LOW-COST MICROWAVE SENSOR FOR DETECTING THE FIRST GENERATION OF MICROPLASTIC IN AQUEOUS MEDIA

JOSAPHAT DESBAS

DISSERTAÇAO DE MESTRADO
EM ENGENHARIA ELÉTRICA

DEPARTAMENTO DE ENGENHARIA ELÉTRICA

FACULDADE DE TECNOLOGIA

UNIVERSIDADE DE BRASÍLIA

Universidade de Brasília
Faculdade de Tecnologia
Departamento de Engenharia Elétrica

LOW-COST MICROWAVE SENSOR FOR DETECTING THE FIRST GENERATION OF MICROPLASTIC IN AQUEOUS MEDIA

Josaphat Desbas

DISSERTAÇÃO DE MESTRADO SUBMETIDA AO PROGRAMA DE PÓS-GRADUAÇÃO EM ENGENHARIA ELÉTRICA DA UNIVERSIDADE DEBRASÍLIA COMO PARTE DOS REQUISITOS NECESSÁRIOS PARA A OBTENÇÃO DO GRAU DE MESTRE.

APROVADA POR:

Achiles Fontana da Mota, PhD (University of Brasília)
(Orientador)

Augusto Martins, PhD (York University)
(Examinador Externo)

Adoniran Judson Barbosa, PhD (University of Brasília)
(Examinador Interno)

Brasília/DF, novembro de 2024

FICHA CATALOGRÁFICA

Desbas, Josaphat
DPPGEE LOW-COST MICROWAVE SENSOR FOR DETECTING THE FIRST
822/241 GENERATION OF MICROPLASTIC IN AQUEOUS MEDIA / Josaphat
Desbas; orientador Achiles Fontana da Mota. -- Brasília,
2024.
124 p.

Dissertação(Mestrado em Engenharia Elétrica) --
Universidade de Brasília, 2024.

1. Ressoador RF . 2. Microplastico. 3. Ressoador
interdigital. 4. Micro canal . 5. Eletromagnetismo. I.
Fontana da Mota, Achiles, orient. II. Título.

REFERÊNCIA BIBLIOGRÁFICA

DESBAS, JOSAPHAT (2024). Low-Cost Microwave Sensor for Detecting the First Generation of Microplastic in Aqueous Media. Dissertação de Mestrado, Departamento de Engenharia Elétrica, Universidade de Brasília, Brasília, DF.

CESSÃO DE DIREITOS

AUTOR: Josaphat Desbas
TÍTULO: Low-Cost Microwave Sensor for Detecting the First Generation of Microplastic in Aqueous Media.
GRAU: Mestre ANO: 2024

_____

Josaphat Desbas
Universidade de Brasília (UnB)
Campus Darcy Ribeiro
Faculdade de Tecnologia - FT
Departamento de Engenharia Elétrica (ENE)
Brasília - DF CEP 70919-970

ACNOWLEDGEMENTS

I would like to extend my heartfelt gratitude to my colleagues at the LEMOM Laboratory at the University of Brasília, whose unwavering support was invaluable throughout my journey in the postgraduate program. Special thanks to the Telecommunications Laboratory at the University of São Paulo in São Carlos for the warm welcome and essential assistance with the VNA during my measurement period. I am especially grateful to Professor Ben-Hur for granting me access to the lab and to Professor Vinícius, who patiently guided me through the calibration process and often stayed late to support my work. My appreciation also goes to Mateus I. O. Souza, who aided and introduced new ideas and techniques to improve my research and measurement methods.

In our lab, I would like to give special thanks to Matheus Rotta Ribeiro, with whom I shared the lab for over two years, for his consistent help and support. I am grateful to João Pedro Moreno de Oliveira, who joined us on the RF journey and made significant contributions to the second sensor model. I owe a great deal to Professor Juliana de Novais Schianti, who was the driving force behind the design and fabrication of the microchannel structure and the preparation of the plastic concentration samples. Additionally, I want to thank Professor Daniel Orquiza de Carvalho, and Professor Sébastien Rondineau, who dedicated extensive time to assisting me with various aspects of this research and training me on the HFSS software.

A special note of appreciation goes to my advisor, Professor Achiles F. da Mota, who introduced me to the fascinating world of RF and high-frequency signals. His valuable insights, patience, and guidance provided solutions and new ideas that were crucial to overcoming the challenges I encountered. It has been a privilege to work and learn with all of you, and I am deeply grateful for the support each of you provided for this research.

I would also like to thank my family, Andrèmen and Joiel, for their unwavering encouragement and belief in me, even from over 5,000 kilometers away. Finally, a heartfelt thank you to Ana Vitória A.D and Hannah N.D, who have become family to me.

ABSTRACT

Title: Low-Cost Microwave Sensor for Detecting the First Generation of Microplastic in Aqueous Media
Author: Josaphat Desbas
Supervisor: Prof. Dr. Achiles Fontana Da Mato
Graduate Program in Telecommunications and Communications Network Engineering Brasília, November 28, 2024

Microplastics have emerged as persistent pollutants in aquatic and ecosystems, and its detection and quantification have become critical to environmental research. This study presents the development and testing of RF-based resonator sensors for detecting microplastics in water. The main goal is to evaluate the sensor's ability to detect and quantify microplastics by analyzing its frequency response. This involves utilizing resonator designs that are highly sensitive to shifts in resonance frequency caused by plastic particles of different sizes and concentrations.

The methodology combined simulation and experimental testing on two sensor models: a simple interdigital resonator and a capacitive interdigital resonator. During the simulation phase, finite element analysis was employed to optimize the resonator structures, with particular emphasis on the electric field distribution and resonance frequency shifts caused by the presence of microplastic particles. These simulations guided the selection of specific resonator geometries and material parameters designed to achieve high sensitivity in practical measurements. The sensor fabrication on the PCB involved integrating microchannels to enable the controlled flow of water samples containing microplastics.

Experimental tests were conducted in two generations, each comprising unloaded (water-only) and loaded (water with microplastics) conditions. The bench tests were performed using a Vector Network Analyzer (VNA) across a frequency range of 1 to 6 GHz, where sensor responses were recorded for various concentrations of microplastic particles (ranging from 0.1% , 0.5% 1%). Microplastics were derived from sanded plastic bottles and ground tire rubber and categorized into particle sizes of less than 300 μm, 150 μm, and 75 μm. Data from the first

generation established baseline resonance shifts for the presence of a single microplastic, while the second-generation sensor design was adjusted to enhance sensitivity and improve response differentiation at higher pollutant concentrations.

Results indicated that both sensor design successfully detected the presence of microplastics, as evidenced by measurable shifts in resonance frequency. Desing 1 demonstrated a maximum frequency shift of 525 MHz, while desing 2 achieved a shift of 105 MHz, indicating that both sensors responded significantly to microplastic presence. The quality factor for each sensor, determined from the bandwidth and peak resonance measurements, demonstrated satisfactory resolution for detecting concentration differences. Model 2 shows improved response stability due to finer particle sizes and higher pollutant concentrations.

In conclusion, this research confirms the potential of RF resonator sensors as effective tools for detecting microplastics in water. By analyzing frequency shifts and optimizing sensor geometry, this study contributes as a foundational approach to non-invasive microplastic detection, with potential implications for further developments in environmental sensing technologies.

Keywords: Microplastic Detection, Resonator Sensors, Resonance

RESUMO

Título: Sensor de Micro-ondas de Baixo Custo para Detectar a Primeira Geração de Microplásticos em Meios Aquosos
Autor: Josaphat Desbas
Orientador: Prof. Dr. Achiles Fontana Da Mato
Programa de Pós-Graduação em Engenharia de Telecomunicações e Redes de Comunicações Brasília, 28 novembro de 2024.

Microplásticos têm se tornado poluentes persistentes em ecossistemas e meio aquáticos, e a detecção e quantificação deles se tornaram fundamentais para a pesquisa ambiental e de saude. Este estudo investiga o desenvolvimento e teste de sensores ressonadores baseados em RF para a detecção de microplásticos em água. O objetivo principal foi determinar a capacidade do sensor de identificar e quantificar microplásticos por meio da análise da resposta em frequência, aproveitando-se de designs de ressonadores sensíveis a mudanças na frequência de ressonância na presença de partículas plásticas de diferentes tamanhos e concentrações.

A metodologia incluiu tanto a simulação quanto o teste experimental de dois modelos de sensor. Na fase de simulação, foi utilizada análise por elementos finitos para otimizar as estruturas dos ressonadores, focando na distribuição do campo elétrico e nas mudanças na frequência de ressonância na presença de partículas de microplástico. Essas simulações orientaram a escolha de geometrias específicas de ressonadores e parâmetros de material esperados para oferecer alta sensibilidade nas medições práticas. A subsequente fabricação dos sensores em PCB incorporou microcanais para facilitar o fluxo controlado de amostras de água com microplásticos.

Os testes experimentais foram realizados em duas gerações, cada uma compreendendo condições descarregadas (somente água) e carregadas (água com microplásticos). Os testes foram realizados com o uso de um Analisador de Rede Vetorial (VNA) em uma faixa de frequência de 1 a 6 GHz, onde as respostas dos sensores foram registradas para várias concentrações de partículas de microplástico (de 0,1% a 1%). Os microplásticos foram derivados de garrafas plásticas lixadas e de borracha moída de pneus, categorizados em tamanhos de partículas inferiores a 300 μm, 150 μm e 75 μm. Os dados da primeira geração

forneceram mudanças de ressonância de referência, enquanto os ajustes no design do sensor para a segunda geração visaram melhorar a sensibilidade e a capacidade de distinguir respostas em concentrações mais altas de poluentes.

Os resultados indicaram que ambos os modelos de sensor detectaram com sucesso a presença de microplásticos, evidenciado por mudanças mensuráveis na frequência de ressonância. O Modelo 1 demonstrou um deslocamento máximo de frequência de 525 MHz, enquanto o Modelo 2 atingiu um deslocamento de 105 MHz, indicando que ambos os sensores responderam significativamente à presença de microplásticos. O fator de qualidade para cada sensor, determinado a partir da largura de banda e das medições de pico de ressonância, demonstrou resolução satisfatória para detectar diferenças de concentração, com o Modelo 2 apresentando estabilidade de resposta aprimorada na presença de partículas de tamanho mais fino e concentrações mais altas de poluentes.

Em conclusão, esta pesquisa confirma o potencial dos sensores de ressonadores RF como ferramentas eficazes para a detecção de microplásticos em água. Ao analisar deslocamentos de frequência e otimizar a geometria do sensor, este estudo contribui com uma abordagem fundamental para a detecção não invasiva de microplásticos, com implicações para desenvolvimentos futuros em tecnologias de sensoriamento ambiental.

Palavras-chave: Detecção de Microplásticos, Sensores de Ressonador, Deslocamento de Frequência, Ressonância Eletromagnética

TABLE OF CONTENTS

LIST OF FIGURES

LIST OF TABLES

CHAPTER 1

1. INTRODUCTION

Microplastics have emerged as a significant environmental issue in recent years, posing threats to the water, air, and food systems [1], [2], [3] . These tiny plastic particles, measuring less than 5mm, have permeated virtually every ecosystem. They are now found everywhere, from oceans, rivers, and lakes to soil and even the air we breathe, infiltrating natural environments and making their way into the water, atmosphere, and food chain [4], [5], [6], [7], becoming now prevalent across the globe [8]. The ongoing rise in synthetic plastic production, coupled with inadequate plastic waste management, has led to widespread pollution, contaminating our environment at an alarming pace [9], [10]. This contamination has far-reaching consequences for both the environment and human health [11]. This introduction will delve into the origins of microplastics, the different sources, and pathways through which they enter the water, air, and food systems impacts, and the technical methods employed for detection across different environmental matrices and analysis.

Microplastic contamination in water, air, and food systems is a pressing concern for scientists, policymakers, and the public [12], [13], [14]. Additionally, raising awareness about the issue and promoting sustainable practices can help reduce the input of microplastics into the environment.

1.1. MICROPLASTIC PRODUCTION

Microplastics have origins rooted in both direct and indirect sources, contributing to their widespread distribution and environmental impact [10], [15], [16], and the direct release of microplastic particles from personal care products and industrial processes[17]. These sources contribute to the widespread distribution of microplastics across terrestrial and aquatic environments, where they persist for extended periods, posing long-term environmental hazards [12]. Understanding the diverse origins of microplastics is crucial for devising effective

strategies to mitigate their proliferation and minimize their detrimental effects on ecosystems and human health.

Fragmentation of Larger Plastic Debris: One of the primary sources of microplastics is the fragmentation of larger plastic debris, such as bottles, bags, and packaging materials, through processes like photodegradation, mechanical abrasion, and weathering [18]. Over time, exposure to environmental factors such as sunlight, wave action, and microbial activity gradually degrades macroplastics into smaller fragments, ultimately reducing them to microplastic-sized particles [19]. Recent studies have highlighted the significant contribution of fragmented plastic waste to the global microplastic pool [20], [20].

Disintegration of Synthetic Fibers: Another significant source of microplastics is the disintegration of synthetic fibers from textiles, clothing, and industrial materials [21]. Synthetic textiles release microfibers into wastewater systems during washing, wear, and disposal, ultimately entering aquatic environments [22]. Studies have shown that synthetic microfibers constitute a considerable proportion of microplastics in freshwater and marine ecosystems, highlighting the need for mitigative measures in textile production and waste management [23], [24].

Direct Release from Consumer Products: Microplastics are also directly released into the environment through the use of consumer products, including cosmetics and cleaning agents[12], [14], [25]. Microbeads, tiny plastic particles used as exfoliants and abrasives in cosmetic products, pose a significant threat to aquatic ecosystems due to their non-biodegradable nature and potential for ingestion by marine organisms [26]. Legislation banning the use of microbeads in personal care products has been enacted in several countries in response to growing concerns over their environmental impact [27].

Industrial Processes and Plastic Pellets: Industrial processes, such as plastic manufacturing, processing, and recycling, contribute to the release of microplastics into the environment through spills, emissions, and runoff [12], [25], [28]. Plastic pellets, also known as nurdles, serve as raw materials in the production of plastic products and are frequently lost during transportation and handling, leading to their dispersal in terrestrial and aquatic ecosystems [29]. Efforts to minimize pellet loss and improve handling practices are essential for preventing microplastic pollution at the source [30].

Atmospheric Deposition and Secondary Sources: Recent research has highlighted the role of atmospheric deposition as a significant pathway for the transport and deposition of

microplastics in terrestrial and aquatic environments [12], [31]. Atmospheric microplastics originate from various sources, including airborne fibers, tire wear particles, and atmospheric fallout from urban areas and industrial emissions [32], [32], [32]. These particles can settle on land and water surfaces, contributing to microplastics contamination in diverse ecosystems [12], [33], [34], such as terrestrial, aquatic, and atmospheric environments worldwide. Here are some key environmental impacts of microplastics contamination: Microplastics can accumulate in ecosystems, impacting organisms across various trophic levels [8]. Marine species, such as fish, seabirds, and marine mammals, may ingest microplastics, mistaking them for food, which can cause physical damage, internal blockages, and impair feeding and digestion [35], [36]. In terrestrial environments, microplastics can build up in the soil, potentially affecting soil health, microbial communities, and plant growth [37]. They also have the capacity to bioaccumulate organisms over time, particularly in species at higher trophic levels[35], [38]. Once ingested, microplastics can absorb and concentrate chemical pollutants from the environment [39]. As predators consume contaminated prey, these pollutants may biomagnify, resulting in higher concentrations at the top of the food chain [14][40], posing risks to apex predators and organisms higher up the trophic ladder [41], [42]. Accumulation of microplastics in natural habitats can lead to habitat degradation and alteration in marine environments; microplastics can settle on the seafloor, covering benthic habitats such as coral reefs and seagrass beds, and impacting sediment-dwelling organisms [43], [44], [45]. On beaches and coastlines, microplastics can accumulate in coastal sediments, affecting beach ecology and nesting habitats for marine turtles and shorebirds etc.

Microplastics can act as vectors for harmful chemicals, including persistent organic pollutants (POPs) and heavy metals [46][47]. These chemicals can adhere to the surface of microplastics in the environment, posing a risk of toxicity when ingested by organisms.[48], [48], [49]. Additionally, the leaching of plastic additives and breakdown products from microplastics may introduce harmful substances into surrounding ecosystems, further exacerbating environmental contamination [46] [49]. Also, microplastics can disrupt biogeochemical cycles by altering nutrient cycling, sediment dynamics, and carbon sequestration processes in ecosystems [50] [51].

In aquatic environments, microplastics can disrupt nutrient cycles, alter microbial activity, and impact oxygen levels in water bodies, posing significant risks to the ecological balance and overall functioning of these ecosystems. [50][52]. Addressing the environmental impacts of microplastic contamination requires comprehensive strategies, including reducing plastic

pollution at its source, improving waste management practices, implementing regulations on plastic production and use, and developing innovative technologies for microplastic detection and remediation [53], [54], [54], [55]. By mitigating microplastic pollution, we can protect ecosystems, safeguard biodiversity, and promote environmental sustainability for future generations. In this sense, understanding the dynamics of microplastics in different environmental compartments is essential for developing targeted solutions to limit their spread and impact.

1.2. MICROPLASTIC TO HUMAN BODY HEALTH RISKS

Microplastic contamination poses potential risks to human health through various pathways, including ingestion, inhalation, and dermal exposure [3] [56] . While the full extent of these health impacts is still being studied, emerging research suggests several potential concerns [57]:

1. *Ingestion*: Microplastics can enter the human body by consuming contaminated food and water [56], [58]. Seafood, particularly shellfish and fish, are known to accumulate microplastics [59], which may be ingested by humans unknowingly [60]. Additionally, microplastics have been detected in drinking water, salt, and other food items [61]. Once ingested, microplastics may accumulate in the gastrointestinal tract and potentially cause physical harm, inflammation, and disruption of nutrient absorption [62] Moreover, there is concern that microplastics may act as vectors for harmful chemicals and pathogens, further exacerbating health risks [12], [63].

2. *Inhalation*: Inhalation of airborne microplastics is another route of exposure. Microplastics can become airborne through various mechanisms, including the fragmentation of larger plastic items, the breakdown of synthetic fibers, and the resuspension of particles from surfaces [64][65]. Workers in industries handling plastic materials, individuals living in urban areas with high levels of air pollution, and even household activities like indoor dusting may be exposed to airborne microplastics [10], [32]. Once inhaled, microplastics may potentially reach the respiratory system and accumulate in lung tissue, leading to inflammation, respiratory problems, and other adverse health effects [66], [67], [68].

3. *Dermal Exposure*: While less extensively studied than ingestion or inhalation, dermal exposure to microplastics remains a significant area of concern[28]. Personal care products

containing microplastic particles, such as exfoliating scrubs and cosmetics, can lead to direct skin contact with these particles[69][70]. Additionally, synthetic clothing made from materials like polyester and nylon can shed microfibers during washing and wearing, potentially exposing individuals to microplastics through skin contact [71][72]. While the health implications of dermal exposure to microplastics are not fully understood, there is growing recognition of the need for research in this area.

Overall, while the health impacts of microplastic contamination on humans are still being elucidated, the potential risks underscore the importance of mitigating microplastic pollution at its source and implementing measures to reduce human exposure[4], [33], [73]. Continued research is essential to understand the extent of these risks better and develop strategies to protect human health in the face of microplastic contamination. Having examined the potential health hazards linked to microplastic contamination, let's delve into the diverse methodologies utilized for detecting and quantifying these pervasive pollutants in environmental samples.

1.3. DETECTING MICROPLASTICS

Researchers have a range of methods for detecting and quantifying microplastics in environmental samples. Each method has its own advantages and limitations, so it is important to carefully consider the study's specific needs when choosing an appropriate technique[17], [74], [75].

1. *Microscopy*: One commonly used method is visual identification, which involves manually sorting through samples under a microscope to visually identify and count microplastic particles. Optical microscopy, including stereomicroscopy and microscopy with polarized light, is often used to visually identify and characterize microplastic particles based on their size, shape, color, and other morphological features[74], [76]. While this method is relatively simple and low-cost, provides high-resolution images, and allows for manual identification, it is labor-intensive and subjective, relying heavily on the expertise of the analyst. Additionally, visual identification may not be suitable for detecting very small or transparent microplastics [74], [77].

2. *Spectroscopy*: Fourier Transform Infrared (FTIR) spectroscopy is another widely used technique for identifying and characterizing microplastics in environmental samples [78]. Like Raman spectroscopy, FTIR spectroscopy analyzes the interaction of infrared radiation with

molecular vibrations in the sample to generate a unique spectrum that can be used for material identification. by analyzing the chemical composition of particles [79]. FTIR spectroscopy offers several advantages for microplastic analysis. It is sensitive to a wide range of polymer types and can differentiate between different types of plastics based on their molecular structure[12] . FTIR spectroscopy is also relatively rapid and non-destructive, allowing for efficient analysis of large numbers of samples. FTIR and Raman spectroscopy both provide information about molecular vibrations but use different approaches. FTIR detects absorption lines from molecular vibrations in the infrared spectrum, though weak signals can be challenging to identify due to noise. Raman spectroscopy uses a visible or NIR laser to excite vibrational modes, measuring the shifted (Stokes) emission. This separation between the laser and Raman signals enables better detection of weak vibrational modes[80]. These techniques enable the identification of polymer types and can distinguish between different types of microplastics [78], [80]. However, like Raman spectroscopy, FTIR spectroscopy has its limitations [12]. They require specialized equipment and may not be suitable for quantifying microplastics in complex environmental samples because they require relatively large sample sizes and may struggle with the detection of very small microplastic particles [12], [81]. Additionally, FTIR spectroscopy may be less effective for identifying microplastics in complex matrices or heavily contaminated samples, where interference from other materials can affect the accuracy of the analysis[81].

In the context of microplastic detection, Raman spectroscopy offers several advantages. It allows for rapid and non-destructive analysis of particles, enabling researchers to identify the polymer type of microplastics present in environmental samples [78]. Additionally, Raman spectroscopy can distinguish between different types of plastics based on their unique spectral signatures, providing valuable information for understanding the sources and distribution of microplastic pollution [82], [83], [84]. However, there are limitations to Raman spectroscopy as well. It requires relatively large sample sizes for accurate analysis, which may pose challenges when dealing with small microplastic particles [81], [85]. Additionally, Raman spectroscopy is less effective for detecting microplastics embedded within complex matrices or heavily contaminated samples, as the signal from the microplastics may be obscured by interference from other materials [84].

3. *Pyrolysis-Gas Chromatography/Mass Spectrometry (Py-GC/MS)*: Pyrolysis is a technique that thermally decomposes organic materials, including microplastics, into volatile compounds, which are then analyzed by gas chromatography/mass spectrometry (GC/MS) to identify the polymer composition of the original material [12], [86]. Py-GC/MS is highly sensitive and can provide detailed information about the chemical composition of microplastics. However, it requires specialized equipment and expertise[86], [87].

6. *Automated Imaging Analysis*: Automated imaging analysis utilizes image processing software to analyze digital images of environmental samples and identify microplastic particles based on predefined criteria such as size, shape, and color [88]. This approach allows for rapid screening of large sample volumes but may lack the accuracy and specificity of other techniques [89].

7. *Polymerase Chain Reaction (PCR):* PCR-based methods can also be used to detect and quantify microplastics by targeting specific DNA sequences associated with microbial communities that colonize plastic surfaces [89]. While PCR is highly sensitive, it requires prior knowledge of the microbial communities associated with microplastics and may be subject to interference from environmental contaminants[90].

Each of these methods has its own strengths and limitations when it comes to detecting microplastics in environmental samples. In some cases, researchers often employ a combination of techniques to obtain comprehensive insights into sample pollution, and the choice of technique will depend on factors such as sample size, sample complexity, and the specific research objectives [74]. By carefully evaluating the advantages and limitations of each method, researchers can select the most appropriate approach for their study and contribute to our understanding of the environmental impact of microplastics. Continued advancements in analytical techniques and method development are essential for improving our understanding of the sources, distribution, and impacts of microplastics in the environment [91].

One cheap alternative that can be used to detect microplastics at aqueous media is employing **microwave sensors**. These sensors are easily fabricated, with a small cost, and can have high sensitivity to the presence of microplastics. In this sense, we propose using an interdigital resonator operating in a microwave regime to detect the presence of microplastics in an aqueous medium [89], [92]. The sensor is coupled with a microfluidic channel that can be linked to any water source for real-time water quality monitoring. The results show that both

sensor designs effectively detected microplastics, ranging from a single piece measuring 0.3x0.3x0.3 mm to a concentration of 1% of microplastics with a size of 75 microns, as they passed through the microfluidic channel. This demonstrates clear sensitivity to these contaminants. This detection was evidenced by measurable shifts in resonance frequency in both designs. The first one exhibited a maximum frequency shift of 525 MHz, indicating a strong interaction between the sensor's electric field and the microplastic particles. The second one also successfully detected microplastic presence, with a frequency shift of 105 MHz. Although the first design exhibited a larger shift, indicating greater sensitivity, both designs produced significant responses, confirming their ability to detect microplastic particles in the solution. These findings highlight the potential of both sensor designs for microplastic detection applications, each offering distinct sensitivity profiles suited to different detection requirements.

1.4. ORGANIZATION OF THE DISSERTATION

The structure of this thesis is as follows: **Chapter 2** provides foundational knowledge, including a literature review on key concepts such as transmission lines, S-parameters, Maxwell Garnett theory, and the relationship between frequency and concentration. **Chapter 3** discusses the rationale behind selecting interdigital sensor simulations. It describes the design and optimization of two sensor topologies, incorporating microfluidic elements. This chapter includes simulations of interdigital resonators with water in the microchannel, tests of both sensor models, and validation of Maxwell Garnett theory through variations in plastic sample concentrations. **Chapter 4** focuses on the experimental setup and measurement results. It provides detailed descriptions of the fabrication methodology, calibration, and testing procedures for both sensor models. **Chapter 5** concludes with an in-depth analysis and discussion of the findings, followed by a summary of the study's contributions and suggestions for potential future research directions.

1.5. MAIN CONTRIBUTIONS

The research presented in this master’s thesis contributes in academic and practical domains, particularly in addressing the pressing issue of microplastic contamination. Developing and applying microstrip interdigital resonators as sensors for detecting

microplastics offers a low-cost approach to tackling this global environmental problem. By leveraging the principles of RF and microwave technology, this method provides an efficient solution to identify microplastics in water, a field that still lacks accessible and accurate detection techniques.

The use of RF resonators to detect microplastics opens up new possibilities in environmental sensing. The interdigital resonator presented in this work demonstrates the ability to detect different microplastics through resonance frequency and Quality factor (Q-factor) changes. The proposed approach offers a scalable, cost-effective alternative for widespread environmental monitoring. Through extensive simulations using HFSS, the topology of the interdigital resonator was carefully optimized to achieve higher sensitivity to microplastics. The process involved adjusting the circuit geometry to maximize the electromagnetic field interaction with the test samples, ensuring accurate detection of microplastic pollutants. This systematic optimization approach could be applied to other environmental detection problems, thereby expanding the utility of RF technology in various sensing applications.

Other Contributions

Standardization in Circuit Manufacturing

For the Laboratory of Electromagnetic Materials (LEMOM) at the University of Brasília, this candidate played a role in advancing the standardization of RF circuit manufacturing processes. By implementing photolithography and calibration techniques, the study ensures both repeatability and reliability in sensor fabrication. These attributes are crucial for scaling up production and facilitating the transition of these sensors from experimental prototypes to commercially viable products. Standardizing these manufacturing processes enhances the sensors' consistency and quality and bridges the gap between academic research and industrial application.

Additionally, this research has significantly contributed to the academic growth and development of undergraduate students under the mentorship of Professor Achiles F. da Mota. I had the privilege of helping to guide two dedicated students, Maria Luiza Vasconcelos Do Nascimento and João Pedro Moreno de Oliveira, through their research endeavors. João Pedro's collaboration was fundamental in developing and refining Sensor Model 2. Their contributions enhanced the quality and scope of this research and provided them with invaluable hands-on experience in RF sensor technology and microplastic detection methodologies.

Moreover, this master's program allowed me to intern at the LEOST laboratory of Université Gustave Eiffel in France. During this internship, I gained hands-on experience working with eco-materials, learning advanced calibration techniques, and collaborating on innovative research projects. This experience allowed me to apply my theoretical knowledge in a practical setting, deepen my understanding of RF technology in environmental applications, and build a network of professional contacts that will be invaluable for my future career in research and development.

2. THEORETICAL FUNDAMENTS AND METHODOLOGY

An RF resonator is a key component in RF systems, used to select or reject specific frequencies. It operates on the principle of resonance, where inductance and capacitance transfer energy at a resonant frequency, minimizing energy loss. RF resonators are widely applied in filters, oscillators, and sensors.

Microwaves, a subset of the electromagnetic (EM) spectrum, are generally defined as waves with frequencies ranging from 300 MHz to 300 GHz, corresponding to wavelengths (in free space) between 1 meter and 1 millimeter. The radio frequency (RF) spectrum is positioned just below the microwave range, with the boundary between the two being somewhat flexible depending on the technologies used. Both RF and microwave technologies have diverse applications across fields such as communications, radar, navigation, radio astronomy, sensing, and medical instrumentation. These applications typically operate within a frequency range from approximately 300 kHz to 300 GHz, encompassing a significant portion of the electromagnetic spectrum. Understanding this wavelength range is essential for leveraging RF/microwave systems in various technological applications[93]. A deeper understanding of RF resonators also requires familiarity with transmission lines and S-parameters, as these concepts are key to analyzing their performance in RF systems.

2.1. TRANSMISSION LINES

A transmission line is a physical medium used designed to guide electromagnetic waves from one point to another with minimal energy loss. It plays a crucial role in RF circuits and connects various components such as antennas, amplifiers, filters, and resonators. Transmission line theory describes their behavior by focusing on key electrical parameters. This approach is possible because, over small segments of the line, the behavior of the fields can be accurately approximated by basic circuit elements: resistance (R) representing the loss of energy due to the resistive heating in the conductors. In the lumped model, this accounts for the series resistance per unit length, inductance (L), modeling the magnetic field induced by the changing current in the line. This is represented as a series inductance per unit length and accounts for the storage of magnetic energy. capacitance (C), accounting for the ability of the line to store electric energy between the conductors. This is modeled as a shunt capacitance per unit length. and conductance (G), representing the leakage current through the dielectric between the conductors. This is modeled as a shunt conductance per unit length. These parameters influence how signals propagate, including their speed, attenuation, and impedance characteristics. The lumped-element model is valid when the wavelength of the signal is much larger than the length of the line segment being analyzed. Under this condition, the variations of voltage and current along each segment are negligible, and the distributed parameters can be treated as concentrated elements.

Transmission lines in printed circuit boards (PCBs) serve as interconnections that transmit signals from transmitters to receivers. A PCB transmission line comprises two conductors: a signal trace and a return path, typically a ground plane. The space between these conductors consists of the PCB's dielectric material. The alternating current traveling through the transmission line at high frequencies exhibits an electromagnetic wave propagation behavior. A key aspect of wave propagation in a transmission line is that every point along the line possesses its own impedance. If the line’s geometry remains uniform, the impedance is constant throughout its length. Such a line is referred to as a controlled impedance line.

Maintaining uniform impedances is crucial in high-frequency applications because non-uniform impedance causes signal reflections, distortion, and electromagnetic noise, which can degrade signal quality and lead to errors in transmitted information. Thus, controlling the impedance of the transmission line ensures predictable signal behavior and minimizes issues like signal reflections and crosstalk.

Two primary transmission line types are used in PCBs: microstrips (Figure 2.3) and striplines (figure A.7 Apendix). Both configurations are designed to manage signal integrity in high-frequency circuits. Two critical properties of a transmission line on a PCB are its characteristic impedance and its propagation delay per unit length. If the impedance is not controlled across the line's entire length, or if it is not terminated with the correct impedance, signal degradation may occur, potentially leading to communication errors.

In summary, the design and control of transmission line impedance are essential for efficient signal transmission in RF circuits. This ensures signal integrity by minimizing reflections, distortion, and electromagnetic interference, which are especially significant at high frequencies

2.1.1. THE TELEGRAPHER'S EQUATIONS

The fundamental behavior of a transmission line is governed by the Telegrapher's equations, which describe the voltage and current variations along the length of the line. These equations, derived from Maxwell's equations, model the transmission of electromagnetic waves along the line and account for losses due to resistance, inductance, capacitance, and conductance. The telegrapher's equations can be expressed as in[94] [95]:

$$\frac{\partial V(x,t)}{\partial x} = -L\frac{\partial I(x,t)}{\partial t} - RI(x,t) \quad 2.1$$

$$\frac{\partial I(x,t)}{\partial x} = -C\frac{\partial V(x,t)}{\partial t} - GV(x,t) \quad 2.2$$

where $V(x,t)$ is the voltage at position (x) and time (t), $I(x,t)$ is the current, R is the resistance per unit length (Ω/m), L is the inductance per unit length (H/m), C is the capacitance per unit length (F/m), and G is the conductance per unit length (S/m).

Equations (2.1) and (2.2) explain the factors influence the rate of change of voltage along the transmission line describe in [94]:

- Inductive effect $L\frac{\partial I(x,t)}{\partial t}$: This term accounts for the voltage drop caused by the inductance of the line, which opposes changes in current (Lenz law).
- Resistive effect $RI(x,t)$: This term represents the voltage drop due to resistance, which causes power dissipation as heat (Ohm's Law).

- Capacitive effect $C\frac{\partial V(x,t)}{\partial t}$: This term accounts for the current induced by the changing electric field in the line's capacitance.
- Conductive effect $GV(x,t)$: This term represents leakage current caused by imperfect insulation, modeled as conductance.

These equations describe how voltage and current propagate along a transmission line and how they are affected by the line's physical properties. The terms related to resistance (*R*) and conductance (*G*) represent the dissipative effects (losses) in the line, while the inductive (*L*) and capacitive (*C*) terms describe energy storage mechanisms.

In an ideal transmission line, where (*R* = 0) and (*G* = 0), the Telegrapher's equations simplify describing purely inductive and capacitive effects, resulting in lossless wave propagation. The non-zero (R) and (G) for real transmission lines introduce attenuation and phase shift, influencing the signal's speed and integrity.

The Telegrapher's equations are central in the design of RF and high-frequency circuits. They allow engineers to calculate key parameters like characteristic impedance (Z_0), signal velocity, and attenuation, which are essential for matching transmission lines to other components and minimizing signal reflection and distortion. Moreover, they help predict how the line will perform under various loading conditions, making them critical for designing efficient communication systems, radar, and microwave networks.

2.1.2. CHARACTERISTIC IMPEDANCE AND PROPAGATION CONSTANT

The characteristic impedance Z_0 of a transmission line is a key parameter determining how the line interacts with connected components. It is defined as the ratio of voltage to current in a traveling wave along the line and is given as in [94] by:

$$Z_0 = \sqrt{\frac{R+\mathrm{j}\omega L}{G+\mathrm{j}\omega C}} \tag{2.3}$$

where ω is the angular frequency of the signal ($\omega = 2\pi f$) and f the frequency. For lossless transmission lines (where $R = 0$ and $G = 0$), this simplifies to:

$$Z_0 = \sqrt{\frac{L}{C}} \tag{2.4}$$

Another important parameter is the propagation constant (k), which describes the attenuation (real part) and phase shift (imaginary part) of the signal as it propagates. It is expressed as:

$$k = \alpha + \mathrm{j}\beta = \sqrt{(R + j\omega L)(G + \mathrm{j}\omega C)} \quad 2.5$$

where α is the attenuation constant (describes signal loss per unit length) and β is the phase constant (describes the phase change per unit length). In a lossless line, $k = \mathrm{j}\beta$ and the phase constant $\beta = \omega\sqrt{LC}$.

2.1.3. REFLECTIONS AND STANDING WAVES

If the transmission line impedance is not matched to the load, a portion of the signal will be reflected toward the source. The reflection coefficient (Γ) is a measure of the magnitude of the reflected wave and is given from [96] by:

$$\Gamma = \frac{Z_L - Z_0}{Z_L + Z_0} \quad 2.6$$

where Z_L is the load impedance, Z_0 is the transmission line's characteristic impedance.

Reflections lead to the formation of standing waves along the line, characterized by constructive and destructive interference. The Voltage Standing Wave Ratio (VSWR) is a measure of how well the line is matched to the load and is defined in[96] as:

$$\mathrm{VSWR} = \frac{1 + |\Gamma|}{1 - |\Gamma|} \quad 2.7$$

2.2. S-PARAMETERS

The scattering parameters, or S-parameters, describe how RF signals behave regarding reflection and transmission when passing through components or networks. S-parameters are used extensively in analyzing RF resonators, filters, amplifiers, and transmission lines. Unlike impedance parameters, S-parameters are particularly convenient because they directly relate to the measurable quantities at high frequencies, such as reflected and transmitted power.

2.2.1. DEFINITION OF S-PARAMETERS

For a two-port network (which is common in RF applications), S-parameters are defined in terms of the outgoing waves at port 1(a_1) and 2 (a_2) and the incoming wave at ports 1(b_2) and 2 (b_2), and the S-matrix relates all waves as [97]:

$$\begin{bmatrix} b_1 \\ b_2 \end{bmatrix} = \begin{bmatrix} S_{11} & S_{12} \\ S_{12} & S_{22} \end{bmatrix} \begin{bmatrix} a_1 \\ a_2 \end{bmatrix} \quad 2.8$$

where S_{11} is reflection coefficient at port 1, S_{22} is reflection coefficient at port 2 and $S_{12(21)}$ is the transmission coefficient from port 1(2) to port 2(1).

Figure 2.1- Depicting a transmission line with a Material Under Test (MUT), this image shows an incident wave at Port 1, an incident wave at Port 2, and the corresponding reflected waves at both ports.

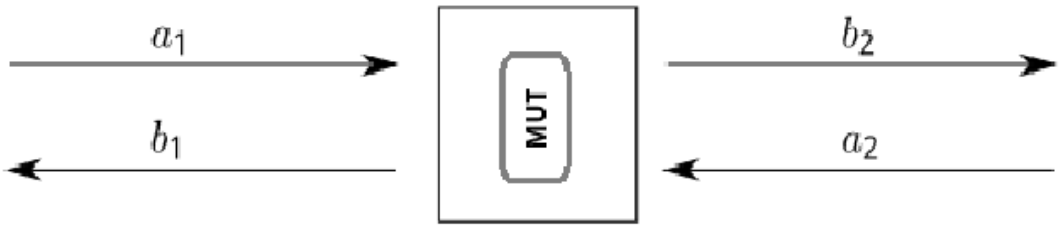

Expanding the matrices into equations gives:

$$b_1 = S_{11}a_1 + S_{12}a_2, \quad 2.9$$

and,

$$b_2 = S_{21}a_1 + S_{22}a_2, \quad 2.10$$

Each equation gives the relationship between the outgoing and incident waves at each of the network ports, 1 and 2, in terms of the network's individual S-parameters, where a_1 in considered incident wave at port 1, a_2 incident wave at port 2 and b_1 is a reflected waves from port 1 and b_2 a reflected waves from port 2.

2.2.2. HOW S-PARAMETERS WORK

- S_{11} (Input Reflection Coefficient): This parameter indicates how much of the signal incident at port 1 is reflected due to impedance mismatch. A perfect match gives $S_{11} = 0$, meaning no reflection.

- S_{21} (Forward Transmission Coefficient): This represents how much of the signal from port 1 is transmitted to port 2. Ideally, for a transmissive resonator, S_{21} should peak at the resonant frequency, indicating that most of the signal is passed through at this frequency.

- S_{12} (Reverse Transmission Coefficient): Describes how much of the signal from port 2 is transmitted to port 1.

- S_{22} (Output Reflection Coefficient): like S_{22}, but measured at port 2. It tells us how much of the signal incident at port 2 is reflected due to impedance mismatch.

2.2.3. FORMULAS FOR S-PARAMETERS

The S-parameter S_{ij}can be calculated measuring the ingoing field amplitudes, at the ith-port (b_i) when only the j-th excitation is on $a_n(n \neq j) = 0$, as follows [96]:

$$S_{ij} = \frac{b_i}{a_j}. \quad 2.11$$

In terms of power, $|S_{ij}|^2$provides the ration of the outgoing from port *j* (P_{in}) to the ingoing power at port *i* (P_{out}) as follows [96]:

$$|S_{ij}|^2 = \frac{P_{out}}{P_{in}}. \quad 2.12$$

Measuring S-parameters is crucial for characterizing materials, particularly in the microwave regime. These parameters provide insights into how electromagnetic waves interact with material, specifically through the transmitted and reflected signals [98]. These interactions are directly related to the material's permittivity and permeability, allowing for extracting these fundamental properties. By analyzing the S-parameters, it becomes possible to evaluate how a material influences the propagation of electromagnetic waves, which is essential for applications ranging from material science to microwave circuit design [99] .

2.2.1. DIELECTRIC PROPERTIES OF MATERIALS

When material subjected to an electromagnetic field, polarizable dielectric materials indeed become polarized, with their dipoles aligning along the applied field. This process, known as dielectric polarization[100][101]. The dielectric properties of substances indeed pertain to their electrical attributes, particularly their limited conductivity and response to electric fields. These properties are fundamental in understanding how materials interact with electromagnetic fields. This knowledge becomes particularly critical when selecting the most appropriate material for detecting microplastics at frequencies up to 6 GHz. These dielectric properties, particularly permittivity, permeability and loss tangent, are crucial in determining

their response to electric fields, which is essential for accurate material characterization. The loss tangent (also called the dissipation factor or tan δ) is a parameter used to describe the energy loss in a dielectric material when it is subjected to an alternating electromagnetic field. It quantifies how efficiently a dielectric material can store and dissipate electrical energy. Mathematically, the loss tangent is defined as:

$$tan\,\delta = \frac{\sigma}{\omega\epsilon_r\epsilon_0} = \frac{\mathrm{Im}(\epsilon)}{\mathrm{Re}(\epsilon)}. \quad 2.13$$

where: δ is the loss angle, representing the phase difference between the electric field and the resulting polarization, σ is the material's conductivity (S/m).

2.3. GARNETT MAXWELL

The Maxwell-Garnett theory is a well-established effective medium approximation used to describe the electromagnetic properties of composite materials, where small inclusions (like microplastics) are embedded in a host medium (such as water). In this context, if microplastics are dispersed in water and behave like dipoles under the influence of an external electromagnetic field, the Maxwell-Garnett theory plays a pivotal role in explaining the material's macroscopic electrical and magnetic response. It's not just a theory, but a powerful tool that keeps us engaged and interested in the complex world of permittivity and permeability. The theory provides a framework for relating the measured electromagnetic response to the concentration and distribution of microplastic particles. This approach is particularly effective at frequencies up to 6 GHz, where the dielectric properties of the microplastics influence the transmission and reflection of the waves, enabling their detection and quantification.

2.3.1. MICROPLASTICS AS DIPOLES

When microplastics, which may be dielectric or slightly conductive, are suspended in water, they can exhibit polarization under the influence of an electric field, potentially behaving as electric dipoles depending on their material properties and the field's characteristics. This is because, at the microscopic level, the material properties of microplastics differ from those of water, causing charge polarization. In the presence of an external electric field, microplastic particles polarize, acting as effective dipoles within the medium [102][103]. These dipoles contribute to the composite material's effective permittivity (ε_{eff}) (water with microplastics). The Maxwell-Garnett model calculates effective permittivity based on the volume fraction of

the microplastics and their individual permittivity relative to the water. This polarization can affect the overall dielectric response, altering how the material absorbs or transmits electromagnetic waves[104].

The interaction between the field and the dipoles' material properties determines the dipoles' behavior in an electromagnetic field. When exposed to an electric field, each microplastic particle polarizes, creating a dipole moment $\vec{p}$ which is proportional to the applied electric field $\vec{E}$ by the particle`s polarizability α. The surrounding water affects how these dipoles interact with each other., and the Maxwell Garnett theory averages this effect to determine the bulk permittivity[102]:

$$\varepsilon_{eff} = \varepsilon_{host}\left(1 + 3f_v \frac{\varepsilon_{\text{inclusion}} - \varepsilon_{host}}{\varepsilon_{\text{inclusion}} + 2\varepsilon_{host}}\right), \quad 2.14$$

where f_v is the volume fraction of the microplastics, ε_{host} is the permittivity of water, and $\varepsilon_{\text{inclusion}}$ is the permittivity of the microplastics.

Figure 2.2- Real (blue) and Imaginary (red) part of the water permittivity.

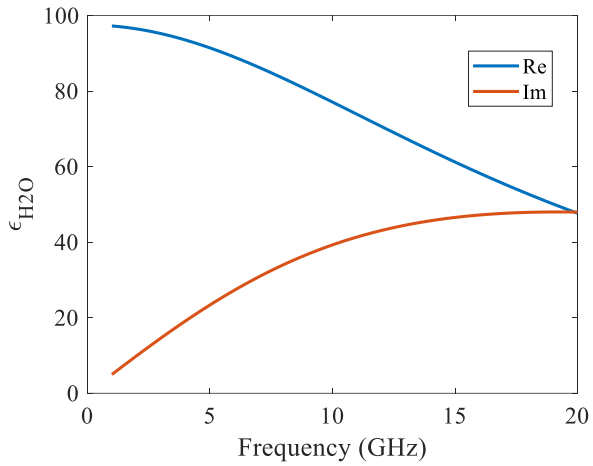

At microwave regime, the water permittivity can be estimated as [105],

$$\varepsilon_{H2O} = \varepsilon_\infty + \frac{(\varepsilon_{DC} - \varepsilon_\infty)}{1 + \omega^2\tau^2}(1 + \mathrm{j}\omega\tau), \quad 2.15$$

where $\varepsilon_\infty = 2.25$ is the water relative permittivity at high frequencies, $\varepsilon_{DC} = 97.5$ is the water relative permittivity at low frequencies, $\tau = \frac{8.27T}{273}$ [ps] is the water relaxation time, and T is the temperature in Kelvin. The real (blue) and imaginary (red) part of ε_{H2O} are shown in **Erro! Fonte de referência não encontrada.**2 considering T = 25 ºC. As can be seen, the real part of the permittivity is very high at low frequencies and decreases as the frequency increases. The opposite behavior can be seen for the imaginary part.

Figure 2.3 - (a) Effective permittivity of water embedded with microplastics for varying plastic concentration. The yellow arrow represents the trend when increasing concentration. (b) presents the derivative of the permittivity.

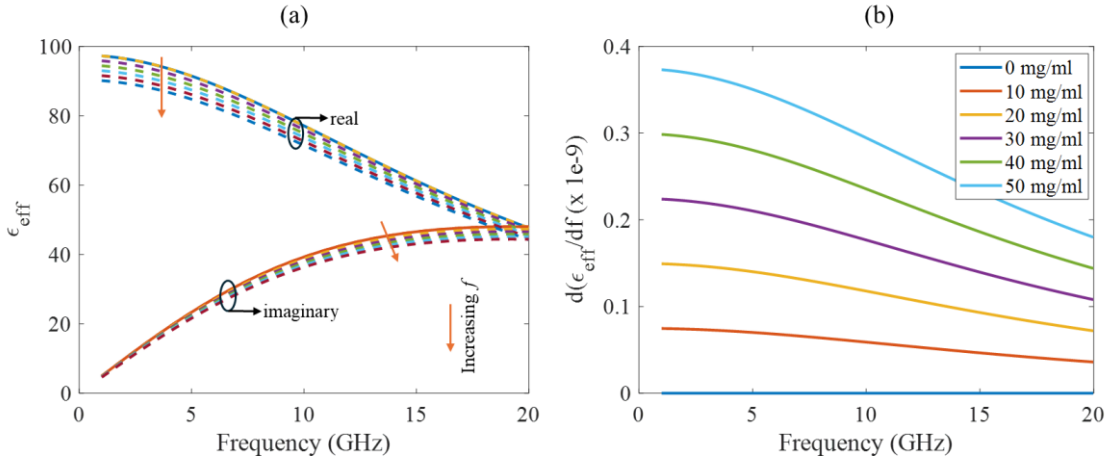

When microplastics are included in water under an electric field exitation, they behave like dipoles, changing their electric properties. To evaluate its impact, we have modeled the inclusion of microplastic particles in water using the Maxwell-Garnett theory, which describes a composite material's effective permittivity (ε_{eff}). Assuming that microplastics are dispersed within the water, with a density of 1.3 mg/mL and a permittivity of 2.25 [106]. As microplastics are introduced, they behave as dipoles in response to the applied electromagnetic field, altering the electric properties of the medium. This leads to changes in the effective permittivity of the water-microplastic mixture, which can be observed through shifts in the real and imaginary components of ε_{eff}, shown in Figure 2.3 (a). Figure 2.3 (a) shows the real and imaginary components of effective permittivity as functions of frequency. As the concentration of microplastics increases from 0 mg/mL to 50 mg/mL, the effective permittivity decreases. This occurs because microplastics have a lower permittivity than water, and their inclusion reduces the overall permittivity of the medium. These variations highlight how the microplastic particles affect the dielectric properties of the medium.

Figure 2.3 (b) shows $\mathrm{d}\varepsilon_{eff}/\mathrm{d}f$ with respect to frequency for different microplastic concentrations. This derivative is critical because it indicates how sensitive the system is to changes in frequency. Higher values of $\mathrm{d}\varepsilon_{eff}/\mathrm{d}f$ imply greater sensitivity to microplastic concentrations. As the frequency increases, the sensitivity decreases, suggesting that the best frequency range to perform measurements is below 6 GHz. At these lower frequencies, the system exhibits the highest variation in permittivity, making it easier to detect changes due to the presence of microplastics.

2.4. MICROSTRIP

The identification of microplastics in environmental samples demands sophisticated and precise analytical techniques. As a result, the detection and characterization of microplastics have become crucial research areas in understanding their distribution, impact, and potential mitigation strategies. By exploring the electrical characteristics, permittivity, and empirical formulas associated with these technologies, it is possible to make informed decisions about selecting the most suitable method for detecting and quantifying microplastics in various environmental matrices. By examining their applicability and sensitivity to microplastics' presence, this study aims to provide valuable insights into choosing the optimal technology for ongoing research in microplastic detection and its implications for environmental conservation efforts. Understanding and tackling microplastic issues are critical steps towards preserving ecosystems and safeguarding the health of both the environment and human populations

Microwave circuit technologies are integral to diverse applications like telecommunications, radar systems, wireless communication, and satellite communication. Efficient and high-performance circuit design relies on understanding the electrical characteristics unique to each technology. Key electrical characteristics, such as characteristic impedance (Z_0), attenuation factor, and signal propagation speed (v), are crucial in high-frequency circuit designs. The values of (Z_0) and (v) are affected by the effective relative permittivity (ϵ_r), while signal losses are influenced by α_c. The following parameters will be employed in this section to calculate the characteristic impedance (Z_0), the conductor loss factor (α_c), and the effective relative permittivity ($\varepsilon_{r,\text{eff}}$) of the transmission lines. These key parameters are applicable to the various transmission line structures discussed, by definition, they are:

- (α_c): The conductor loss factor, which quantifies the energy loss due to the resistance of the conductors in the transmission line. This factor influences the attenuation of the signal as it propagates through the line, and higher conductor losses can degrade signal quality.

- ($\varepsilon_{r,\text{eff}}$): The effective relative permittivity of the transmission line, which affects the speed of signal propagation (v) and the characteristic impedance (Z_0). The effective permittivity takes into account both the dielectric material and the structure of the transmission line, providing a more accurate representation of how electromagnetic waves travel through the medium. These parameters will be used in detailed calculations to evaluate the performance

of the different transmission line structures, enabling a comprehensive comparison in terms of signal integrity, loss mechanisms, and impedance matching.

The main text focuses on microstrip analysis, while the results for stripline, coplanar waveguide, slotline, and asymmetric stripline, along with the definitions and notations used in their formulas, are presented in the Appendix A. Microstrip technology is widely utilized in microwave integrated circuits, featuring a conductor trace placed on a dielectric substrate with a ground plane on the other side, as seen in Figure 2.4. This planar transmission line offers advantages such as easy integration, cost-effectiveness, and design flexibility for microwave circuits [93], [107]. However, it has some drawbacks, including radiation, higher losses, and limited power handling capabilities compared to other technologies.

Figure 2.4- Microstrip model on the top of a substrate (right) and a cut view with dimension (left).

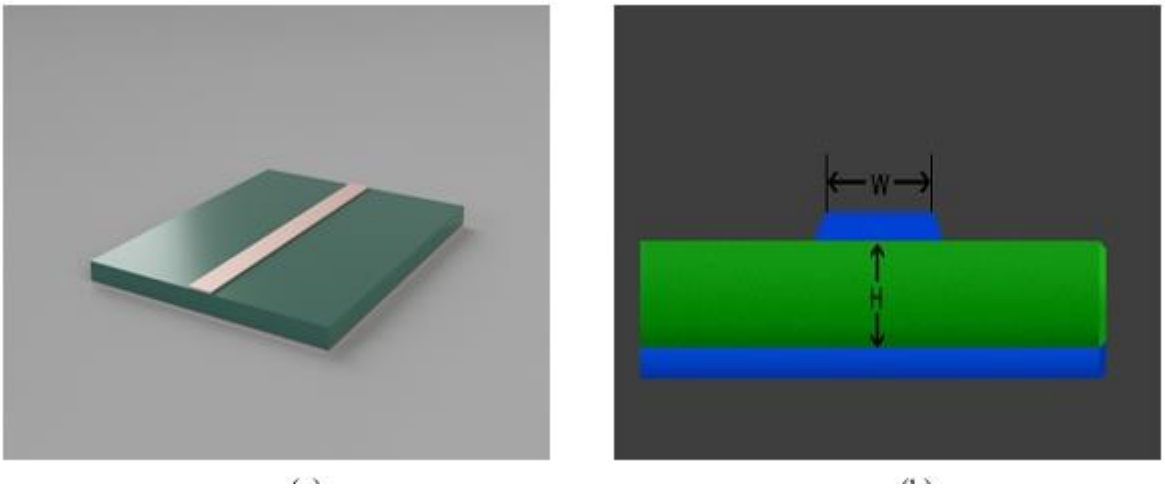

The effective permittivity of the microstrip propagation mode is given by [107],

$$\varepsilon_e = \varepsilon_{\mathrm{r}} - \left(\frac{\varepsilon_{\mathrm{r}} - \varepsilon_{\mathrm{r,eff,dc}}}{1+p(f)}\right), \tag{2.16}$$

$$\epsilon_{\mathrm{r,eff,dc}} = \frac{\epsilon_r+1}{2} + \frac{\epsilon_r - 1}{2}\frac{1}{\sqrt{1+12H/W}}, \tag{2.17}$$

where ε_{r} is the substrate permittivity, H is the substrate thickness and W is the microstrip width, $p(f)$, is given by,

$$P(f) = P_1P_2[10^{-6}fh(0.1844 + P_3P_4)]^{1.5763}, \tag{2.18}$$

$$\mathrm{P_1} = 0.27488 + [0.6315 + 0.525(1.57\mathrm{x}10^{9}\mathrm{fh} + 1)^{-20}]u - 0.065683\mathrm{e}^{(-8.7513\mathrm{u})}, \tag{2.19}$$

$$\mathrm{P_2} = 0.33622\left[1 - \mathrm{e}^{(0.336221\epsilon_r)}\right], \tag{2.20}$$

$$\mathrm{P_3} = 0.0363e^{4.6\mathrm{u}}\left\{1 - e^{-\left(\frac{10^{-8}fh}{3.87}\right)^{4.97}}\right\}, \tag{2.21}$$

$$P_4 = 1 + 2.75\left\{1 - e^{-\left(\frac{\epsilon_r}{15.916}\right)^8}\right\}. \quad 2.22$$

In our study, we utilize Rogers Duroid 5880 with thickness H=1.6 mm and $\varepsilon_r = 2.2$. In this configuration, the impedance is given by

$$Z_0 = \frac{120\pi}{\sqrt{\varepsilon_e}\left[\frac{W}{H}+1.393+0.667\ln\left(\frac{W}{H}+1.444\right)\right]}. \quad 2.23$$

Figure 2.5 - Impedance of the microstrip line.

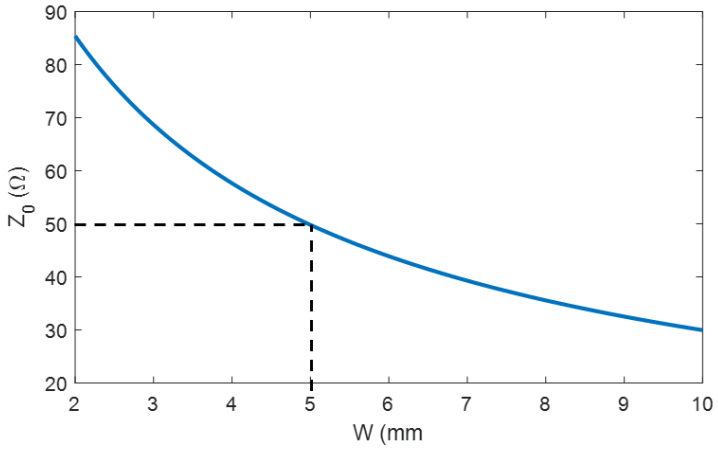

Figure 2.5 show the calculated impedance of the microstrip when above a Duriod 5880 substrate for 3.5 GHz. Since most Network Analyses operate with an impedance of 50 Ohms, we design the microstrip with W = 5mm to match our system.

Different dielectric materials are combined above the circuit, which impacts effective permittivity and impedance. Using $\epsilon_{eff}(\gamma)$ as the permittivity of the new material (calculated in section 2.2, where γ is the concentration in mg/ml), 2.12 turns into:

$$\epsilon_{r,eff,dc}(\gamma) = \frac{\epsilon_r+\epsilon_{eff}(\gamma)}{2} + \frac{\epsilon_r - \epsilon_{eff}(\gamma)}{2}\frac{1}{\sqrt{1+12H/W}} \quad 2.24$$

In this context, (v_p) represents the volume of a microplastic particle, which is considered to have a spherical structure to simplify the characterization calculations. This assumption helps in determining the volume easily using the formula for the volume of a sphere, $(v_p = \frac{4}{3}\pi r^3)$, where (r) is the radius of the microplastic particle. On the other hand, (v_t) represents the total volume of microplastic particles suspended in the water under test. This total volume is calculated based on the microfluidic channel's volume, through which the water transports the microplastic particles during the experiment. The microfluidic volume considers the dimensions of the channel, ensuring that the total volume of the microplastics in the water can be accurately estimated and related to the sensor's measurements. In this sense,

$$\gamma = \frac{v_t d_{plastic}}{V_{total}} = \frac{v_p N d_{plastic}}{V_{total}} \quad 2.25$$

where $d_{plastic}$ is the microplastic density, and N is the number of spheres in the sample. By substituting the equations recursively, the final value of the permittivity is obtained as:

$$\varepsilon_{r,\text{eff}}(f) = \varepsilon_r - \left[\frac{\left(\varepsilon_r - \varepsilon_{r,\text{eff,dc}}(\gamma)\right)}{P(f)}\right] \quad 2.26$$

and its derivative is given by:

$$\left|\frac{\partial(\epsilon_{r,eff})}{\partial\gamma}\right| \quad 2.27$$

As the resonator's sensitivity depends on the concentration of microplastics in the test environment, which is a function of both the individual particle volume and the overall volume present in the water sample. Figure 2.6 shows the effective permittivity of the microstrip when water containing different concentrations of microplastic is present. The real part of the permittivity (blue) decreases slightly as the microplastic concentration increases, indicating a change in the dielectric environment due to the added microplastic particles. Meanwhile, the imaginary part (red), which relates to losses in the material, remains almost constant across different concentrations. This slight decrease in the real part suggests that even small amounts of microplastic alter the effective dielectric properties of the medium, which could be used to detect low concentrations of microplastics.

Figure 2.7 presents the derivative of the effective permittivity concerning concentration, highlighting how sensitive the sensor is to changes in concentration. A higher derivative value implies that the sensor is more responsive to changes in microplastic concentration within the tested range. Here, the real part of the derivative is nearly constant, suggesting a uniform sensitivity level across concentrations. This consistency in sensitivity is crucial for developing a reliable detection system, as it indicates that the sensor can reliably differentiate between low and high concentrations of microplastic in water.

Figure 2.6- Real (blue) and imaginary (red) part of the effective permittivity ($\varepsilon_{r,\text{eff}}(f)$) of the microstrip with water containing various concentrations of microplastic.

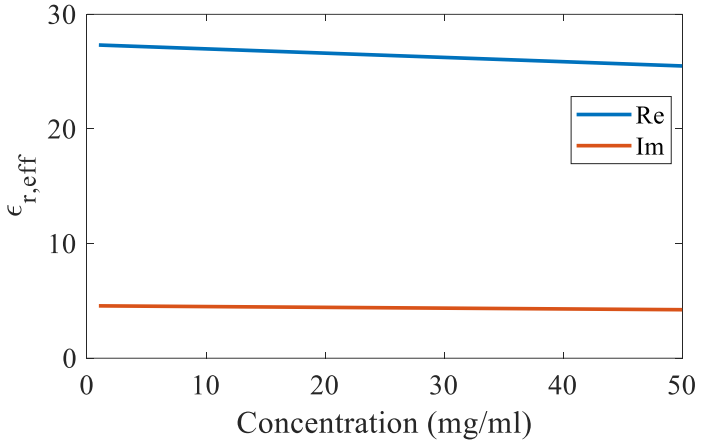

Figure 2.7 - Derivative of the effective permittivity ($\frac{\partial(\epsilon_{r,eff})}{\partial\gamma}$) with respect to microplastic concentration

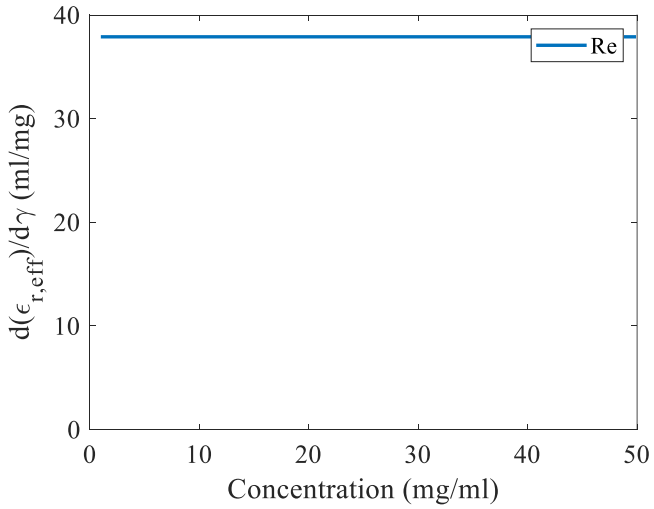

2.5. CIRCUIT FABRICATION

For the bench tests, the circuits were fabricated using photosensitive ink for the photolithography method. For this research, the **photolithography** technique was chosen due to its precision and suitability for producing fine circuit patterns on a PCB substrate. Photolithography is a process that uses light to transfer a geometric pattern from a photomask onto a photosensitive material. This technique is widely used in PCB manufacturing because it enables accurate and repeatable etching of intricate designs necessary for high-frequency resonators [108]. The photolithography process for this project includes several key steps:

- *Preparation of the Photomask:* The process begins by creating a photomask that matches the HFSS resonator design. A scaled-down cutout of the resonator was exported from HFSS and pasted into a Word document to verify dimensions. Adjustments were made to ensure precise alignment, and the PCB areas with no conductive material (circuit pathways) were filled in black. The finalized image was printed on a transparent sheet, which serves as the photomask.
- *Coating the PCB with Photosensitive Ink*: The PCB board is coated with a photosensitive layer. This photosensitive ink hardens when exposed to light, forming a resist pattern that protects the copper areas during etching. The coating must be even and consistent to achieve accurate exposure.
- *Mask Application under Dark Lighting*: In a low-light environment (to prevent unintentional exposure), the transparent photomask is carefully aligned and placed on top of the PCB coated with photosensitive ink.
- *Exposure to UV Light:* The masked PCB is then exposed to UV light, which hardens the exposed ink areas that represent the circuit design. Areas protected by the black portions on the mask remain unaffected, allowing for selective etching later.
- *Development:* After exposure, the PCB undergoes a developing process to reveal the circuit pattern. The developer removes the unexposed areas of the photosensitive ink, revealing the copper underneath while preserving the ink-covered circuit paths.
- *Etching:* The PCB is then submerged in an etching solution, typically ferric chloride or another copper etchant, which removes the unprotected copper, leaving only the desired circuit design intact.

- *Final Cleaning and Sizing:* Any remaining photosensitive layer is removed after etching. The PCB is cleaned to remove residue and then cut to match the exact dimensions of the model specified in HFSS.

Following these steps allows precisely fabricating the resonator models, providing physical structures that closely resemble the simulated designs. This ensures that the experimental testing of these resonators accurately represents the anticipated results, allowing for a direct comparison and validation of the simulation predictions.

2.5.1. PREPARATION OF THE PHOTOMASK:

With the image correctly positioned and scaled, the areas representing conductive paths on the PCB (the circuit traces) were left transparent, while the remaining areas were filled in black. This preparation technique is essential because the final image will be printed on a transparent sheet as a photomask. When the photomask is placed on the PCB coated with photosensitive ink, the darkened areas will block UV light, preventing exposure. Meanwhile, the transparent areas will allow UV light to pass through and directly reach the photosensitive coating on the PCB.

Figure 2.8 - Photomask Layout Showing Darkened Non-Circuit Areas and Transparent Circuit Traces

This selective exposure technique ensures that the UV light hardens only the areas intended to remain in the final circuit. In contrast, unexposed areas will be removed during the development and etching stages. **Erro! Fonte de referência não encontrada.** illustrates the photomask preparation, with dark areas corresponding to non-circuit regions and transparent areas indicating the circuit traces.

2.5.2. COATING THE PCB WITH PHOTOSENSITIVE INK

The next crucial step in the fabrication process was coating the PCB with photosensitive ink. This step required precision to ensure a uniform application of the ink, which is vital for consistent exposure and pattern transfer during the photolithography process. For this task, a syringe was used to dispense controlled drops of photosensitive ink onto the surface of the PCB. The PCB was then mounted on a spinner (a device specifically designed for coating substrates) set to rotate at 2000 rpm for 45 seconds. This high-speed rotation spread the ink evenly across the surface, ensuring a thin and uniform coating.

Figure 2.9 - PCB Coated with Photosensitive Ink, Prepared for Photolithography. The solid curves represent the next step while the dotted lines represent the name of the process or an element or component. The process in a) is to remove the photosensitive ink with a syringe, in b) the ink is being injected into the PCB, c) the spinner was attached to execute the configured programming (time and speed) in d) the PCB was placed on the hot plate to dry for 90 seconds at 150 degrees and in d) the PCB is ready to be used.

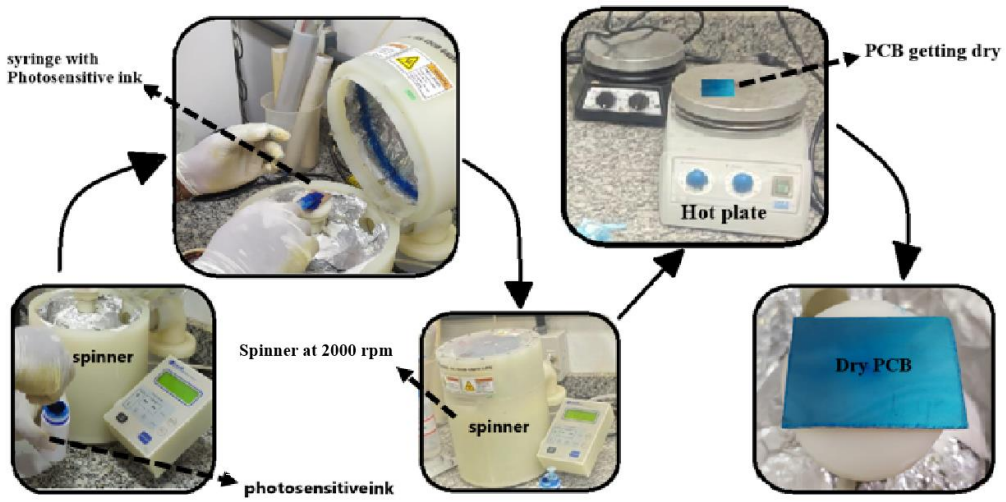

The choice of rotation speed and duration is critical. A consistent speed of 2000 rpm provides enough centrifugal force to distribute the ink without creating gaps or uneven areas. The 45-second duration allows the ink to level out before drying starts. If the ink is not evenly applied, the thickness may vary, leading to issues in later stages, such as uneven exposure during UV light processing. Uneven coatings can result in sections of the PCB taking longer to cure or dry, complicating the exposure process and making it difficult to develop the circuit pattern correctly.

Once the PCB was fully coated with the ink, a visual inspection was conducted to ensure there were no visible irregularities. If any unevenness or defects were detected, the PCB was returned to the spinner, and the coating process was repeated. If the coating was uniform, the

PCB was then carefully transferred to a hot plate set at 150°C for 90 seconds. This heating step helped to partially cure the photosensitive ink, ensuring it adhered properly to the PCB while avoiding complete drying. Handling the PCB at this stage required care, as the heat left it hot to touch, and the ink remained somewhat tacky.

After being removed from the hot plate, the PCB needed to be placed in a low-light or dark environment. This precaution prevented premature exposure to ambient light, which could partially activate the photosensitive ink and compromise the quality of the circuit pattern. Proper storage ensured that the ink remained stable until the photomask could be applied in the next step of the process. The final result of the coated PCBs, prepared and ready for the photolithography step, is shown in **Erro! Fonte de referência não encontrada.**.

2.5.3. MASK APPLICATION UNDER DARK LIGHTING

The next step in the photolithography process was the application of the photomask under controlled lighting conditions. This step required the printed mask on a transparent sheet to be precisely aligned and placed on top of the PCB that had been previously coated with photosensitive ink. It was essential to carry out this task in a low-light or dark environment to prevent any unintended exposure of the photosensitive layer to ambient light, which could compromise the pattern transfer. To begin, the transparent photomask was positioned carefully over the PCB, ensuring that the circuit design aligned perfectly with the coated surface. This alignment step is critical; even the slightest shift could result in a misaligned pattern, leading to inaccuracies in the final circuit. Once the photomask was accurately positioned, a glass plate was gently placed on top to secure it and maintain the mask's position throughout the exposure process. The added weight of the glass ensured that the photomask was in close contact with the photosensitive layer, preventing any light from scattering underneath and blurring the circuit pattern.

With the photomask securely in place, a 100-watt UV light source was turned on and directed at the assembly for exposure. The exposure time for this process was set to 8 minutes, but this duration can vary depending on the intensity and specifications of the UV light used (seen in Figure 2.10). The goal was to provide enough UV exposure to harden the photosensitive ink in the areas not covered by the dark regions of the mask, creating a precise resist pattern on the PCB. It is important to note that in other cases, with different UV light

sources or intensities, the exposure time may need to be adjusted—either shortened or lengthened—to achieve optimal results.

Once the exposure was complete, the UV light was turned off, and the glass plate and photomask were carefully removed. At this stage, the PCB was ready for the development process, where it would be placed in a developer solution to reveal the circuit pattern. This solution dissolved the unexposed areas of the photosensitive ink, uncovering the copper beneath, while leaving the UV-hardened areas intact to form the desired circuit layout. Proper handling and timing in this step were crucial to ensure a clean, sharp pattern that matched the original design.

Figure 2.10 - Transparent photomask was positioned carefully over the PCB

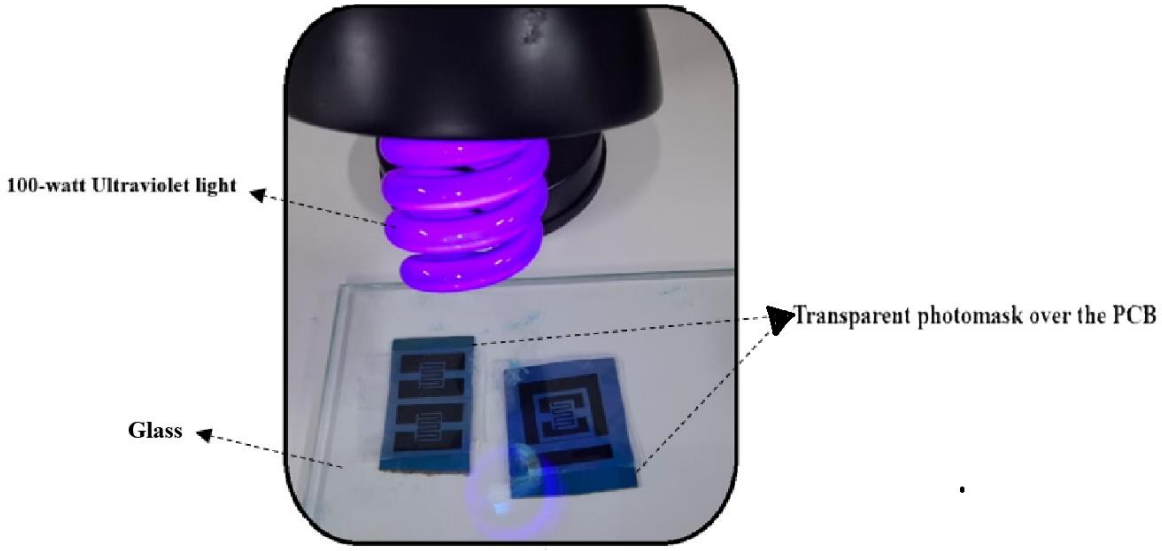

2.5.4. CHEMICAL PROCESSING OF THE PCB

After the PCB has been exposed to UV light and the circuit pattern has been set, the next step involves a series of chemical treatments to develop and etch the circuit. This process ensures that the unneeded copper is removed, leaving only the desired circuit traces intact. The PCB is successively placed into three different chemical solutions, each serving a specific purpose.

2.5.4.1. SODIUM CARBONATE (DEVELOPER STAGE):

The first step is to immerse the PCB in a solution of sodium carbonate. This solution is prepared by mixing sodium carbonate with water to create a concentration suitable for developing the exposed PCB. The purpose of this solution is to dissolve and remove the photosensitive ink in areas that were not exposed to UV light (i.e., areas that were shielded by the dark portions of the photomask). This step acts as a preparatory phase for copper etching, as it exposes the copper surface that needs to be removed.

During this phase, the PCB should be gently agitated to ensure that all unexposed ink dissolves evenly. The solution works by softening the unexposed ink, allowing it to be easily washed away, while the UV-cured ink remains adhered to the copper, protecting it from the subsequent etching process. Once the unexposed areas are clear, the PCB is rinsed with water to remove any residual developer solution.

Figure 2.11 - Sequential Stages of PCB Processing a) PCB with Mask Applied Under UV Light Exposure, b) PCB Immediately After UV Light Exposure, c) PCB Immersed in Sodium Carbonate Solution for Development, d) PCB with Unexposed Ink Removed After Development, e) PCB Rinsed and Dried After Development, f) Materials for Preparing the Ferric Chloride Solution (Etching Stage), g) PCB in Ferric Chloride Solution Undergoing Etching h) Fully Etched PCB Displaying Completed Circuit Pattern.

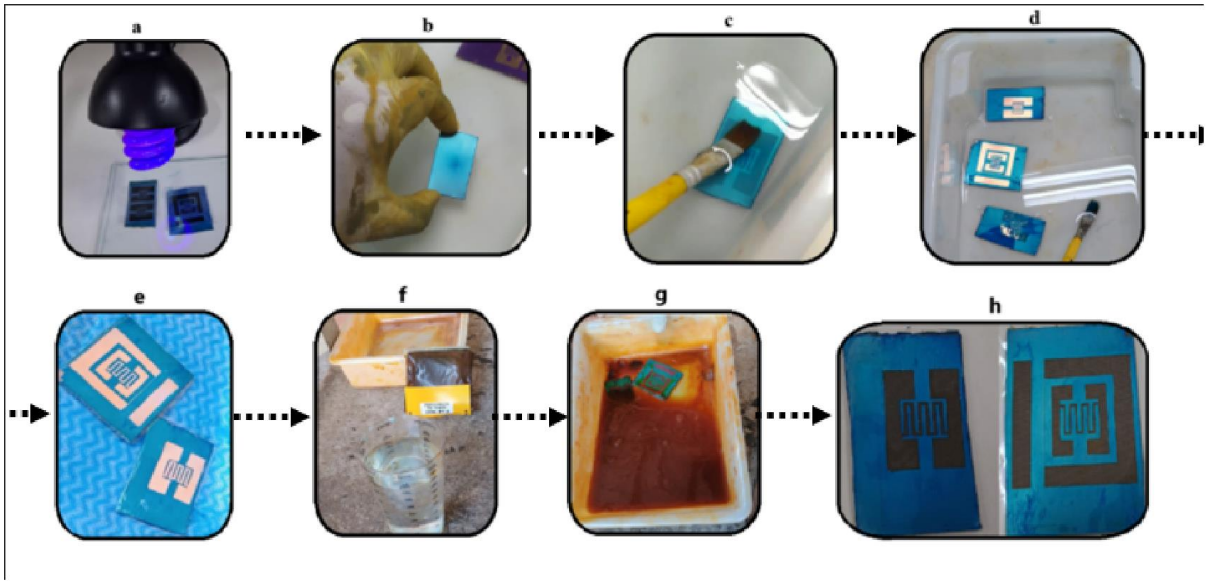

2.5.4.2. FERRIC CHLORIDE SOLUTION (ETCHING STAGE):

Following the development process, the PCB is submerged in a ferric chloride solution to etch away the unwanted copper. The solution is typically prepared by dissolving 50 grams of ferric chloride in 0.5 liters of water, resulting in a mixture capable of effectively etching the

copper layer. Ferric chloride reacts with copper, breaking it down and dissolving it, leaving behind only the sections protected by the UV-cured ink.

This step is critical, as it determines the precision and quality of the final circuit. The PCB should be left in the etching solution for approximately 10 to 20 minutes, with occasional gentle agitation to ensure uniform etching. Progress should be closely monitored to avoid over-etching, which could damage the circuit traces. Once all the unwanted copper has been removed, the PCB is carefully rinsed with water to halt the etching process as shown in **Erro! Fonte de referência não encontrada.**.

2.5.4.3. SODIUM HYDROXIDE (INK REMOVAL STAGE):

The final step involves removing the cured photosensitive ink to reveal the completed copper circuit. This is done by immersing the PCB in a solution prepared with 20 grams of sodium hydroxide in 0.5 liters of water. Sodium hydroxide acts as a stripping agent, dissolving the hardened ink without affecting the copper underneath. The PCB should remain in this solution for approximately 10 minutes. During this time, the cured ink will dissolve, exposing the clean copper circuit beneath. After the ink has been completely removed, the PCB is rinsed thoroughly with water to ensure no residue remains.

Once these steps are complete, the PCB should display the desired circuit pattern clearly, as shown in Figure 2.12. This process results in a high-precision circuit ready for further testing and integration into the project. Proper handling and timing at each stage are essential to maintain the quality and accuracy of the fabricated circuit.

In addition to the circuit design, SMA connectors were installed at the ends of the microstrip line, using conventional soldering techniques (Solder Figure). The circuit was complete and ready for bench tests using the Vector Network Analyzer (VNA). To ensure precise measurements, the VNA was calibrated using a 50Ω calibration kit, ensuring impedance matching between the instrument and the circuit, thus optimizing the results. A photograph of the fabricated circuits can be seen in Figure 2.12.

Figure 2.12 - Final Stages of PCB Fabrication and Cleaning Process. a) PCB Fully Etched as the Starting Point (Referencing Figure 4.3h), b) PCB Placed in Sodium Hydroxide Solution for Ink Removal, c) Ink Removal Process in Progress Within the Solution, d) PCB with All Ink Removed, Exposing the Circuit, e) Completed PCB Ready for Testing.

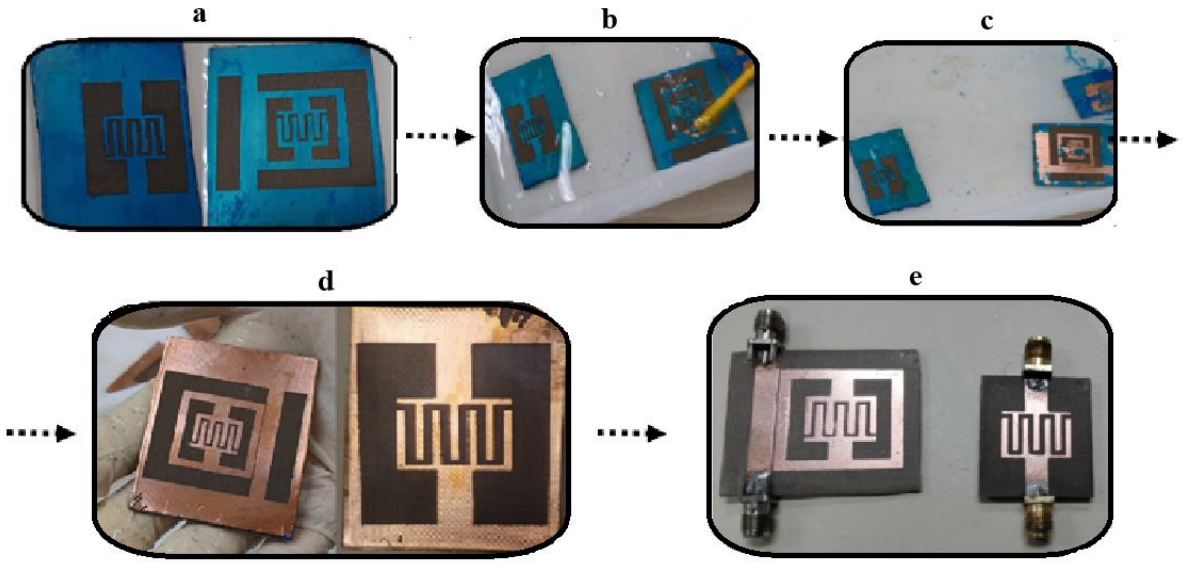

2.6. MICROFLUIDICS

The fabrication of the microfluidic channels, as illustrated in Figure 2.13, begins with creating a detailed computational model of the mold to be used. This model is digitally designed to ensure that the final microfluidic channel meets the exact specifications necessary for testing and experiments. The computational model is then transferred to a ceramic 3D printer, which is used due to its ability to create highly precise and durable molds. Ceramic printing is particularly advantageous because it provides a robust mold that can withstand the PDMS molding process without deforming.

After printing the ceramic mold, the PDMS (Polydimethylsiloxane) mixture is prepared. PDMS is a silicone elastomer that offers flexibility, transparency, and biocompatibility. It is ideal for microfluidic applications because it allows direct observation of liquid flow and is chemically inert, preventing unwanted interactions with the tested fluids. The PDMS mixture is made using SYLGARD™ 184 Elastomer, which includes a base silicone and a curing agent. These components are mixed in specific proportions to ensure the correct formation of the material.

Figure 2.13 –Microfluidic channel fabrication process. The procedure includes (1) computational modeling of the mold, (2) ceramic mold printing using a 3D printer, (3) preparation and curing of the PDMS silicone elastomer in the mold, and (4) removal of the cured microfluidic channel, ready for use in detection experiments.

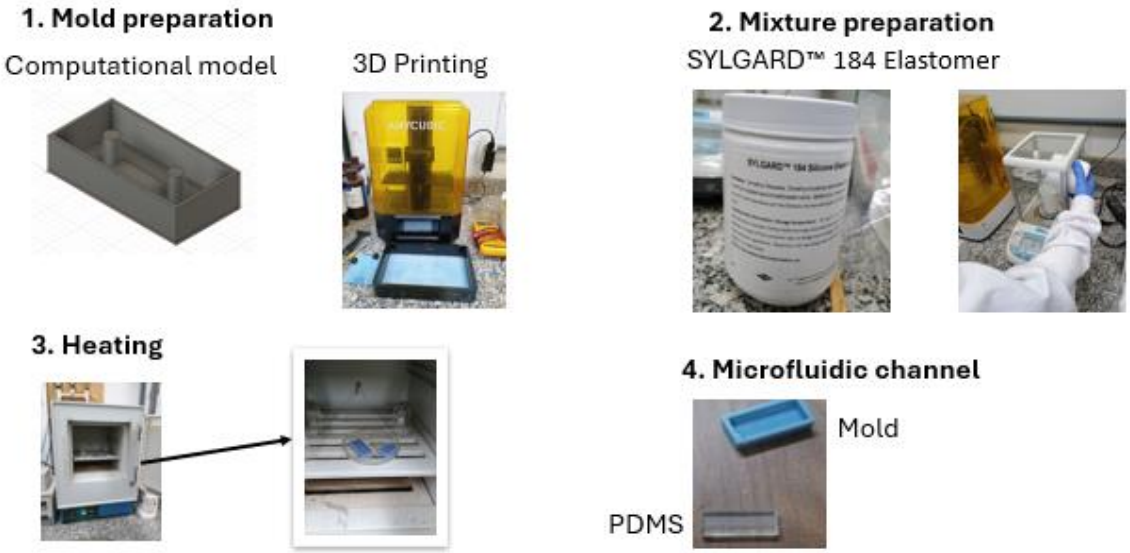

The prepared mixture is carefully poured over the ceramic mold, and the assembly is then heated to accelerate the PDMS's curing. The heating is done in an oven, where the PDMS remains for sufficient time to ensure that the material solidifies uniformly, taking on the exact shape of the mold. Once cured, the PDMS is removed from the ceramic mold, revealing the final microfluidic channel. This channel is transparent, facilitating observation during experiments, and maintains the designed shape and dimensions, making it suitable for microplastic detection tests. The microfluidic channel is placed above the fabricated circuit, as shown in Figure 2.13.

Figure 2.14 - Microfluidic channel installed above the fabricated circuit.

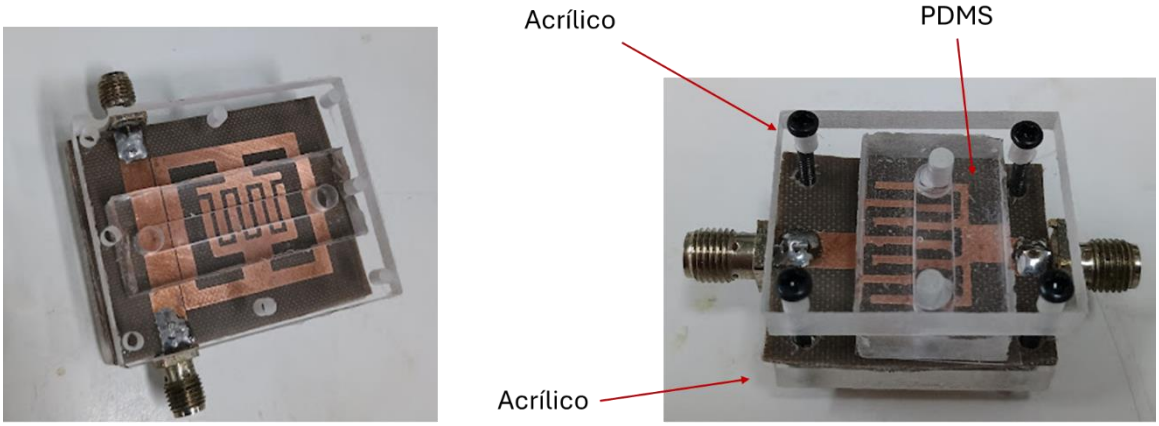

2.7. MICROPLASTIC PRODUCTION

The process of generating microplastics begins with manually cutting polyethylene terephthalate (PET) plastic bottles, which are reduced into smaller, more manageable pieces (Figure 2.15). This initial cutting is done carefully to ensure that the material can be properly processed in the subsequent stages. The plastic pieces are then fed into a high-speed mill, which grinds the material until it reaches standardized sizes. The mill uses sharp blades to break the plastic into smaller particles suitable for sensitivity detection tests. This grinding step is essential to ensure that microplastics have controlled dimensions, which is fundamental for standardizing experiments.

Figure 2.15 –Preparation of microplastics for detection tests. After manually cutting PET bottles, the plastic is ground in a mill to standardize sizes and then sieved. The resulting particles are separated into different sizes and mixed with deionized water to create suspensions of 150 µm, 300 µm, and 1 mm, ready for experiments.

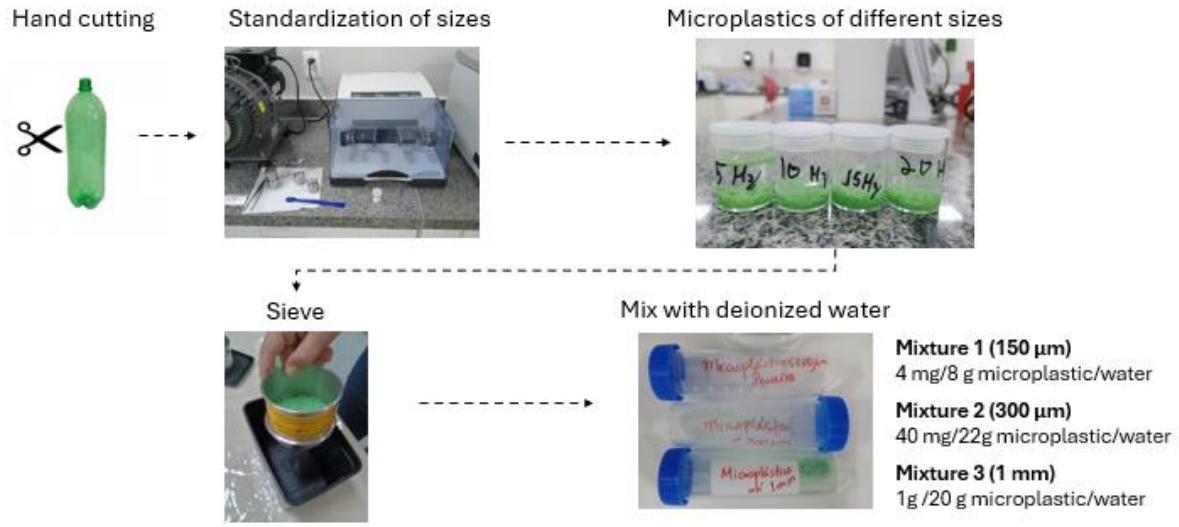

After the grinding process, the microplastic particles are passed through a sieve, which separates them into specific size ranges (Figure 2.15). The sieve ensures that the samples are uniformly distributed into predefined size categories, such as 1 mm, 300 µm, and 150 µm. The resulting particles are then stored in labeled containers according to their size, facilitating the control of variables in the experiments. Precise size separation is crucial, as it allows for the evaluation of the detection sensors' effectiveness in identifying microplastics of different dimensions and helps create consistent samples for testing.

CHAPTER 3

3. SIMULATION

The use of radio frequency (RF) resonators to detect microplastic particles in water presents a promising approach due to their sensitivity to changes in permittivity. Microplastics, which have different dielectric properties compared to water, alter the resonant frequency of an RF resonator when present in the material under test (MUT) [35][109]. This frequency shift can be detected using a vector network analyser (VNA), allowing for the identification of microplastic contaminants [110]. Before manufacturing the resonator, simulating the device using specialized electromagnetic simulation software, such as Ansys HFSS (High-Frequency Structure Simulator), is crucial. HFSS allows for a detailed analysis of how the resonator will behave under real-world conditions, helping to predict the electromagnetic response, verify the design, and ensure optimal performance within the desired frequency range of 1 to 6 GHz. Simulation is necessary for several reasons such as:

Cost and Time Efficiency: Building physical prototypes is costly and time-consuming. Simulating the device allows design errors or performance issues to be identified and rectified before committing to fabrication, saving resources.

Accurate Prediction of Resonant Behavior: The simulation provides insight into how the structure resonates, allowing for the tuning of dimensions to ensure the desired frequency response.

Assessment of Interaction with the Environment: Water, as the MUT, has higher permittivity than air, which can significantly affect the resonant frequency. Simulation can model the interaction between the resonator and water, helping to predict how the device will behave in detecting microplastics.

Design Optimization: HFSS enables the optimization of parameters such as the resonator's geometry, material properties, and substrate choice, ensuring the best performance within the given frequency range.

3.1. SENSOR'S TOPOLOGY

The resonator's design is critical to its performance, particularly in achieving the desired resonant frequency for a range of 1 to 6 GHz. The dimensions of the resonator, especially its length, width, and spacing between interdigital fingers, directly affect the resonant frequency, which is determined by the geometry of the device concerning the wavelength of the electromagnetic waves at that frequency [111]. To achieve the desired performance, several factors must be considered in determining the dimensions. For instance, an RF resonator's dimensions are directly related to its operating frequency due to the principles of electromagnetic wave propagation. In simple terms, for the resonator to function effectively at a specific frequency, its geometry must align with the corresponding wavelength of the electromagnetic waves. This is particularly true for a printed RF interdigital resonator on a Rogers/5880 PCB, where the material's properties, such as its dielectric constant, and the resonator's physical dimensions, play crucial roles in ensuring optimal performance across the target frequency range [39][112]. In an RF resonator, the dimensions are often designed to be a fraction of the wavelength, depending on the type of resonator [112].

- *Resonant Frequency and Length*: The resonant frequency of an RF resonator is inversely proportional to its effective length. The resonator's effective length (L) can be calculated using the relationship:

$$f_r = \frac{c}{2L\sqrt{\epsilon_{\text{eff}}}} \tag{3.1}$$

  where (f_r) is the resonant frequency, (c) is the speed of light in vacuum, (ϵ_{eff}) is the effective permittivity of the microstrip above the substrate material (Rogers 5880) (section 2.4). Since we aim to operate within the 1 to 6 GHz range, the length must be chosen such that the fundamental mode of resonance falls within this range.

- *Substrate and Dielectric Constant*: The selection of Rogers 5880 as the substrate, with a dielectric constant $(\epsilon_r = 2.2)$ and a low loss tangent of 0.0009, is crucial in minimizing losses and ensuring stable resonant performance across a wide frequency range. The effective permittivity (ϵ_{eff}) depends on the resonator's geometry and the proportion of the electromagnetic field confined within the substrate versus the surrounding medium. Typically, (ϵ_{eff}) is slightly less than (ϵ_r) because some of the fields extend into the air (or a mixture of water and plastic).

- *Width and Finger Spacing*: The width of the resonator and the spacing between the interdigital fingers affect the coupling strength and quality factor (Q-factor) of the interdigital resonator (section 2.5). Narrower spacing increases capacitive coupling, enhancing the sensitivity of the resonator to dielectric changes caused by microplastic particles in water. However, the spacing must be optimized to avoid excessive parasitic capacitance, which could lower the resonator's Q-factor and degrade its performance.
- *Effective Permittivity:* The effective permittivity (ϵ_{eff}), which is influenced by both the substrate material and the surrounding medium (air and water), impacts the resonator's frequency response. By simulating the resonator with water as the MUT, we can predict how the resonant frequency will shift in the presence of microplastics, helping to fine-tune the resonator's dimensions for optimal sensitivity.

3.2. INTERDIGITAL RESONATORS CHOICE

Several key factors drive the choice of an interdigital resonator for this application, such as.

- **High Sensitivity to Permittivity Changes**: Interdigital resonators are sensitive to small variations in the dielectric constant of the surrounding medium, making them ideal for detecting microplastics in water.
- **Compact Size**: They provide high resonant frequency performance in a compact, planar structure, important for devices operating at frequencies up to 6 GHz.
- **High Q-Factor**: These resonators exhibit a high-quality factor (Q-factor), which ensures sharp frequency response and enhances the detection of small frequency shifts. Q-factor is calculated using the formula $\mathrm{Q} = \frac{\mathrm{f_r}}{\Delta \mathrm{f}}$, $\mathrm{Q} = \frac{f_{\mathrm{res}}}{f_{\mathrm{high}} - f_{\mathrm{low}}}$, where f_{res} is the resonant frequency, and f_{low}, f_{high} are the -3dB points around the peak.
- **Ease Fabrication**: Interdigital resonators are relatively simple to fabricate using standard PCB manufacturing techniques, which reduces cost and complexity.

To design an RF resonator for a target operating frequency, we start by calculating the resonator's effective length. For this example, we aim for a 6 GHz frequency. Where, Speed of light is represented by ($c = 3 \times 10^8$ m/s), is the target resonant frequency, effective

permittivity ($\epsilon_{eff} \approx 1.9$). The resonator length (L) is determined by substituting the known values, in formula 3.1.

Solving for (L), $L = 18.1$ mm. Adjusting for Lower Frequencies. For a lower frequency, such as 1 GHz, the resonator length increases. Using the same formula, $L = 108.8$ mm. These calculated values serve as the foundation for designing the resonator. With these dimensions, we can begin the circuit simulation process and assess the design's performance in meeting the required parameters. Notice that their dimensions are just to give an idea of the ideal dimensions of the resonator. In the simulation, we need to consider the microfluid channel, water and the microplastics, which alter these values. Moreover, interdigital is also important, since the inductive and capacitive parameters influence the resonant frequency.

3.3. SIMULATION SETUP AND ADJUSTMENTS

Before starting the simulation, the microstrip transmission line dimensions were calculated using an impedance calculator from [113] to ensure a 50-ohm impedance. Key input parameters included, PCB thickness, dielectric thickness (h), Relative dielectric constant ($\epsilon_r = 2.2$). The calculator provided the necessary transmission line width (W_{50}) to meet the 50-ohm impedance requirement, as illustrated in Figure 3.1.

Figure 3.1 - Design of the Proposed RF Resonator Topology and Its Arbitrary Dimensions

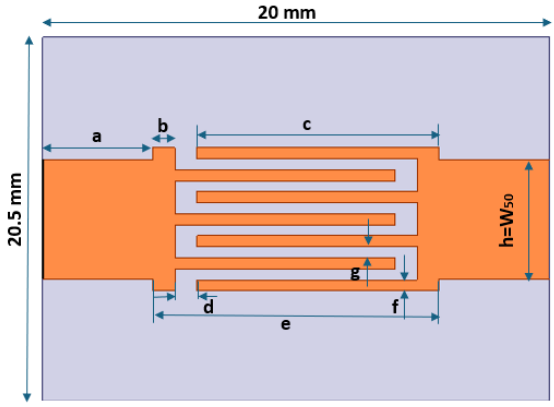

For the resonator, although the calculated length for 6 GHz was approximately 18.1 mm, the actual resonator length was adjusted to 20 mm. This change was made to simplify the design and accommodate the spacing between interdigital fingers while still maintaining operability across the 1-6 GHz range. This slight increase in length allows flexibility without sacrificing

performance at higher frequencies. It also offers greater ease in fabrication and tuning during the simulation stage.

The resonator and transmission line designs were subsequently input into the Ansys HFSS software for detailed simulation. Figure 3.1 shows the simulation setup, and Table 3.1 presents the complete set of dimensions used, including length, width, and interdigital finger spacing. These dimensions are critical for ensuring the resonator operates as expected within the 1-6 GHz range, as they directly impact the device's electromagnetic behavior and resonant frequency. Simulation results will verify that all key parameters such as resonant frequency and impedance matching align with the design goals.

Once the design with the dimensions is set up, it's time to calibrate the ANSYS HFSS software to simulate real-world conditions as closely as possible. The first step is to define the conductive materials on and under the PCB as "Perfect E," which means they are treated as perfect electric conductors (PEC). Next, the input and output ports are configured as "Lumped Ports," which simulate the electrical connections as small, concentrated sources of current and voltage. These ports represent how the device will interact with external circuits, such as a vector network analyzer (VNA). A simulation boundary is then created around the PCB in the form of a box, with dimensions set to more than the wavelength of the lowest frequency under analysis. This box serves to mimic the open space around the resonator and is crucial for modelling radiation effects. The faces of the box surrounding and on top of the PCB are defined as "Radiation Boundaries," allowing the electromagnetic waves to radiate outward, just as they would in free space.

After setting up the physical aspects of the simulation, the next step is to configure the simulation parameters. The frequency range is set with a maximum of 6 GHz, and the simulation is allowed to run for 31 passes with a maximum delta-S of 0.001, ensuring high precision in the final results. Additionally, a frequency sweep is added, covering the range from 1 GHz to 6 GHz with a step size of 0.001 GHz. This provides detailed data across the entire operational frequency range.

Once all the settings are in place, it is important to perform a validation check to ensure there are no warnings or errors in the setup. This step confirms that the simulation can run smoothly and that all boundary conditions, material definitions, and port configurations are correctly applied.

Variables	Dimensions[mm]
a	5
b	1
c	10
d	1
e	12
f	0.5
g	0.5
h	5.4

Table 3.1 - Initial Dimensions of the variables for the Proposed RF Resonator Topology.

With everything ready, the "Analyze All" button is clicked, initiating the simulation. After a period of computation, the results can be observed. The output shows a blue curve representing the transmission parameter (S_{21}), with two resonant frequencies observed at 1.88 GHz and 2.79 GHz, with magnitudes of 35.6 dB and -52.34 dB, respectively. These results are shown in Figure 3.2, where the green curve represents transmission(S_{21}). and the blue curve represents reflection (S_{11}).

Figure 3.2 – Results of S-parameter response, where the green curve represents transmission ($S21$)and the blue curve represents reflection ($S11$), the resonant frequency is the peak of the S_{21} curve

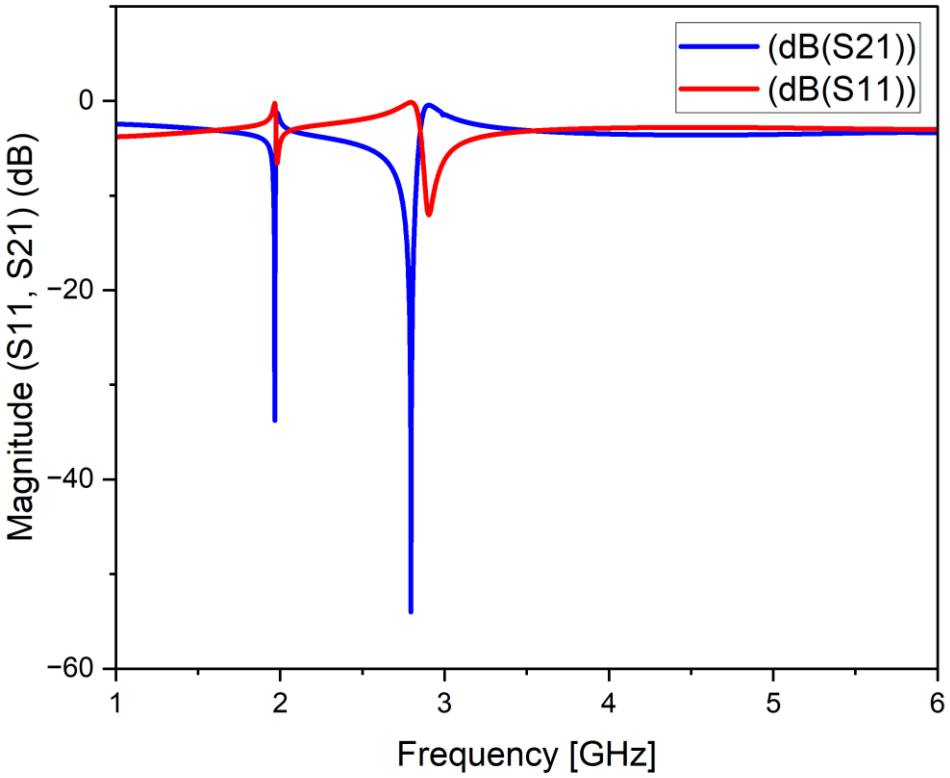

The first observation is that the proposed topology is sensitive, as evidenced by the distinct resonances. The resonator responds well within the desired frequency range, making it a promising candidate for the intended application. Further optimization may improve its performance, but the initial results are promising.

As mentioned earlier, the dimensions of the simulated circuit were chosen arbitrarily. However, two of the three fundamental characteristics expected from the device have been demonstrated: sensitivity and a good Q-factor (>50). Now, the final task is to confirm that the device is sensitive to microplastics, which is the primary objective. While the current design performs well, there is potential for further optimization by adjusting the circuit dimensions to achieve the best possible version of the resonator. To optimize the design, the "Optimetrics" tool in ANSYS HFSS was employed, which allows for automatic variation of the circuit's dimensions. Variables such as (a), (b), (c),(d), (e), (f), (g), and (h) were simultaneously altered, starting from the minimum length calculated for a frequency range between 3 GHz and 6 GHz.

Moreover, one critical aspect to monitor during simulation is the **meshing** quality, as it directly impacts the accuracy and stability of the results. For both circuit models, a mesh error tolerance of 0.002 was used. This value indicates the maximum permissible error in mesh cell size relative to the wavelength, ensuring a balance between precision and computation time. Using finer mesh (smaller mesh cells) increases simulation accuracy by capturing more details of the fields and currents, but it also increases computational demands.

If the mesh quality appears inadequate or the results are inconsistent, adjusting the mesh cell length is often an effective approach. By reducing the cell length, the simulation captures more geometric and field details, which can improve the accuracy. This refinement is particularly important in areas with high field intensity or in regions of complex geometry, as finer meshing captures subtle variations in electromagnetic behavior.

In cases where the mesh quality remains insufficient after adjustments, it may be helpful to conduct localized meshing for specific regions rather than applying a fine mesh across the entire model. This approach optimizes resources, targeting critical areas without significantly increasing the overall simulation time.

Finally, testing the two models with incremental changes in mesh resolution helps verify that results are consistent and unaffected by mesh-related errors. Conducting this validation

across both circuit models ensures that the simulations are reliable and that the conclusions drawn from the results are robust. An illustration of the mesh is shown in Figure 3.3.

Figure 3.3 - Mesh Design and Optimization for Accurate RF Circuit Simulation with an error of 0.002.

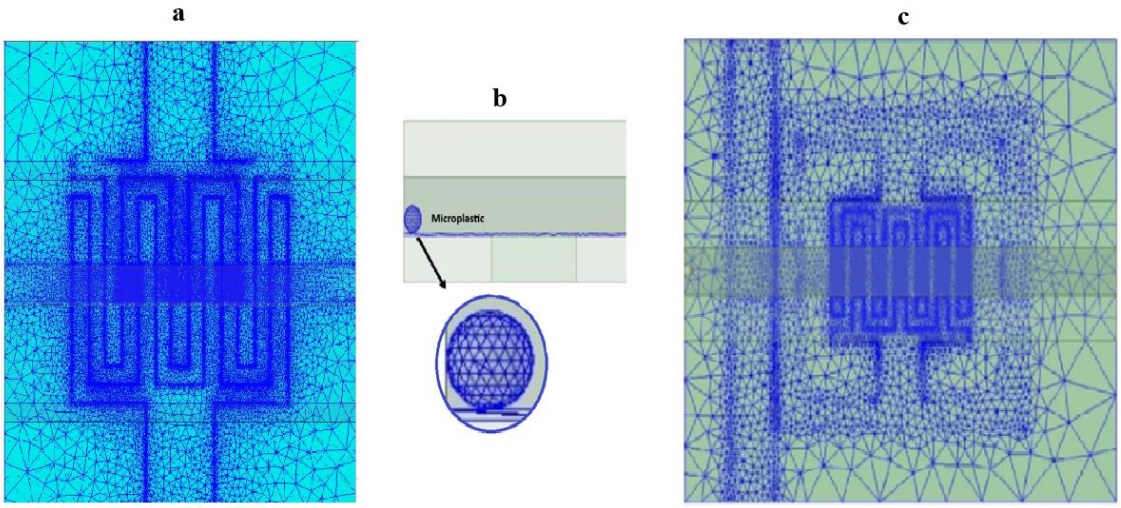

3.4. OPTIMIZATION QUASI-NEWTON

The "Quasi-Newton" method was selected for this process, which is particularly useful in optimization problems because it provides efficient convergence when searching for a minimum. This method incrementally adjusts the dimensions with a step size of 0.1 mm. The advantage of the Quasi-Newton approach is its ability to find an optimal solution by reducing the computational load compared to other methods like full-gradient searches, making it ideal for fine-tuning complex designs such as RF resonators.

For each variation of the dimensions, HFSS generated a new curve of the S-parameters, including both (S_{21}) (transmission) and (S_{11}) (reflection). This iterative process was repeated until the design with the best performance, characterized by the sharpest resonance frequency and improved S-parameters, was identified. The S-parameters of some points of the optimizations are shown in Figure 3.4.

After analyzing the resulting curves, the dimension set with the optimal performance was selected. The final optimized resonator demonstrated improved resonant behavior, sensitivity, and Q-factor (74.11). The dimensions of this optimized design are presented in Table 3.2, showing the updated values for the key parameters that contributed to enhanced performance.

Figure 3.4 – Optimized by Quasi-Newton: S-Parameter Response Curves for Variable Resonator Dimensions (a), (b), (c),(d), (e), (f), (g), and (h).

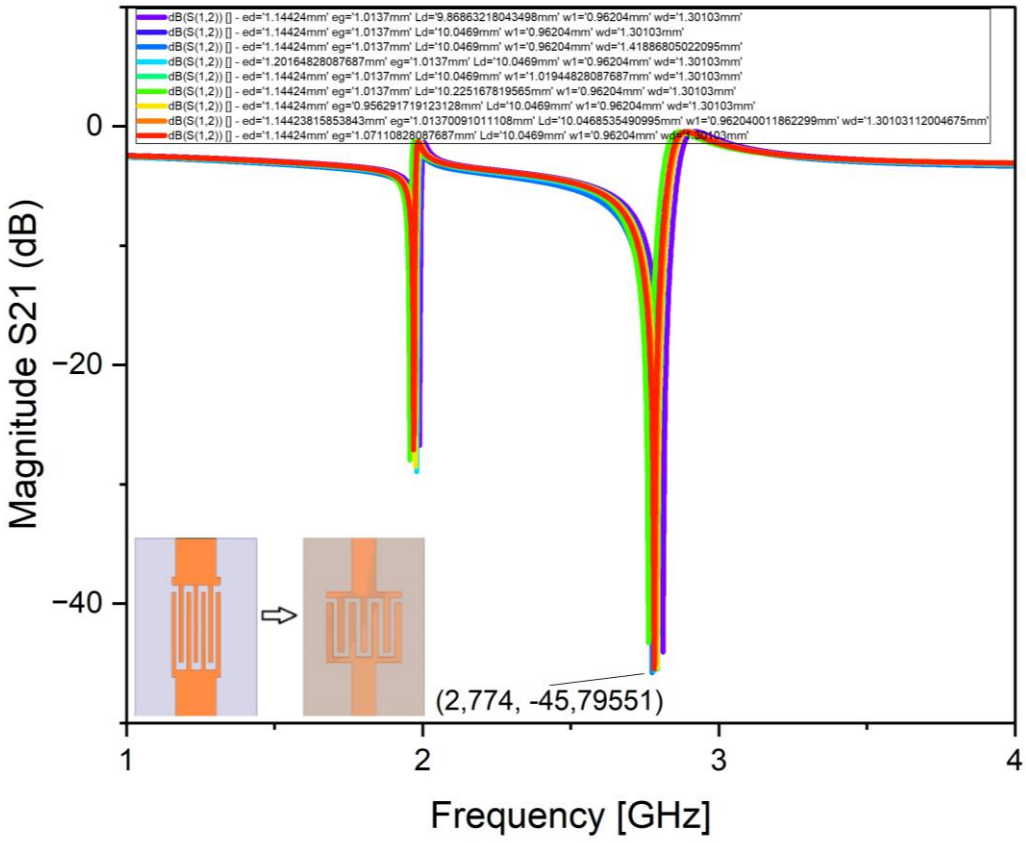

By refining the design in this manner, the resonator is now well-suited to its intended application, and the improved sensitivity will enhance its ability to detect microplastics in water.

Figure 3.5 – Final Circuit Design with Optimized Dimensions for Variables *a, b, c, d, e, f, g, h*.

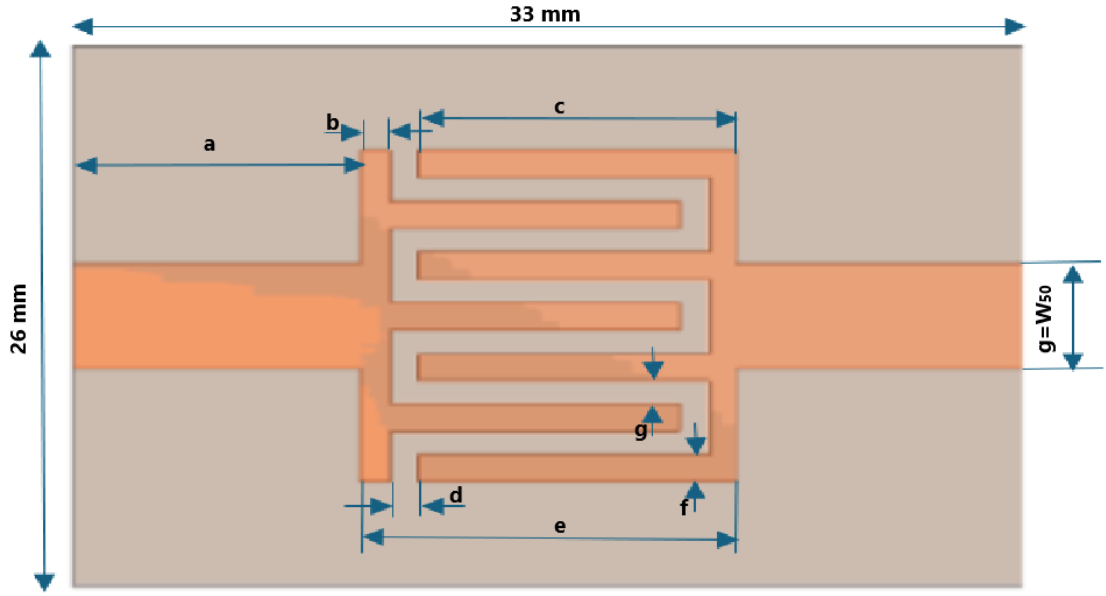

Variable	Dimension [mm]
W50	5.1
a	5
b	0.96
c	10.05
d	1.30
e	1.14
f	1.3

Table 3.2 - Final dimensions of the proposed resonator.

Now that it has confirmed the optimized dimensions of the circuit, it's time to proceed with the characterization of the device. This involves testing its performance under various conditions, such as unloaded, loaded, and other relevant scenarios. By doing so, we can evaluate how the resonator behaves in real-world applications, ensuring that it operates effectively within the desired frequency range. First, the unloaded condition will be tested, where no material is present to interfere with the resonator. This will serve as the baseline measurement for the device. Next, the device will be loaded with different materials, such as water, microplastic particles, and other dielectric samples, to observe how the resonant frequency shifts and to assess the device's sensitivity to these changes.

Each test will provide valuable data on the resonator's Q-factor, insertion loss, and overall sensitivity, allowing us to verify whether the device meets the design objectives. By comparing the unloaded and loaded conditions, we can determine how well the resonator detects variations in permittivity, especially with microplastics, which is the primary goal of this study. Finally, it´s will be analyzed to confirm the resonator's accuracy, stability, and robustness under different environmental conditions, ensuring that it functions as expected for its intended application.

3.5. ANALYSIS OF S-PARAMETER

With the confirmation that the device is functioning correctly and the understanding gained from the previous experience, it was decided to build a new version of the device with some modifications. This new circuit was designed to maintain the same transmission line structure

(W_{50}); however, the resonator part was slightly modified to increase the capacitance. To achieve this, the interdigital structure was confined to the center of the circuit, as shown in the figure 3.3 as sensor.

The most favorable geometric aspect to achieve a better Q-factor (quality factor) in resonators typically involves reducing losses while maintaining strong confinement of the electromagnetic energy within the resonator. Key geometric considerations for improving the Q-factor include:

Increasing the Inductor-to-Capacitor Ratio: For resonators such as lumped element or distributed resonators, an increased inductance or capacitance can contribute to a higher Q-factor. Interdigital or spiral structures with longer current paths are beneficial because they increase inductance.

Reducing Conductor Losses: Using wider or thicker conductors in the resonator reduces the resistive losses, which can improve the Q-factor. This can be especially important at higher frequencies, where the skin effect increases resistance.

Reducing Dielectric Losses: The choice of the dielectric material and its geometry are crucial. Low-loss dielectric materials should be used, and the electric field concentration in lossy materials (e.g., substrates) should be minimized. Air gaps or materials with lower dielectric constants may help reduce these losses.

These changes were made to improve the overall performance, particularly focusing on enhancing the resonance characteristics. The goal was to achieve better frequency selectivity and tuning capabilities, which are critical for the device's intended applications. The modifications will be tested and analyzed in the subsequent steps to confirm their effectiveness. Furthermore, the redesign aims to optimize impedance matching and reduce losses, ensuring that the device operates efficiently at the desired frequency range.

From this point onward, the procedures, results, and analyses will be conducted concurrently for both Models 1 and 2. Sensors 1 and 2 (model 1 and 2, respectively) were designed to have band pass and band rejection characteristics. By following this approach, we aim to directly compare their performance and identify which model demonstrates superior sensitivity and accuracy in detecting microplastics. At the conclusion, a comparative assessment will be made to understand the strengths and weaknesses of each model. This

analysis will provide insights into any potential limitations, guiding future research to avoid challenges and optimize sensor design.

Figure 3.6 - Proposal model circuits 1 (right) and 2 (left) where the 2 model was made, based on some principals of model.

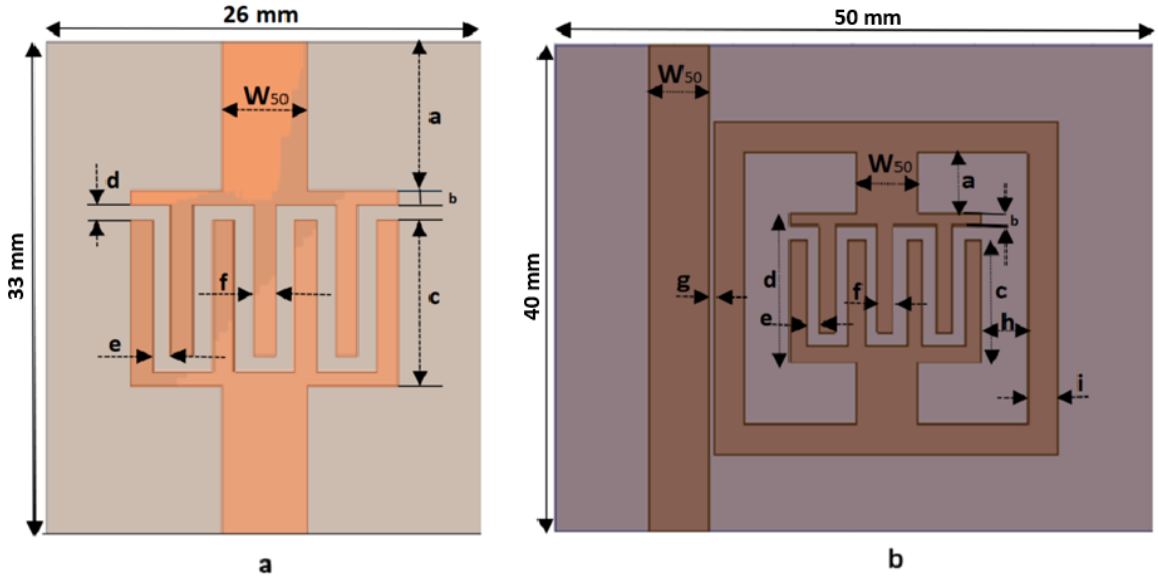

Table 3.3 provides the precise dimensions of the circuits based on the optimization previously described. Notably, the dimensions are configured parametrically, ensuring that any adjustments to one variable automatically update the others. This parametric approach offers adaptability and precision in circuit design, allowing for dynamic responses to modifications, which is particularly advantageous for further optimization and iterative testing.

	Model 1 dimension(mm)	**Model 2 dimension(mm)**
W50	5.1	5.1
A	5	5
B	0.96	0.96
C	10.05	10.05
D	1.30	12.31
E	1.14	1.14
F	1.3	1.3
G		0.3
H		3.83
I		2.55

Table 3.3 - Optimized Dimensional Parameters for Circuit Models 1 and 2.

However, to ensure the accuracy of these measurements, it's essential to distinguish the frequency shifts caused by microplastics from other factors that could influence the results.

This includes elements like the water itself, the container holding the water, and any potential interaction between the silver parts of the resonator and the water, which could cause undesired interference or signal cutoff. Minimizing the effects of these factors is crucial, and this is where the device's calibration plays a vital role.

The calibration process begins by simulating the optimized circuits under different conditions. First, a glass slide with a thickness of h = 0.1(zoom in figure 3.6) mm is introduced as a simple non-reactive material to observe any baseline shifts to avoid contact with the water with the microstrip. Next, a channel made of PDMS (Polydimethylsiloxane) is used to simulate the actual measurement environment. PDMS is commonly used in microfluidic applications due to its flexibility, transparency, and biocompatibility, making it one of the ideals for containing water without significantly affecting the electromagnetic fields. Figure 3.6 illustrates the proposed simulation setup.

By running these calibration simulations, we can isolate and minimize the effects of other variables, ensuring that any frequency shift observed during testing is due to the microplastic presence rather than other materials in the system. This careful calibration process is essential to ensure the reliability and precision of the resonator when used in real-world microplastic detection applications.

Figure 3.6 – Circuit with a Glass Slide Positioned on Top to Prevent Short Circuits.

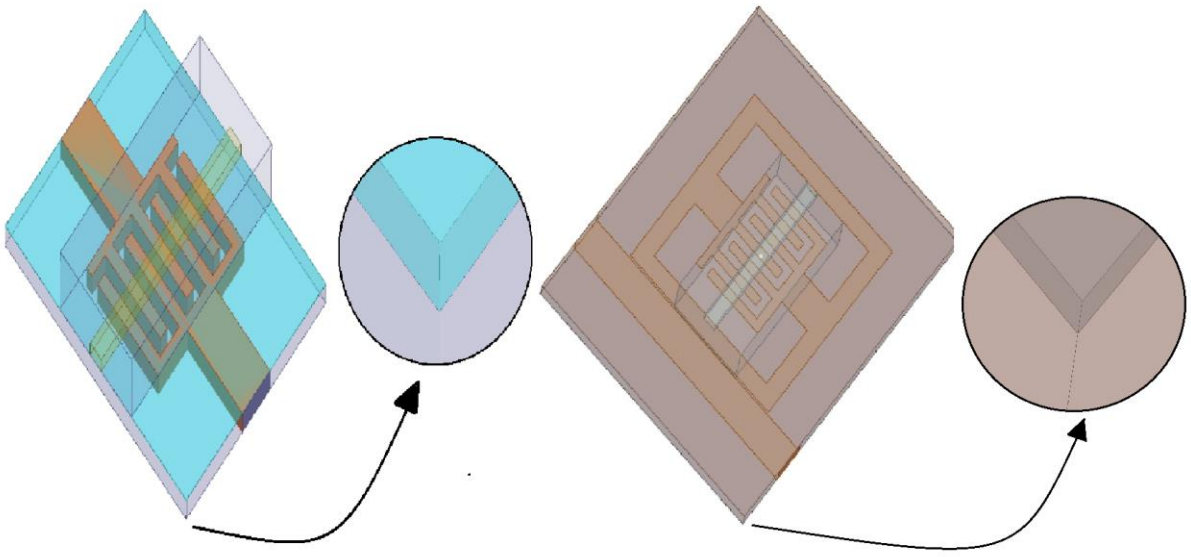

Water is introduced into the channel after simulating the circuit with the PDMS channel. This step helps identify how water alone affects the resonant frequency, considering its high

permittivity compared to air. Finally, a piece of microplastic is placed in the water, and the resonant frequency is monitored for a significant shift, indicating the device's sensitivity to the microplastic particles.

Figure 3.7 - Comparative Resonant Frequency Shifts for PDMS Channel, Glass Slide, and Water-Filled Channel Configurations for model 1.

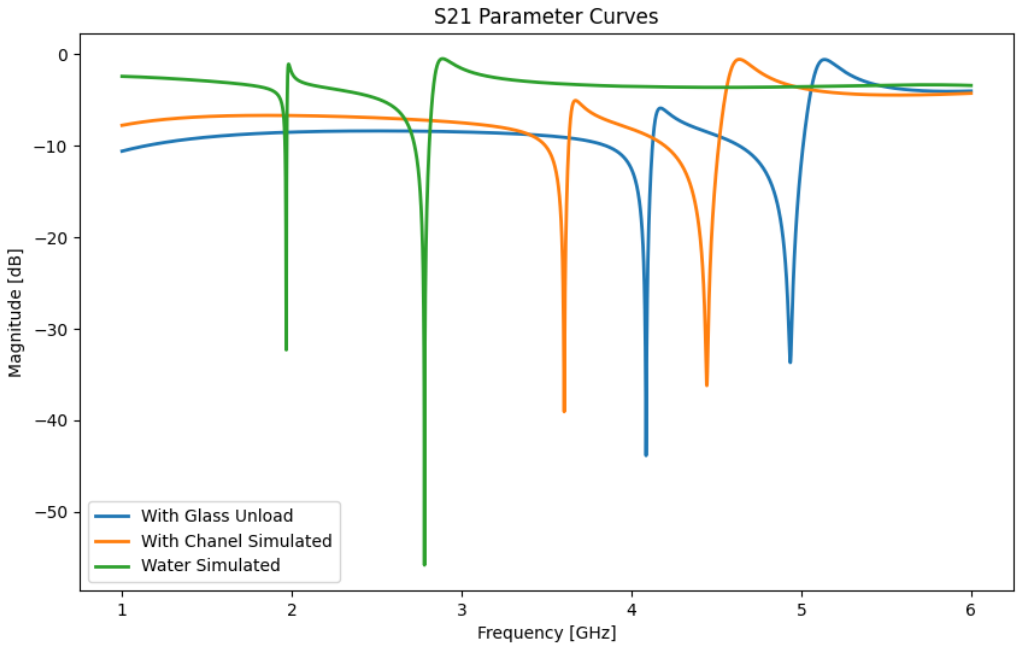

A new set of S-parameters is presented to highlight further the impact of each scenario on the resonator's performance. This graph includes together the S-parameter curves for each condition: (1) the resonator with just the glass slide, (2) the resonator with the channel made of PDMS, and (3) the resonator with water flowing through the channel, as shown in Figure 3.7. By plotting all curves on the same graph, the resonant frequency and magnitude shifts are clearly visible, enabling a direct comparison of how each condition affects the device's response. For model 1, a frequency shift of 475 MHz from 4.078 GHz (with only a glass slide) to 3.603 GHz occurs when a PDMS channel is introduced, indicating the added material's impact. When water is introduced, the resonance further shifts to 2.780 GHz, meaning a shift of 1.30 GHz, and for model 2. a frequency shift of 750 MHz with the presence of the water. This result aligns with literature findings, which consistently demonstrate water's substantial permittivity effect compared to air, validating the observed shifts in resonant behavior. Figure 3.8 shows S11 and S21 of sensors 1 and 2 as a function of the frequency without and with water filling the PDMS channel at the summation.

Figure 3.8 - Simulation Results of Sensor 1 (a) and Sensor 2 (b): Comparison of Frequency Responses for Different MUT Conditions (With and Without Water). The Dashed Curve Represents the Response with Water, While the Solid Line Represents the Response Without Water (air).

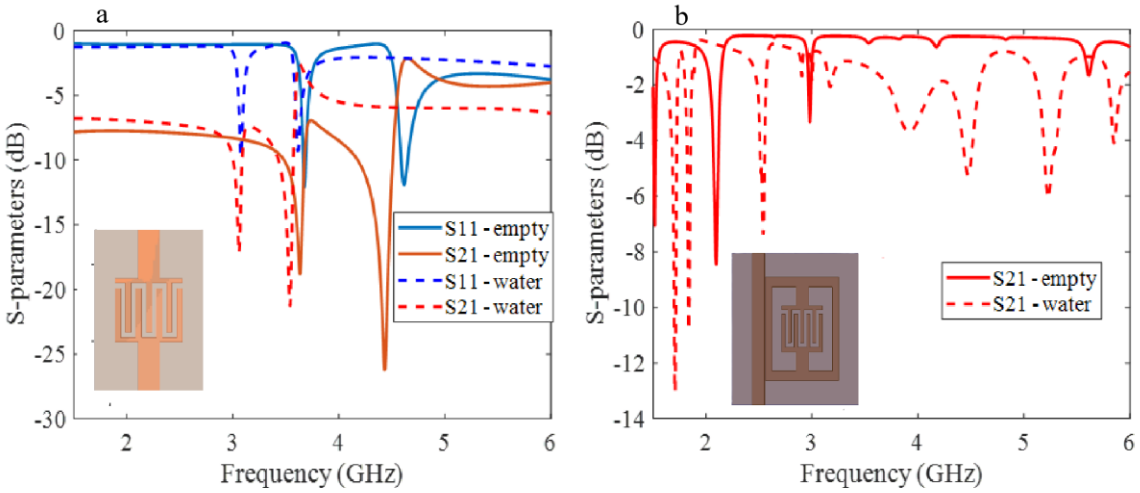

3.6. DETECTING MICROPLASTIC

Moving into the objective, a spherical plastic particle was introduced into the water channel. This spherical shape was chosen strategically to simplify the water's plastic density calculations and assess the effective permittivity. With this approach, we can vary the radius to adjust the plastic density in the water, providing a flexible way to analyze different concentrations. Additionally, this setup allows us to determine the maximum and minimum plastic particle sizes for which the circuits remain operational and sensitive to microplastic detection. This dimension choice provides an adaptable model for assessing the circuit's performance across various conditions and enhancing its practical applications in microplastic sensing.

3.6.1. FIRST GENERATION OF MICROPLASTIC

In this section, both circuit models will be tested using a spherical microplastic particle with a radius of 0.5 mm, as illustrated in Figure 3.9. The results of the S-parameter responses for both Model 1 and Model 2 will be presented and analyzed sequentially. This analysis aims to evaluate how each model reacts to the presence of microplastic in water, focusing on shifts in resonant frequency and changes in magnitude. By comparing the S-parameter responses, we will gain insights into the performance and sensitivity of each model in detecting microplastic

contamination. This systematic approach will allow us to identify which model demonstrates superior detection capabilities and provide a basis for further optimization in future research.

Figure 3.9 - Microplastic sphere added in both sensors.

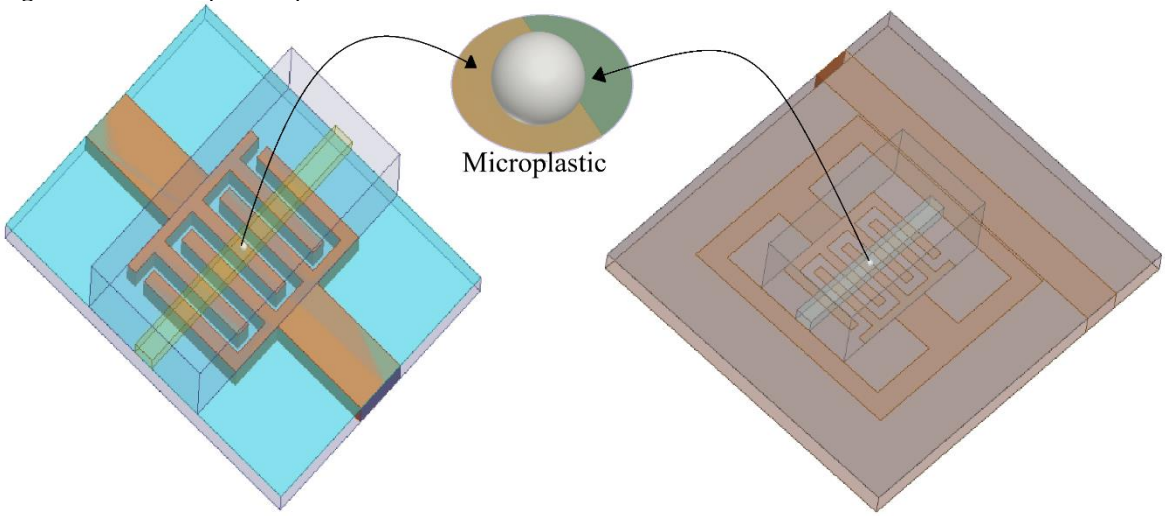

The differences in responses between (S_{21}) in each model underscore how each circuit design—whether band-pass or band-reject—affects the sensitivity and selectivity of the sensor in detecting microplastics. These characteristics make (S_{21}) an ideal parameter for analyzing the circuit's performance across different models, as it directly reflects the impact of varying test conditions on signal transmission or attenuation within each setup.

3.6.1.1. SENSOR 1

For sensor 1, Figure 3.10 (a) shows S11 (blue) and S21 (red) of the sensor with (solid lines) and without (dashed lines) the presence of the 1mm diameter microplastics. As can be seen, the small size of the microplastic compared to the total volume of water only provokes a slight change in transmission or reflection, which can only be seen when zooming at the curves. To determine the frequency with the highest variation of the S-parameters, we plot $\Delta S11$ (blue) and $\Delta S21$ (red) in Figure 3.10 (b). As seen at $f = 3.06$ GHz, both reflection and transmission present the most significant variation (approximately 1 dB), meaning an optimum frequency further to analyze the impact of microplastics in the water. This analysis illustrates the resonator's sensitivity to environmental changes, confirming its potential for detecting microplastic contamination through measurable frequency shifts, and transmission changes in each test setup.

Figure 3.10 – (a) S-Parameters as a function of the Frequency in the presence and absence of microplastic inside the fluidic channel. (b) shows the variance of S11 and S21 in the presence and absence of microplastic.

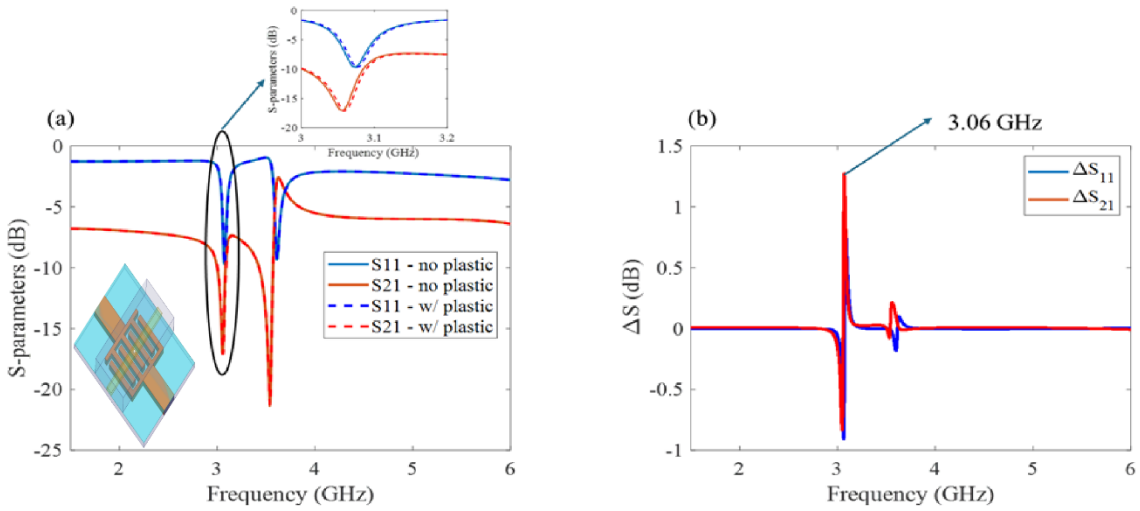

Given this project's 1 to 6 GHz operating range, 1 dB is significant, especially for material identification tasks such as microplastic detection in water. This shift provides a quantifiable indicator of the device's response to environmental variations (e.g., from water alone to water with microplastics), demonstrating its utility in identifying contaminants like microplastics in various media.

As explained in the literature, an RF circuit with two ports, port 1 (input) and port 2 (output), receives an input current (J), which flows from port 1 to port 2. As these current travels through the circuit, an electric field (E) is established across the interdigital capacitor gap, bridging the signal path from one side to the other[114][115]. When introduced, microplastic particles become immersed in this electric field, altering the dielectric properties in the field region. This change directly impacts the transmission (S_{21}) and reflection (S_{11}) parameters of the system. In this sense, the is an optimal physical position which provokes the highest change in S_{21} and S_{11}.

In Figure 3.11 (a), the normalized electric field distribution is visualized on a rectangular plane perpendicular to the RF device's surface, illustrating how the field extends through the dielectric material. Figure 3.11 (b) shows the flow of current (J) across the circuit from port 1 to port 2. Both images are taken at a frequency of 3.06 GHz, highlighting the frequency shift when comparing the response with pure water as the material under test (MUT) versus water containing microplastic contaminants. In this figure, it is possible to notice the position where the electric field is more intense, which implies more energy being stored in those regions. In this sense, when the microplastic is at these positions (referred here as hot spots), there will be

a larger variation of S_{21} and S_{11}. As can be seen in Figure 3.11, the position is at 6 cm from the center of the interdigital sensor.

Figure 3.11 - Electric Field Distribution and Current Flow in the RF Circuit at 3.06 GHz, Illustrating the Influence of Microplastic Contaminants in the Material Under Test (MUT).

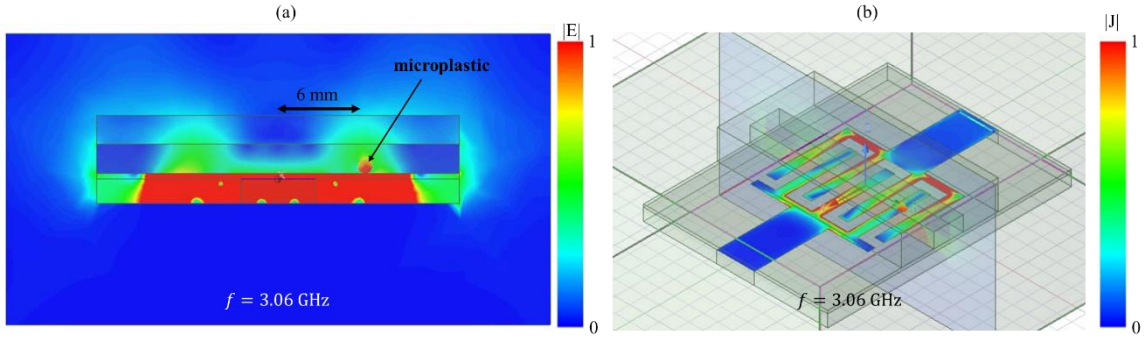

To confirm the hot-spot, Figure 3.12 show S_{21} and $S_{11}$for the plastic moving within the interdigital sensor, for different microplastic radius (from 0.2 to 0.5 mm). We observe a similarity between the curve and the electric field distribution of the previous figure, which can be explained by the symmetry inherent in the RF circuit. In symmetric RF circuits, the design allows for a balanced distribution of electric fields across the structure, with the circuit centerline acting as a mirror axis. This symmetry helps ensure that any changes in the material under test (MUT), such as the addition of microplastics, impact the electric field distribution uniformly across both sides of the circuit.

Figure 3.12 illustrates the RF circuit's response as a function of the position and size of the plastic particle, shown through the magnitude of (S_{21}) and (S_{11}). As expected, larger spheres will have more impact on the sensors response resulting in a higher variation of the S-parameters. One important issue observed in Figure 3.12 is the reduction of the initially observed 1 dB difference. This occurs since at the first simulation, the software was set for a “fast” sweep, which is less precise, while for the simulation shown in Figure 3.12, the circuit is discretely solved at the chosen frequency. Although it reduced the variation, it is still possible to confer the presence of microplastic in the system. The response is small for a radius smaller than 0.2 mm, and it would be difficult to assess these values experimentally. This sensitivity to particle size emphasizes the potential of the RF sensor to detect varying levels of microplastic contamination by monitoring the corresponding changes in resonant frequency and magnitude. Using this sensor, the position of the microplastic would be more accurately predicted using S11 parameters since it implies a higher change.

Figure 3.12 - Polynomial fitted - Symmetric Response of Electric Field and S-Parameters (S_{11}) and (S_{21}) in RF Circuit for Varying Plastic Particle Radius in Water.

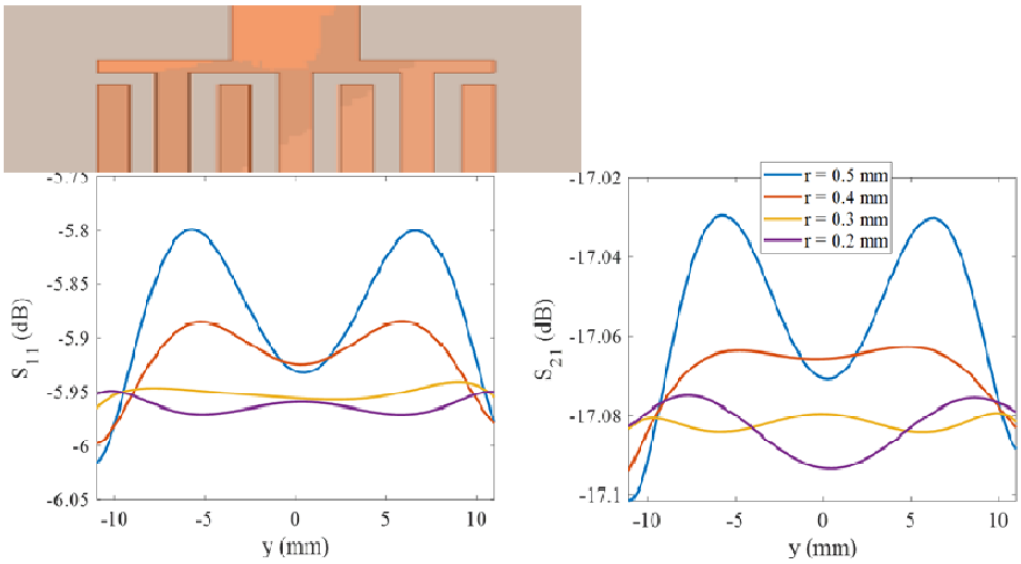

3.6.1.2. SENSOR 2

For circuit model 2, a band-reject circuit, the same testing process was applied as in model 1, and the results are displayed in Figure 3.13, for the microplastic positioned in two different positions (at the gap between the microstrip and the sensor, and at 6cm from the interdigital sensor). This analysis was conducted with the plastic particles configured and dimensioned similarly. As previously mentioned, the analysis focuses solely on (S_{21}) due to the nature of the circuit's response.

Model 2 was evaluated under three conditions to enhance the test dynamics: with only water, with plastic particles positioned at two different points, and using a range of frequencies of 1 to 6 GHz. This model exhibits three notable resonant frequencies, and the analysis centers on these points. In Figure 3.13 (a), the full response from 1 to 6 GHz is shown, while (b) and (c) provide detailed views of the shifts at two specific frequencies: 1.72 GHz and 1.84 GHz, respectively, where water without plastic initially resonates.

At 1.84 GHz, the presence of plastic causes distinct shifts: plastic at position 1 shifts to 1.81 GHz, and plastic at position 2 shifts to 1.82 GHz, aligning closely with the behavior observed in model 1. Although the shift magnitude is modest, these results demonstrate the circuit's accuracy and sensitivity to minor environmental changes, reinforcing its effectiveness in detecting the presence of microplastics.

Figure 3.13 - (a) Frequency Response of Circuit Model 2 with Water and Microplastic Contaminants at 2 Positions. (b) and (c) provide detailed views of the shifts at two specific frequencies: 1.72 GHz and 1.84 GHz, respectively.

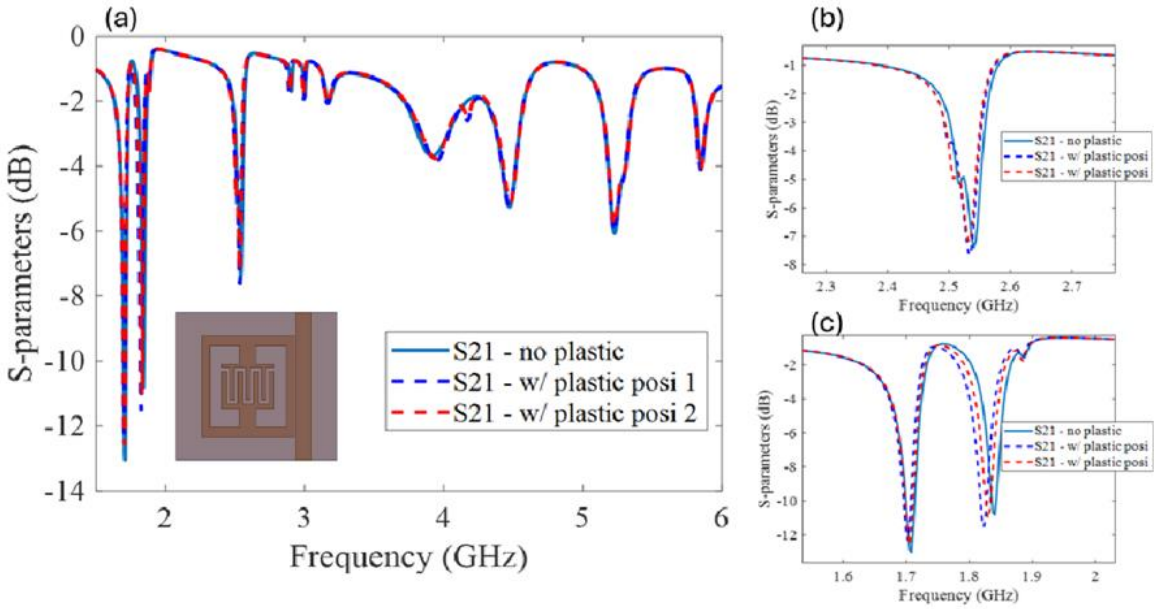

Similar to Model 1, Figure 3.14 presents the computed differences in response for the (S)-parameters. In Figure 3.14(a), the response across the full frequency range (1 to 6 GHz) is shown, where the most significant difference occurs at 1.82 GHz, followed by another notable difference at 2.84 GHz. Figure 3.14 (b) and (c) provide a zoomed-in view of these regions for enhanced clarity. These findings confirm that both circuit models are sensitive and functional for detecting microplastics. Importantly, the observed frequency shifts are linked to the size of the spherical microplastic particles: larger microplastic particles produce more noticeable shifts, demonstrating that the circuits are more responsive with increased MUT (material under test) size. As can be seen, the circuit presents the highest variation at the resonant frequencies at 1.82 Ghz and 2.54 GHz, with a change of up to 6dB at the first resonance. In this sense, it is possible to detect microplastic presence by resorting to these frequencies. Note that the sensibility of Sensor 2 is much higher than Sensor 2, as noted by the higher variation.

Figure 3.14 - Differences in S-Parameter Responses Across Full and Selected Frequency Ranges for Microplastic Detection in model 2.

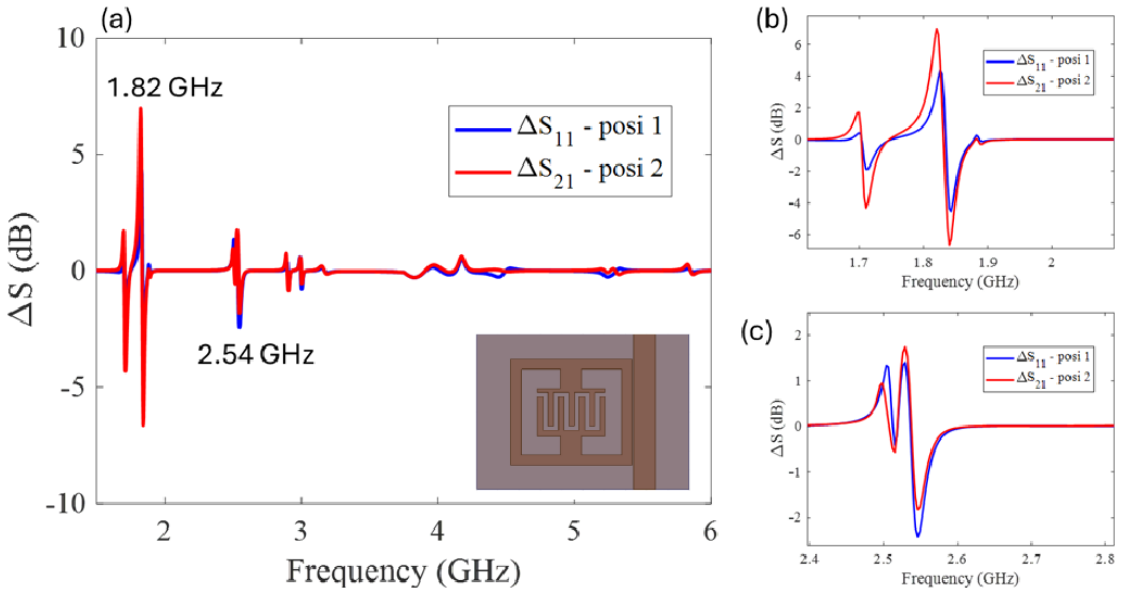

Figure 3.15 presents the electric field distribution of circuit model 2, highlighting the positions of the hot spots at a frequency of 1.82 GHz (the electric field at 2.54 GHz provides almost the same electric field pattern). These hot spots are clearly concentrated along the pathway where the plastic pollutant traverses the circuit, confirming two important aspects. First, it demonstrates the symmetry of the circuit, with hot spots mirrored on both sides of the central axis, indicating balanced field distribution, which is crucial for consistent and reliable sensor responses. Additionally, the positioning of these hot spots exactly where the plastic crosses the circuit reveals how the presence of the pollutant directly interacts with the electric field. This interaction indicates the circuit's sensitivity to microplastic contaminants, as the pollutant’s effect on the electric field is most pronounced in these high-intensity regions. Furthermore, the clear field concentration suggests that the circuit is optimized for detection along this pathway, as any changes in permittivity (from added pollutants) are immediately reflected in the S-parameter response, enhancing the circuit’s capability to detect and respond to even subtle variations in the environmental medium.

Figure 3.15 - Electric Field Distribution and Hot Spot Localization in Circuit Model 2 at 1.82 GHz

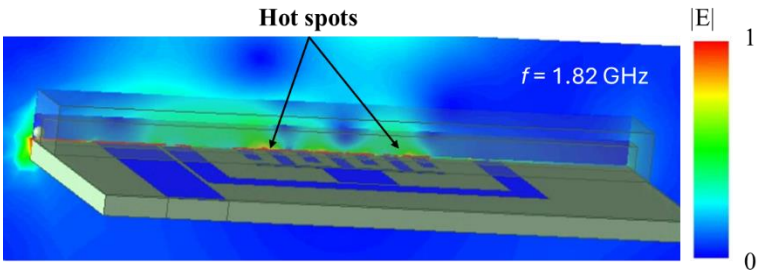

Following the electric field distribution shown in Figure 3.15, Figure 3.16 illustrates the circuit's response to microplastic particles crossing from one side to the other. This procedure was repeated four times, each with a different microplastic concentration achieved by varying the radius of the spherical plastic particles (MUT). The figures clearly demonstrate the circuit's symmetrical design, as the high-magnitude field regions align consistently with the previously identified hot spots. Additionally, the figures show the device's enhanced sensitivity as the concentration of plastic pollutants increases within the medium. As can be seen, the transmission shift is close to 1 and 0.4 dB for 1.82 GHz and 2.54 GHz, respectively, when r = 0.5 mm. This indicates a very high sensor sensibility at 1.82 GHz, providing a good alternative for microplastics detection. As can be seen, as the size decreases, the changes reduce, and the detection of microplastic is also decreased. Based on the noise, we can notice that Sensor 2 can detect microplastics down to r = 0.2 mm of radius.

Figure 3.16- Symmetrical Circuit Response to Varying Microplastic Concentrations at Key Resonance Frequencies (1.82 GHz and 2.54 GHz).

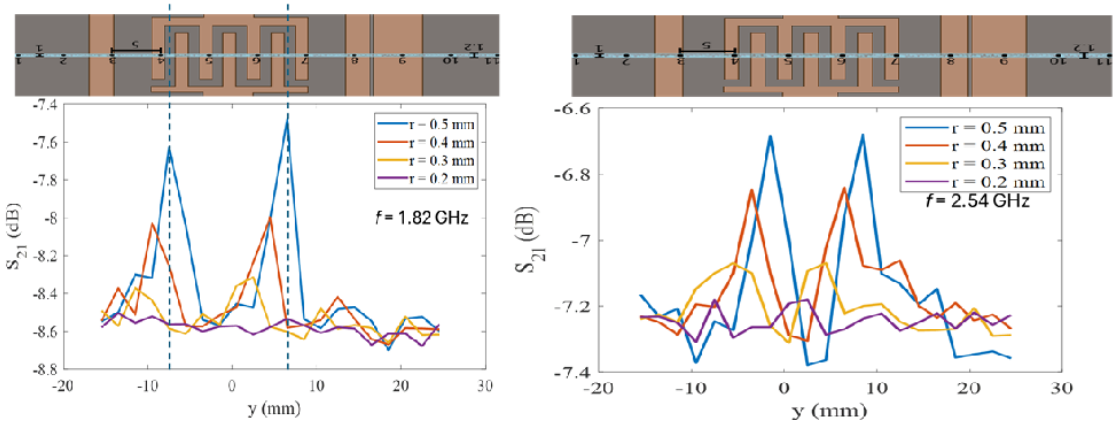

This test was key to assessing the sensor's sensitivity to both the presence and movement of microplastics within its active region. The results, illustrated in the final figure, show distinct shifts in the magnitude of the S-parameters at each microplastic position, confirming a variation in response based on the particle's location within the resonator's structure. These findings highlight the resonator's capability to detect microplastics and track their movement across its sensing surface. This spatial sensitivity is essential for precise monitoring applications, showcasing the resonator's potential for high-accuracy detection of microplastic contamination in water. It is also important to notice that the curves shown in Figure 3.12 and Figure 3.16 illustrate what a real-time oscilloscope could measure for a passing microplastic at the system, highlighting that it produces a signature that can be used for inferring its dimensions.

In summary, for the 1.82 GHz resonance frequency:

A particle radius of 0.2 mm results in a magnitude response of -8.52 dB. With a radius of 0.3 mm, the response is -8.28 dB. At 0.4 mm, the response increases to -7.93 dB. At the largest tested radius of 0.5 mm, the response reaches -7.47 dB.

At the 2.54 GHz resonance frequency:

- The magnitude response for a 0.2 mm radius is -7.18 dB; with a 0.3 mm radius, the response is -7.05 dB; for a 0.4 mm radius, the response shifts to -6.85 dB; at a 0.5 mm radius, the response peaks at -6.68 dB.

This consistent decrease in magnitude (absolute values) at both resonance frequencies as the particle size increases indicates that the sensor becomes more responsive to the plastic particles' presence as they occupy more volume within the circuit's field. This pattern is highly significant, as it supports the device’s ability to detect variations in microplastic concentrations.

3.6.2. SECOND GENERATION OF MICROPLASTIC

With both circuit models confirmed as operational for detecting microplastics, the next step involves analyzing a second generation of plastic particles, specifically by examining the concentration of microplastics within the water sample (which is a much smaller dimension but diluted in water). For this, we use Maxwell Garnett's theory, which predicts that as the volume of plastic in water increases, the effective permittivity of the mixture decreases. This relationship is due to the relative permittivity of water and plastic: water has a significantly higher permittivity than plastics, which are generally more electrically insulating. As the volume fraction of plastic particles grows, these lower-permittivity inclusions alter the overall dielectric properties of the medium, effectively reducing the permittivity of the mixture. This experiment seeks to validate how varying microplastic concentrations influence the sensor’s response, providing further insight into the circuit's sensitivity and effectiveness in detecting microplastic contamination at different levels.

3.6.2.1. SENSOR 1

In sensor model 1, the Maxwell-Garnett theory was applied by adjusting the permittivity (ε) of water from 81 to 70, simulating the effect of increased microplastic concentration on the

water's effective permittivity, which would correspond to a change in the concentration of microplastic in the water samples. It is important to notice that, although it may correspond to a high density of microplastic, there is always the possibility of concentrating the water, which is a common technique for analyzing water samples. In this procedure, you need to evaporate a large quantity of water and stay with a more concentrated remaining. For each adjusted value of ε, the S-parameters were observed to track how changes in the dielectric environment influenced the sensor response.

The results in Figure 3.17 (a) show the behavior of the S-parameter at the first resonance frequency, while Figure 3.17 (b) illustrates the response at the second resonance. In both figures, arrows indicate the trend of the S-parameter shifting as ε decreases, pointing to the direction of resonance frequency changes as plastic concentration increases. This trend aligns with Maxwell-Garnett predictions, confirming the sensor's sensitivity to variations in effective permittivity caused by microplastics in the water.

Figure 3.17- Sensor 1 S-Parameter Responses for Sensor Model 1 with Varying Water Permittivity (ε), Illustrating Resonance Shifts at First and Second Frequencies.

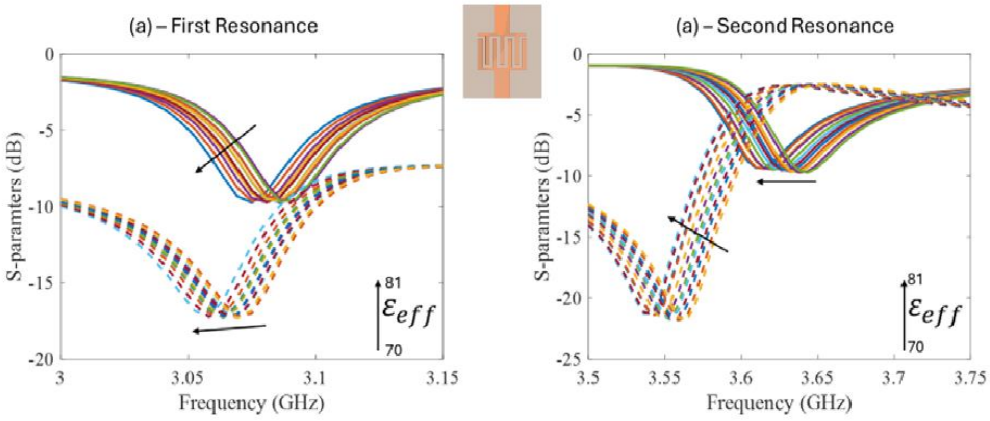

Figure 3.18 illustrates the differences in reflection S11 and transmission S21 lines, highlighting the shift from an initial water permittivity of 70 to a final permittivity of 81. This shift validates the Maxwell-Garnett theory, which posits that as the concentration of plastic particles increases, less volume is available for water, given the principle of volume conservation. Consequently, the effective permittivity of the water-plastic mixture decreases in proportion to the density of the plastic pollutant, confirming an inverse relationship between effective permittivity and pollutant density.

By comparing Figure 3.17 and Figure 3.18, it becomes clear that higher plastic concentration significantly influences the (ΔS)-parameter magnitudes. In contrast, Figure 3.18 shows a substantial increase in the response, where the initial resonant frequency at 3.06

GHz shifts to 3.08 GHz, and a secondary frequency shift at 3.57 GHz reaches a much larger magnitude, increasing to 10.8 dB. This notable enhancement in the (ΔS)-parameter emphasizes the sensor's increased sensitivity to higher plastic concentrations, with the altered signal strength and frequency shift providing insight into pollutant density.

Figure 3.18 - Shift in (S_{11}) and (S_{21}) S-parameters with Increasing Plastic Concentration, Illustrating Resonance and Magnitude Changes in Response to Permittivity Variations

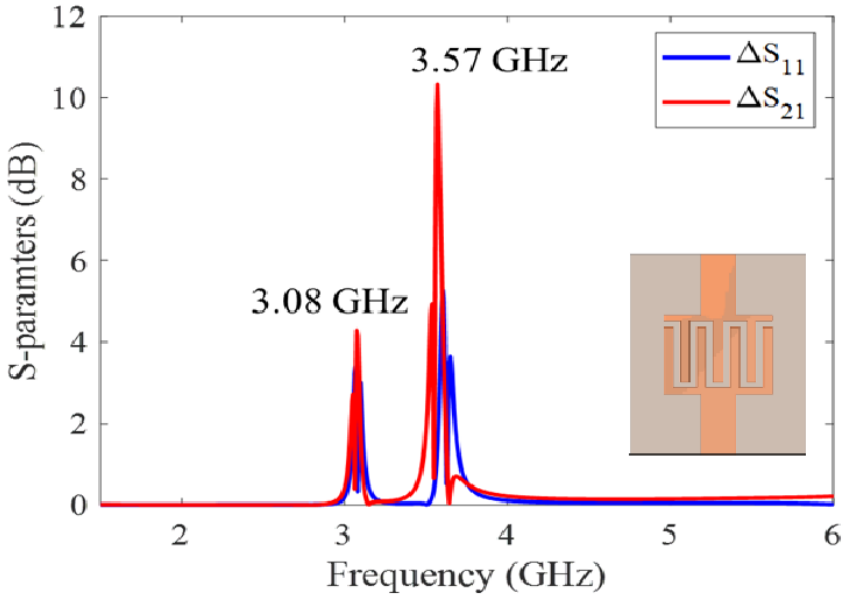

In Figure 3.19, the left graph displays the two resonant frequencies observed in (S_{11}). As noted previously, the changes in (S_{11}) due to effective permittivity alterations are relatively modest, with minimal frequency shift across the permittivity range of 70 to 81. On the right, the two resonant frequencies in (S_{21}) reveal more significant shifts, particularly at the higher frequency resonance at 3.57 GHz. Initially, the first resonance at 3.08 GHz demonstrates a lower sensitivity to the increase in effective permittivity, but as the permittivity approaches 81, the response becomes more dynamic. This shift highlights the sensor's ability to respond to pollutant density changes as predicted by the Maxwell-Garnett theory, where the effective permittivity decreases with increasing plastic density, significantly influencing the (S_{21})-parameter responses.

Figure 3.19 - Variation of (S)-Parameter Resonant Frequencies in Response to Effective Permittivity Changes Due to Increased Plastic Pollutant Density

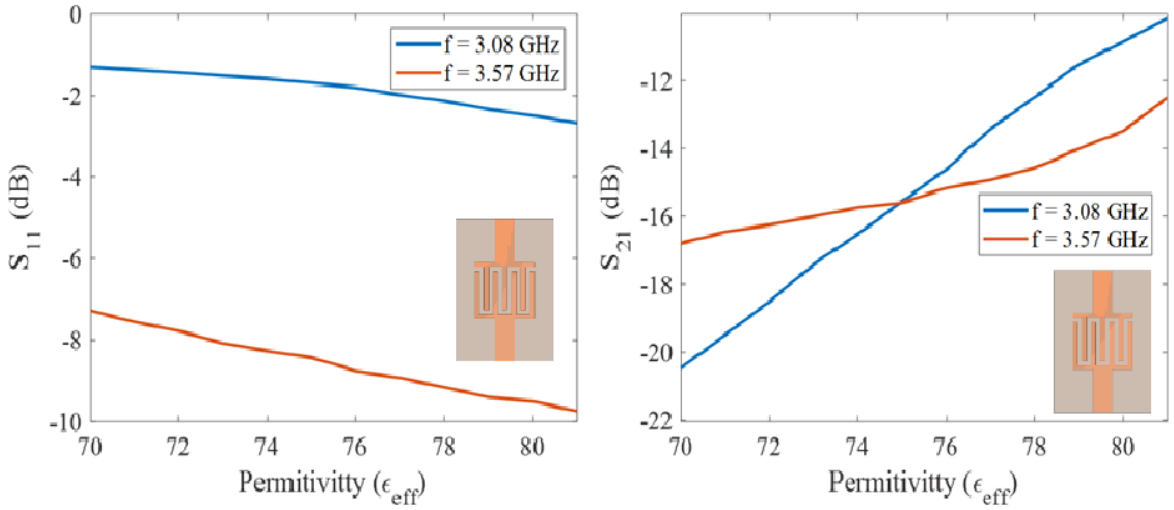

As discussed in Chapter 2, effective permittivity is influenced by frequency, an effect supported by the theoretical equations for frequency-dependent permittivity. Figure 3.20 provides a simulation-based confirmation of this dependency, illustrating how frequency shifts occur as effective permittivity changes, validating the model's sensitivity to variations in permittivity.

Figure 3.20 - Simulated Resonance Frequency Shifts as a Function of Effective Permittivity Variation from 70 to 81.

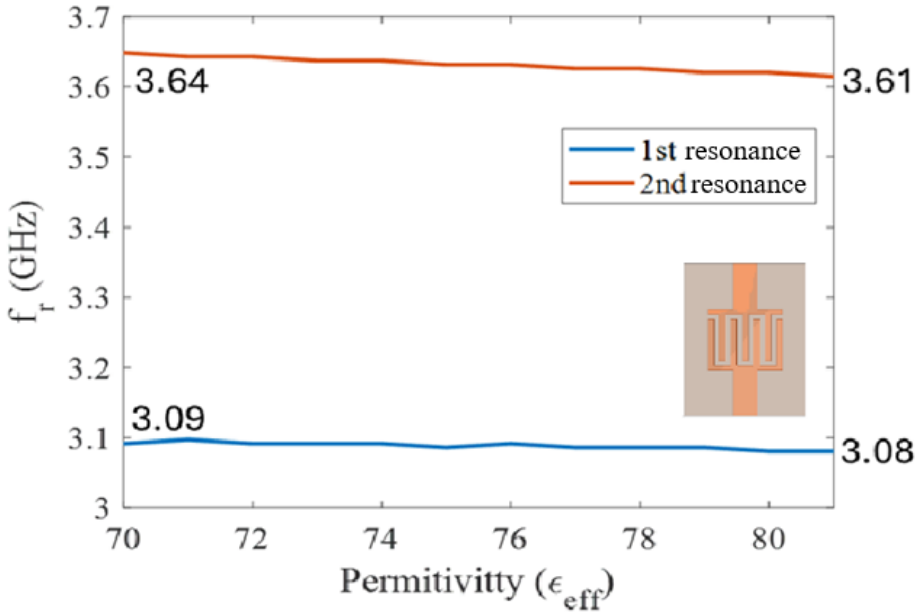

In this simulation, the effective permittivity values are incrementally adjusted from 70 to 81, which reveals shifts in the resonance frequencies. Specifically, the first resonance

frequency shifts from 3.08 GHz to 3.09 GHz, while the second resonance frequency experiences a more pronounced shift from 3.61 GHz to 3.64 GHz. These shifts, though small in magnitude, indicate a consistent, proportional relationship between effective permittivity and resonance frequency in the RF circuit. The more significant change observed at the second frequency resonance (3.61 GHz to 3.64 GHz) highlights the circuit's increased sensitivity at higher frequencies, where minor changes in permittivity result in relatively larger shifts in resonance frequency. This simulation further confirms that the RF circuit design is effectively responsive to micro-level changes in environmental permittivity, demonstrating the model's practical accuracy in detecting permittivity variations, as predicted by theoretical frameworks.

3.6.2.2. SENSOR 2

For sensor model 2, an identical series of simulations were conducted to examine the impact of effective permittivity changes from 70 to 81 on its resonance frequencies. Figure 3.21 illustrates these effects, with the left side of the figure focusing on the two closely spaced resonance frequencies. Arrows in this section indicate the shifting direction of these resonances as permittivity increases from 70 to 81. This demonstrates a slight upward frequency shift, as expected from the Maxwell-Garnett theory, which predicts that effective permittivity decreases as the density of plastic in the water mixture rises.

Figure 3.21 - Shifts in Resonance Frequencies for Sensor Model 2 as Effective Permittivity Changes from 70 to 81, Highlighting Direction of Shifts at Close and Distant Resonances

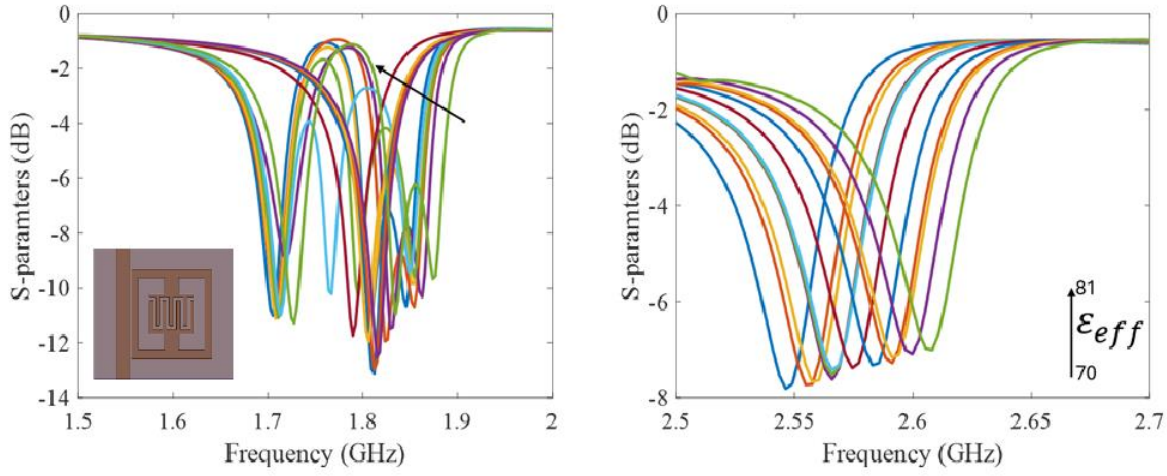

On the right side of Figure 3.21, the focus is on the second resonance frequency. This frequency also shifts as permittivity changes, but at a more pronounced and linear level, which is consistent with the observed behavior in other simulations. The response aligns with the

Maxwell Garnett model, where an increased density of plastic particles effectively reduces the permittivity of the mixture due to the substitution of water volume by plastic. As a result, the sensor's resonance frequency shifts upward as plastic density rises, showing a consistent trend across multiple resonances.

This consistent response to permittivity changes highlights sensor model 2's suitability for detecting plastic pollutant concentration, even at varying permittivity values. The results further validate the RF circuit's capacity to measure microplastic contamination across different resonance frequencies. Figure 3.22 illustrates the S-parameter response differences for the Material Under Test (MUT) when configured with only water versus water mixed with a plastic pollutant, with the pollutant mixture's effective permittivity incrementally adjusted from 70 to 81. This adjustment simulates an increase in the density of plastic particles within the water, providing insight into the sensor's sensitivity to pollutant concentration levels. As expected, this shift in permittivity follows the behavior predicted by the Maxwell Garnett equation, which states that the effective permittivity of a composite medium will decrease as the volume fraction of plastic particles increases, thereby substituting for water's higher permittivity. The results clearly demonstrate significant changes at two main resonance frequencies, at 1.82 GHz and 2.54 GHz, aligning with observations from Figure 3.14 (b) and (c).

Figure 3.22 - S-Parameter Response Comparison for Water and Water with Plastic Pollutant, Highlighting Resonance Shifts at 1.82 GHz and 2.54 GHz with Effective Permittivity Increase from 70 to 81

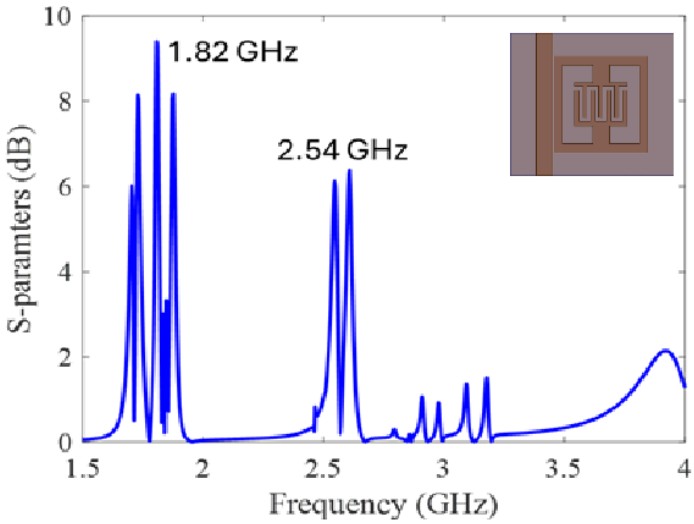

At both resonance frequencies, the magnitude response nearly doubles with the increased density of plastic pollutants, showcasing the sensor's ability to detect pollutant concentration variations. This effect is particularly prominent at 2.54 GHz, where the shift is most

pronounced. These findings validate the use of this RF sensor for effective monitoring of microplastic contamination, as the S-parameter response directly correlates with changes in pollutant density in the water.

Finally, by repeating the simulation to analyze the relationship between effective permittivity and (S_{21}) (dB), as well as the relationship between effective permittivity and frequency, we gain further insights into the sensor's responsiveness across different positions across the channel. In the initial detection tests, the first two resonance frequencies demonstrated relatively lower sensitivity with the presence of a unique microplastic, while the second resonance frequency at 2.54 GHz exhibited a more dynamic response. This trend persists in the current simulation, where the changes in (S_{21}) magnitude, and frequency shift are most pronounced at the 2.54 GHz resonance.

In the permittivity vs. (S_{21}) plot, the resonance frequencies around 1.82 GHz display a fluctuating response, with the amplitude oscillating but remaining within a narrow range. In contrast, the 2.54 GHz frequency shows a more gradual and distinct trend, with (S_{21}) shifting steadily from approximately -1.4 dB to -6.4 dB as the effective permittivity is increased from 70 to 81. This change illustrates the increased sensitivity at this higher frequency, aligning well with the Maxwell Garnett predictions regarding effective permittivity and pollutant density.

On the right side of Figure 3.23, the permittivity vs. frequency analysis further emphasizes this effect. At 1.82 GHz, the resonance shift is minimal and non-linear, showing weak response changes as permittivity is adjusted. However, at 2.54 GHz, a more linear frequency shift is observed, with the resonance frequency gradually decreasing from 2.61 GHz to 2.54 GHz as effective permittivity rises. This linearity and magnitude shift at 2.54 GHz suggest that this resonance is highly responsive to changes in plastic pollutant concentration, reinforcing the suitability of this frequency for precise detection and monitoring of microplastic contamination levels in the sensor's active range.

The next chapter will delve into a detailed exploration of real experimental tests. This transition from simulation to physical realization will provide further insights into the effectiveness of the design modifications and their implications for practical deployment. In conclusion, the simulation of the two models of RF resonators demonstrated the importance of meticulous mesh calibration and the consideration of potential sources of error. By focusing on enhancing mesh resolution and performing thorough mesh convergency, the results indicated a clear path toward achieving high-quality performance metrics, such as resonance frequency

and Q-factor. These findings underscore the critical nature of accurate simulations in predicting the behavior of RF resonators in practical applications.

Figure 3.23 - Analysis of Effective Permittivity vs. (S_{21}) Magnitude and Frequency Shifts, Highlighting Increased Sensitivity at 2.54 GHz Resonance with Permittivity Change from 70 to 81

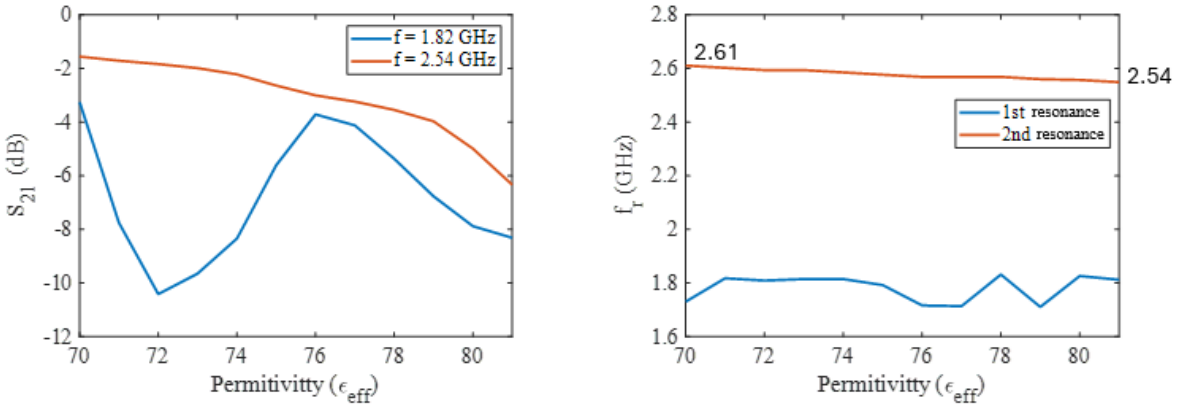

CHAPTER 4

4. EXPERIMENTAL RESULTS

This chapter presents the experimental procedures undertaken to develop and analyze the proposed circuit models. Building on the theoretical foundation and simulations discussed previously, we detail the fabrication process, from selecting materials to assembling circuit components, ensuring alignment with the designed specifications. Each fabrication step is carefully documented to provide a clear view of the construction methodology and the considerations necessary for achieving optimal performance.

The setup and calibration of the measurement system are then described in detail, covering the instrumentation, environmental conditions, and testing protocols used to capture accurate data. This phase is crucial, as it establishes a reliable basis for measuring and evaluating the circuit characteristics under different operating conditions. Attention is given to key factors, such as impedance matching, measurement accuracy, and minimization of external interferences, which are essential for obtaining high-quality results.

Finally, the experimental results are presented, analyzed, and compared to the initial design goals and simulation predictions. Discussions will focus on interpreting these results, identifying discrepancies, and assessing the effectiveness of the circuit modifications. This comprehensive analysis provides insights into the device's performance, highlighting achievements and areas for potential improvement. This chapter ultimately aims to validate the circuit designs and provide an understanding of their practical capabilities and limitations in real-world applications.

4.1. EXPERIMENTAL SETUP

With the circuit now fully fabricated, the next critical step is to set up the bench test as shown in figure 4.1, to verify its functionality and assess how closely its performance aligns with simulation predictions. It is common for differences to arise during bench testing due to

the complexities and imperfections inherent in real-world conditions. These variations can be attributed to several factors, including human error, environmental impurities, mechanical discrepancies, and interference from other electronic equipment in the lab.

Figure 4.1 - Experimental Setup for Microplastic Detection Tests: Overview and Sensor Configuration. This figure illustrates the complete experimental setup and details each component involved in the microplastic detection process: a) Full bench setup, including the Vector Network Analyzer (VNA), a syringe pump to control fluid flow, the sensor with the Material Under Test (MUT), and a waste container for expelled fluid. b) Top view of the sensor showing the electrical connections and tubing for water and microplastic injections. c) Side view of the sensor with hose connections, providing an alternate angle for the fluid pathways. d) Tire particle sample used for testing, sized for precise compatibility with the PDMS channel. e) Close-up of the microplastic particle situated within the detection channel during the test.

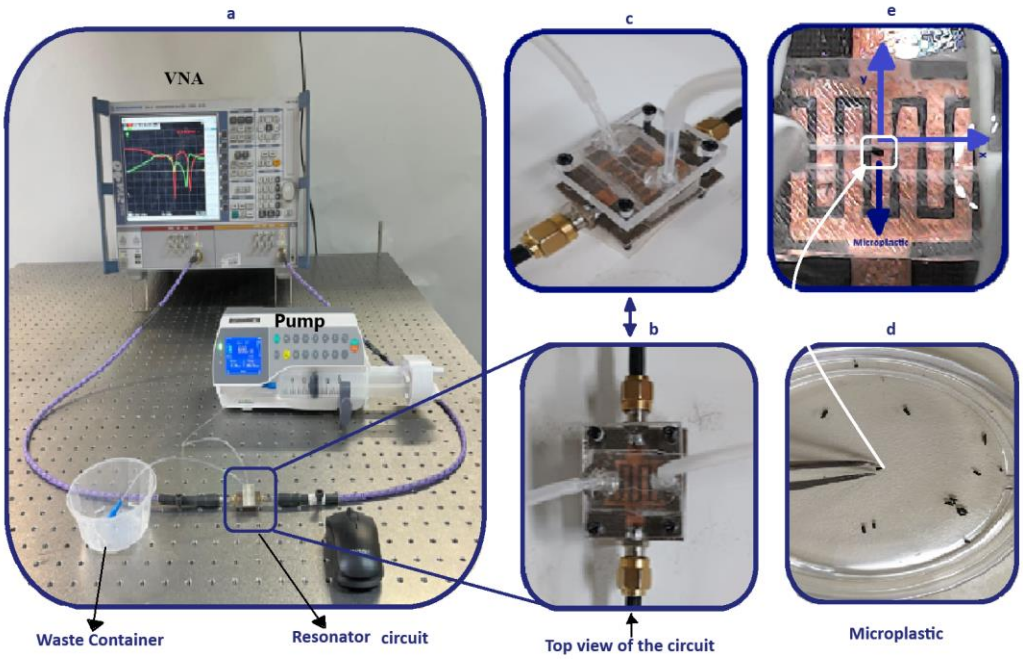

4.1.1. POTENTIAL SOURCES OF VARIATION

- Human Error, Minor inaccuracies during circuit placement, handling, and testing can contribute to discrepancies between expected and actual results. Careful attention during each step is essential to minimize these potential issues.
- Impurities and Environmental Conditions Dust, moisture, or other contaminants in the workspace can subtly impact circuit behavior. Proper cleaning and maintaining a controlled testing environment can help reduce these effects.
- SMA Connector and Adapter Gaps Even slight misalignments or gaps between the SMA connectors, adapters, and the circuit can introduce signal transmission and reception variations, leading to measurement inconsistencies.

- PCB Material Variations Variability in the substrate material, such as inconsistencies in the dielectric properties of the PCB, could affect the circuit's performance.
- Water Quality For circuits designed to detect materials in water, using non-fully distilled or contaminated water could skew results due to unexpected impurities or conductivity.

4.1.2. TEST SETUP CONSIDERATIONS

The calibration of the test equipment is paramount. Using instruments and confirming their calibration status before beginning tests helps ensure the measurements' accuracy. Additionally, the test should be conducted in a location where electromagnetic interference is minimized, or appropriate shielding should be applied.

4.2. FIRST GENERATION OF MICROPLASTIC

The primary objective of the first-generation testing phase is to confirm that the resonator circuit can reliably detect the presence of plastic particles in water. This foundational test evaluates whether the device is functioning as intended regarding sensitivity and response consistency. To maintain control and reliability, the tests focus on a single type of plastic particle, as shown in Figure 4.1 (d).

4.2.1. CHOICE OF TEST MATERIAL

At this stage, rubber particles from a tire cutter, measuring approximately $0.3 \times 0.3 \times 0.3$ mm^3, were chosen as the plastic sample due to their prevalence in environmental pollution. These particles are ideal for several reasons:

Environmental Relevance: Tire particles are one of the most prevalent types of microplastic pollution due to wear and tears from road traffic, making them a suitable model for environmental monitoring applications.

Size and Shape: The small, cylindrical form factor enables precise handling, particularly for dispersal in water samples and controlled injection into the circuit testing apparatus. Their dimensions were carefully chosen to ensure they could easily pass through a syringe needle, allowing for repeatable and consistent dosing in each test. The choice of ground tire particles

simulates real-world pollution and ensures that the resonator's response is tested under realistic conditions.

For the measurements, the following procedures were adopted:

- *Equipment Preparation and Calibration:* VNA Calibration - The Vector Network Analyzer (VNA) was thoroughly calibrated before connecting the resonator. The calibration was conducted within the 1 to 6 GHz frequency range, capturing the study's resonance frequency shifts.
- *Sweep Parameters:* To maximize resolution and capture minute changes, a sweep of 801 points was selected. This point density ensures sufficient data points across the frequency range, allowing for accurate tracking of resonance frequency shifts and magnitude changes.
- *Connection Integrity:* High-frequency testing is sensitive to any cable and connector quality inconsistencies. Each cable, SMA connector, and adapter were checked for proper attachment to avoid signal losses or reflections that could distort the measurements. The connections were verified before each test to ensure that they were secure, and any loose or damaged cables were replaced.
- *Sample Preparation:* A solution is prepared with a specified concentration of ground tire particles dispersed in distilled water. Consistent stirring ensures even distribution, preventing particle aggregation that could impact the readings.
- *Baseline Measurement:* The circuit's response is measured in pure distilled water before introducing the plastic particles. This baseline measurement establishes a control for comparing any frequency shifts caused by the presence of microplastics.
- *Controlled Plastic Injection:* A syringe is used to introduce a known volume of the prepared microplastic solution into the test setup, ensuring precise dosing and accurately controlling the particle concentration.
- *Resonance Frequency Monitoring:* After injecting the microplastic solution, the resonator's frequency response is monitored in real-time. The addition of plastic particles with distinct dielectric properties alters the circuit's electromagnetic environment, resulting in a shift in the resonance frequency and a change in the Q-factor.
- The S-Parameters data are recorded for analysis, allowing for a quantitative assessment of the detection capability. Any shifts in these parameters indicate that the resonator is successfully detecting the presence of microplastics.

- *Repeatability and Consistency Checks:* Multiple trials are conducted to ensure the reliability of the detection mechanism. Repeating the test with fresh samples can identify and minimize any variance due to environmental or procedural factors. Consistency across trials is essential to validate the circuit's detection performance.

This initial detection phase serves as a foundational step in broader research. By confirming that the resonator can accurately detect microplastics, it paves the way for second-generation testing, where the concentration of plastic particles will be quantified. This dual-phase testing process is essential for developing a robust, scalable solution for environmental microplastic monitoring.

4.2.2. SENSOR 1

As observed in The simulated sensor exhibited resonance frequencies at 4.073 GHz (-44.39 dB) and 4.98 GHz (-33.82 dB), while the measured sensor showed frequencies at 3.7937 GHz (-28.10 dB) and 4.6875 GHz (-43.99 dB). These discrepancies are attributed to practical factors such as material property variations, fabrication tolerances, contact imperfections, and the idealized conditions assumed in simulations.

Figure 4.2, there are significant differences between the simulated and measured responses of the sensor, particularly in terms of resonance frequency shifts and magnitudes. The simulated sensor exhibited resonance frequencies at 4.073 GHz (-44.39 dB) and 4.98 GHz (-33.82 dB), while the measured sensor showed frequencies at 3.7937 GHz (-28.10 dB) and 4.6875 GHz (-43.99 dB). These discrepancies are attributed to practical factors such as material property variations, fabrication tolerances, contact imperfections, and the idealized conditions assumed in simulations.

Figure 4.2 - Comparison of Simulated and Measured Resonance Responses for the Microplastic Detection Sensor.

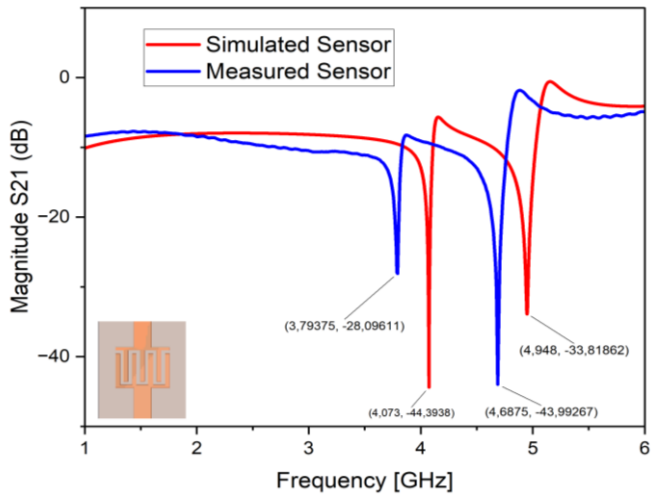

These factors contribute to the observed frequency shifts and magnitude changes between the simulated and real measurements. Nonetheless, the measured sensor's response remains acceptable, confirming its functional capability for detecting microplastic presence in real-world conditions.

Figure 4.3 illustrates how each element of the sensor setup influences the resonator's response across the tested frequency range, with resonance frequencies and magnitudes presented as follows:

- *Sensor Alone (Red):* The unloaded circuit resonator frequencies were observed at 3.7875 GHz and 4.6875 GHz with magnitudes of -27.8982 dB and -43.9926 dB, respectively.

- *Addition of the Channel (Blue)*: When the channel was added, the resonance frequencies shifted to 3.6437 GHz and 4.4562 GHz with magnitudes of -26.8511 dB and -42.9344 dB. This step highlights the influence of the channel on the overall response, showing that it introduces a slight reduction in both frequency and magnitude.

- *Addition of Water in the Channel (Green):* With water in the channel, the resonance frequencies further shifted to 3.5062 GHz and 4.1625 GHz with magnitudes of -22.7133 dB and -23.6763 dB. As a dielectric medium, the water introduces more significant frequency and magnitude changes, primarily due to its permittivity.

Figure 4.3 - Calibration Step-by-Step. Analysis of Sensor Response in Different Configurations.

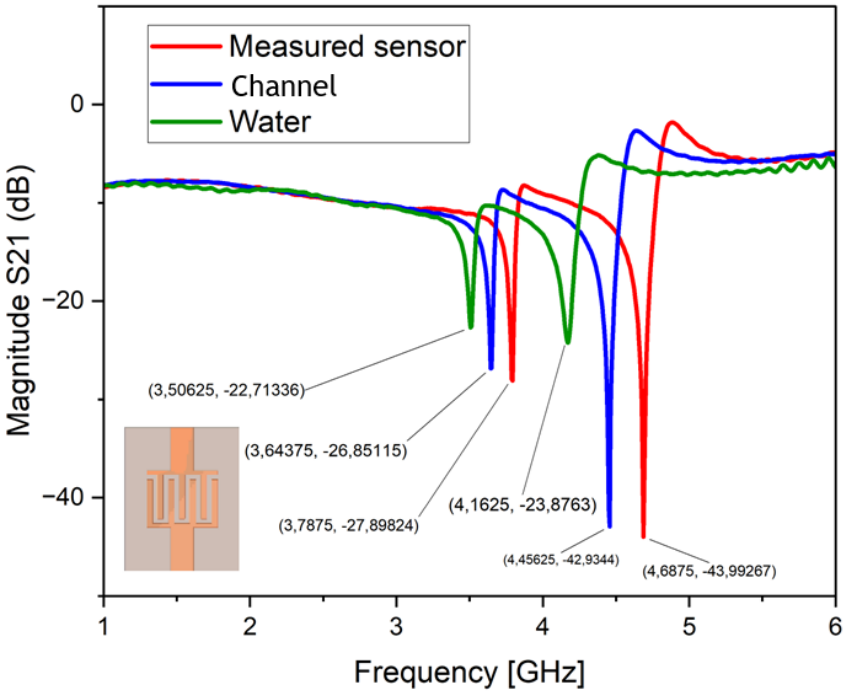

The incremental shifts in resonance frequency and magnitude demonstrate the sensor's sensitivity to different materials in the channel. Each component—sensor, channel, and water—contributes specific interference to the baseline, which must be accounted for to detect microplastics accurately. The substantial frequency shift and magnitude change when water is added underscore the dielectric effect of fluids in the sensor's response, confirming that the sensor can distinguish between unloaded and loaded conditions with certain accuracy. This analysis confirms the sensor’s potential for precisely detecting microplastics in aqueous solutions.

Figure 4.4 presents the comparative frequency response of the resonator in its unloaded (baseline) and loaded with plastic configurations designed to evaluate the resonator’s sensitivity to microplastic presence. In this figure, the red curve represents the response of the unloaded resonator, where the channel is filled only with water, while the blue curve shows the response when a microplastic particle is introduced into the channel at the center, simulating a real detection scenario.

Figure 4.4 - Frequency response comparison of Unloaded (Red) and Loaded (Blue) resonator configurations.

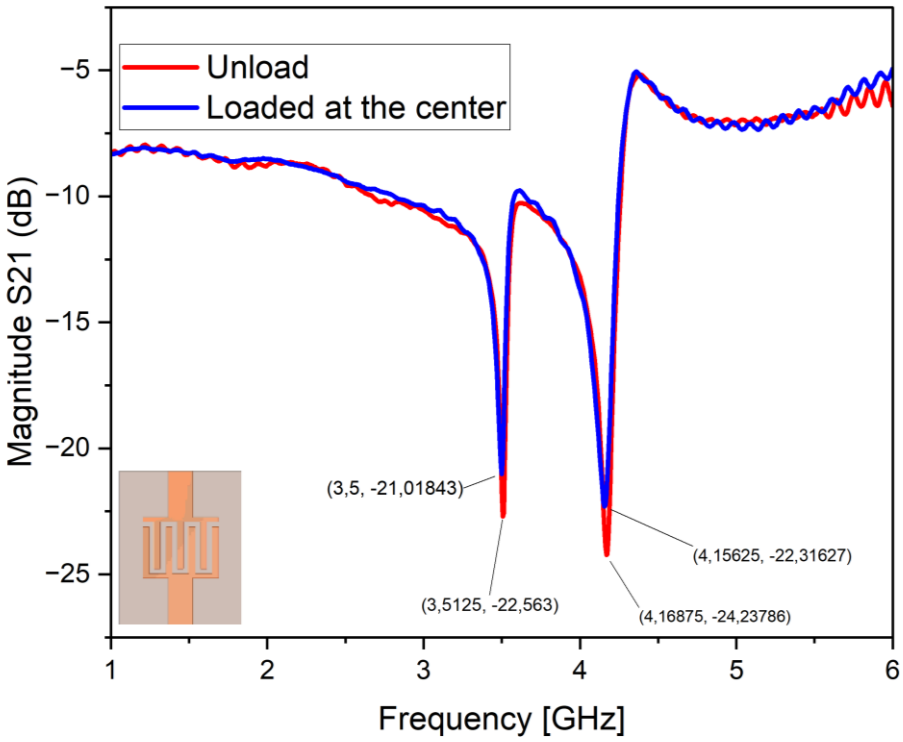

Notably, the resonance frequency exhibits a measurable shift upon loading. Specifically, the frequency shifts by approximately *12 MHz*, moving from *3.5 GHz* in the unloaded state to *3.512 GHz* in the loaded state. This frequency shift demonstrates the resonator's sensitivity to the dielectric properties of the added plastic particle, which impacts the electric field distribution within the resonator and results in a slight but detectable alteration of the resonance condition.

This observed shift, although subtle, is significant within the context of high-frequency resonators, where even minor frequency changes can indicate the presence of foreign materials within the resonant field. Additionally, the loaded configuration exhibits a change in signal magnitude at the resonant frequency, further underscoring the impact of the microplastic on the system. These findings validate the simulation predictions and support the possibility of using this resonator design as a practical microplastic sensor.

The plastic particle was placed at the resonator's center for this initial test. However, simulations have shown that other areas within the resonator experience even higher field intensities, which could potentially yield more incredible frequency shifts if exploited. Therefore, while the test confirms that the resonator is operational and accurate, it does not necessarily represent the most optimized detection scenario.

Due to uncertainties about the most effective positioning of the plastic sample on the resonator, a series of measurements were conducted to explore if specific placements could yield more accurate and consistent responses. The goal was to identify a position that maximizes the resonator's sensitivity to the plastic particle, thereby optimizing detection accuracy.

To assess the effect of particle placement, a set of tests was performed by moving the plastic sample incrementally along the channel, positioned both slightly before and after the printed resonator structure on the PCB. In these tests, each position was carefully adjusted to evaluate the resonance frequency response at various points along the resonator’s geometry, with particular attention given to the resonator’s “fingers” and “gaps” in the interdigital structure. Using controlled air pressure through a syringe, the plastic particle was precisely positioned at each designated spot on the resonator. This careful placement allowed for systematic testing across the resonator's length to identify regions with potentially higher sensitivity.

Figure 4.5 presents the resonance frequency responses of the resonator when the plastic particle is positioned at different points along its structure. This graph provides a detailed view of the frequency shifts as the particle moves across various resonator regions, illustrating the impact of its exact location on the resonator's response. The two most pronounced shifts occur when the particle is placed at Finger 2 and Gap 5. These locations correspond with regions of high electric field intensity, as identified in the simulation analysis in the previous chapter. These findings support the simulation's prediction that the resonator's sensitivity is heightened in these areas, as the electric field distribution is strongest here, causing significant perturbations when the plastic particle interacts with these fields.

Figure 4.5 - Shows the S_{21} transmission response for plastic particles at various positions along the channel, from the beginning to the end.

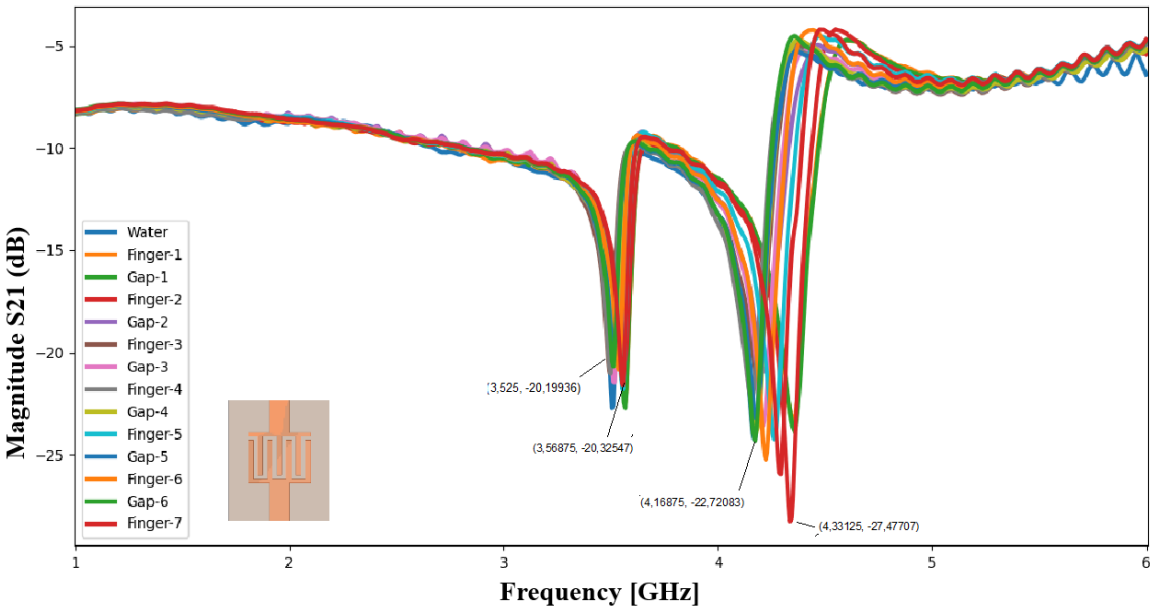

This experiment underlines the resonator's spatial sensitivity, confirming that certain positions on the resonator are more responsive to the presence of microplastic particles. Understanding this spatial variability is critical for optimizing the sensor's detection accuracy and may inform adjustments to the resonator design to further enhance its sensitivity and selectivity for microplastic detection applications.

In particular, more significant frequency shifts were observed when the plastic particle was placed on finger 2 and gap 5, where the electric field intensity is maximum (as seen in the previous section). This suggests that the resonator's response is highly position-dependent, with some areas yielding stronger detection signals than others, agreeing with the simulations. The position that achieved the highest frequency shift is likely near or within regions where the electric field lines converge, enhancing the resonator's sensitivity to changes in dielectric properties. This knowledge will be instrumental for future testing, as it identifies an optimal positioning approach that improves the reliability and sensitivity of the resonator's response.

In Figure 4.6, the most significant resonance frequency shifts are highlighted, showing a shift from (3.1525 GHz and 4.1687 GHz) with magnitudes of (-20.3254 dB and -24.2378 dB) in the unloaded state to (3.5687 GHz and 4.3312 GHz) with magnitudes of (-20.3254 dB and -27.4770 dB) in the loaded state. This indicates a resonance frequency shift of approximately Δf_1 =416.2 MHz and Δf_2 = 162.5 MHz, respectively, for the two resonant frequencies. The

magnitude shift from -24.2378 dB to -27.4770 dB at the second frequency confirms a notable change in the system's response due to the presence of the plastic particle. This substantial shift in both frequency and magnitude demonstrates that the sensor effectively detected the plastic and performed as expected.

Figure 4.6 - Resonance Frequency and Magnitude Shift for Sensor 1 Unloaded to Loaded State.

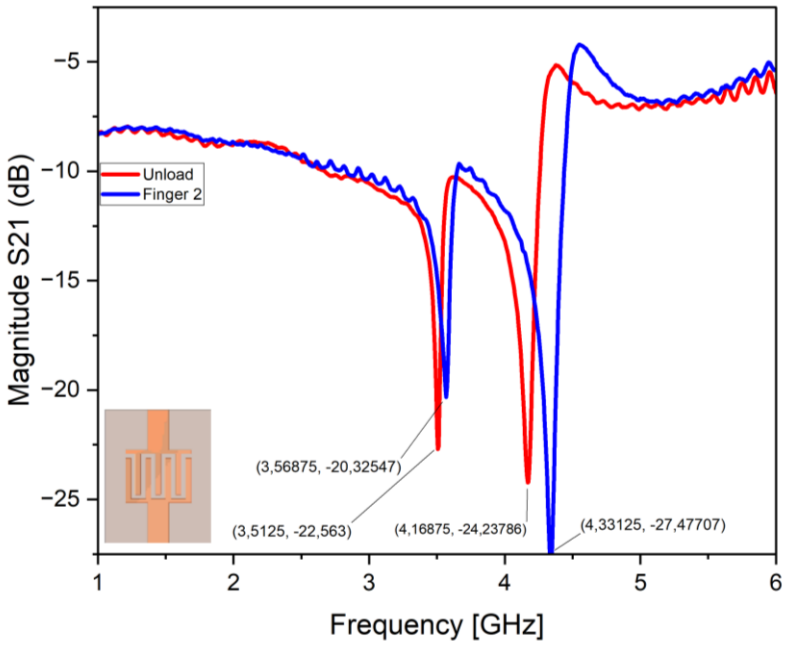

4.2.3. SENSOR 2

To continue the sensor performance evaluation, the analysis was extended to Sensor Model 2 following the same methodology applied to Model 1. This involved a comparative study between the simulated and measured responses, focusing specifically on resonance frequency and magnitude. As anticipated, significant differences were observed between the simulated and measured data, particularly in terms of resonance frequency shifts and variations in magnitude.

The analysis targeted the second and third resonant frequencies, as the first resonance showed minimal impact on detection accuracy and was thus excluded from detailed examination. The following results were obtained (shown in Figure 4.7):

Simulated Circuit Resonances:

- Second Resonance: 2.274 GHz, Magnitude: -11.378 dB

- Third Resonance: 2.79 GHz, Magnitude: -13.316 dB

Measured Circuit Resonances:

- Second Resonance: 2.386 GHz, Magnitude: -7.576 dB

- Third Resonance: 2.9525 GHz, Magnitude: -7.066 dB

These findings reveal a marked shift in both frequency and magnitude between the simulated and real-world results. Specifically, the resonance frequencies shifted by approximately 112 MHz and 162.5 MHz in the measured circuit relative to the simulated values. Additionally, the measured magnitudes were notably weaker than the simulation, with differences exceeding 3 dB in each resonance. The reason for the discrepancies is the same for sensor 1.

The comparison between simulated and real-world conditions highlights the inherent differences. It emphasizes the importance of accounting for practical factors during sensor design and calibration. This knowledge can be used to refine future sensor models and improve simulation accuracy by incorporating realistic parameters.

Figure 4.7 - Comparison of Simulated and Measured Resonance Frequencies and Magnitudes for Sensor Model

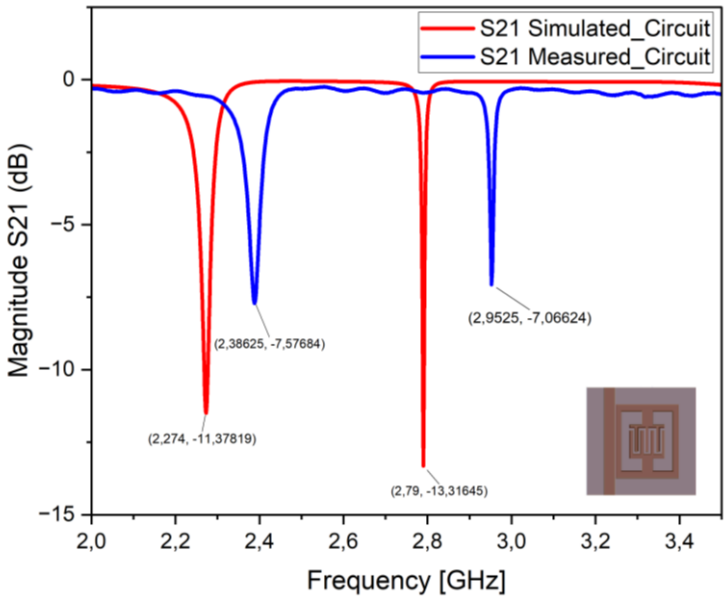

Figure 4.8 presents the calibration process for the sensor in isolation, where efforts were made to ensure that no external components or environmental factors could interfere with the sensor's response. This isolated measurement was essential to establish a baseline or

"unloaded" state for the sensor, ensuring that any subsequent variations in the response would be directly attributable to the presence of microplastics.

Baseline Calibration of the Unloaded Circuit (red): The initial calibration involved measuring the circuit by itself, devoid of any added materials or channels. This baseline configuration allows us to capture the sensor's intrinsic resonant frequencies and magnitudes without influence from additional components. The resonator demonstrated stable frequency and magnitude responses in this setup, establishing a reference point for unloaded conditions.

Adding the PDMS Channel (blue): After establishing the baseline, a PDMS (polydimethylsiloxane) channel was introduced on top of the resonator. This channel serves as the conduit through which water and microplastics flow later. The inclusion of the PDMS channel altered the system's resonant characteristics slightly due to its dielectric properties and physical proximity to the resonator. The resulting response showed resonant frequencies at 2.388 GHz and 2.9506 GHz, magnitudes of -7.2059 dB and -6.55 dB, respectively. This calibration helps assess the channel's direct impact on the sensor's response before introducing water or microplastics.

Figure 4.8 - Calibration Process of Sensor Model 2: Baseline, PDMS Channel Addition, and Water

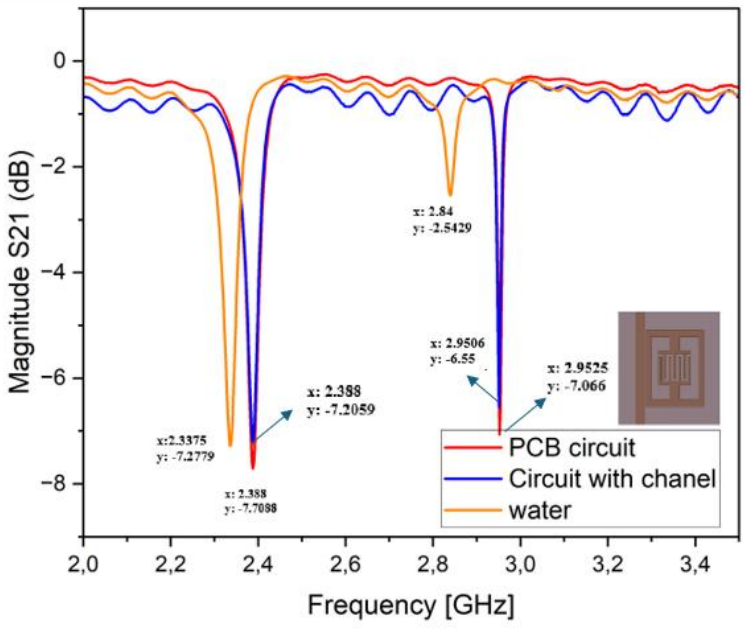

Introducing Water into the Channel (yellow): Water was added to the PDMS channel to simulate the sensor's unloaded "wet" condition. The presence of water further shifted the resonant frequencies and magnitudes due to its dielectric properties and interaction with the resonator's electric field. The unloaded response with water in the channel registered at 2.3375

GHz and 2.84 GHz for the resonance frequencies, with magnitudes of -7.278 dB and -2.543 dB. This final calibration with water establishes the sensor's unloaded baseline response for testing with microplastics.

This step-by-step calibration allows for precise monitoring of the sensor's response, where any subsequent changes can be confidently attributed to the presence and concentration of microplastics in the water.

Figure 4.9 - Microplastic Detection Test: Sensor Response to Tire Particle Introduction and Frequency/Magnitude Shifts

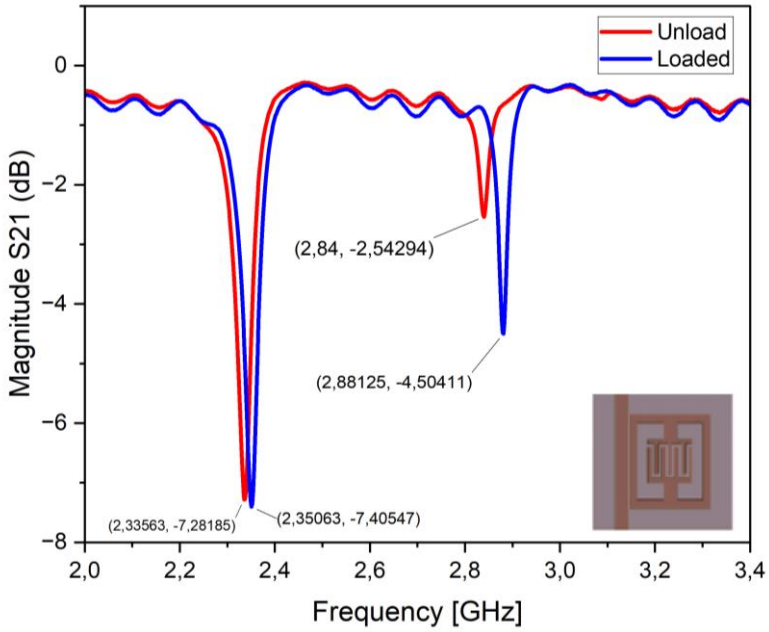

The final test in this stage aimed to validate the sensor's primary objective: detecting microplastics within a liquid medium. Following sensor calibration, a microplastic sample was introduced into the PDMS channel, simulating real-world conditions for microplastic detection. The chosen test sample was a tire particle string, sized approximately 0.3 x 0.3 x 0.3 mm^3, introduced as the Material Under Test (MUT) in the channel, as shown in the setup illustration. The transmission in showed in Figure 4.9. Once the microplastic particle reached the sensor's central region—where the electric field is most intense — the sensor's resonant frequency and magnitude shifted due to the presence of the plastic within the detection region. The resonant frequencies shifted to 2.3675 GHz and 2.9206 GHz, corresponding magnitudes of -6.9691 dB and -5.9877 dB. These shifts reflect a response that aligns with the sensor's design purpose for detecting microplastics. Specifically, the first frequency shift from 2.3375 GHz (the water-only baseline) to 2.3675 GHz indicates a 30 MHz shift. The second resonance shifts from 2.84 GHz (water-only baseline) to 2.9206 GHz corresponds to a 80.6 MHz shift. In terms of magnitude,

the changes were 0.3089 dB and 3.4443 dB, respectively, marking significant sensitivity to the presence of microplastics.

This experimental outcome confirms that the sensor effectively detects microplastic particles, showcasing its sensitivity to variations introduced by even small particles within the detection channel.

4.3. SECOND GENERATION OF MICROPLASTIC

In the second part of the bench test, the focus shifted to evaluating the sensor's ability to detect varying concentrations of microplastics in a distilled water solution. For this experiment, the microplastics used were small fragments derived from a sanded plastic bottle. These fragments were processed through three sieves to sort the particles by size. The sieves were arranged in a tower configuration, with the largest sieve at the top, followed by smaller ones.

The first sieve had a mesh size of 300 microns, the second was 150 microns, and the third was 75 microns. The process worked as follows: plastic fragments larger than 300 microns remained on the top sieve, while the fragments passing through the first sieve and retained in the second were considered to be less than 300 microns. Similarly, the particles that passed through the second sieve and were retained in the third sieve were smaller than 150 microns, and those passing through the third sieve were less than 75 microns. This method allowed the classification of microplastics using three sizes: particles larger than 300um, from 300um to 150um, and smaller than 150um.

After sieving, the portions of plastic from each sieve were carefully weighed using an electronic scale to determine the mass of the microplastics. These samples were then mixed with distilled water to prepare solutions with varying concentrations of microplastics. The plastic concentrations tested in water were 0.1%, 0.5%, and 1%, and for sieve 1, a sample concentration of 0.75% was also prepared based on the available plastic. This setup ensured the creation of a range of solutions for testing the sensor's sensitivity to different contamination levels.

Figure 4.10 illustrates the procedure used for sorting the microplastics and preparing the test solutions.

Figure 4.10 - Experimental Setup and Plastic Sample Preparation Process: (a) Three-Sieve System and Plastic Weighing on Electronic Scale, (b) Prepared Samples of Varying Microplastic Concentrations Mixed

with Water, (c) Zoomed View of Microplastic Dispersion, (d) VNA Screen Display During Measurement, (e) Close-Up of Cup-Style Container for Sample Holding, and (f) Full Measurement Setup.

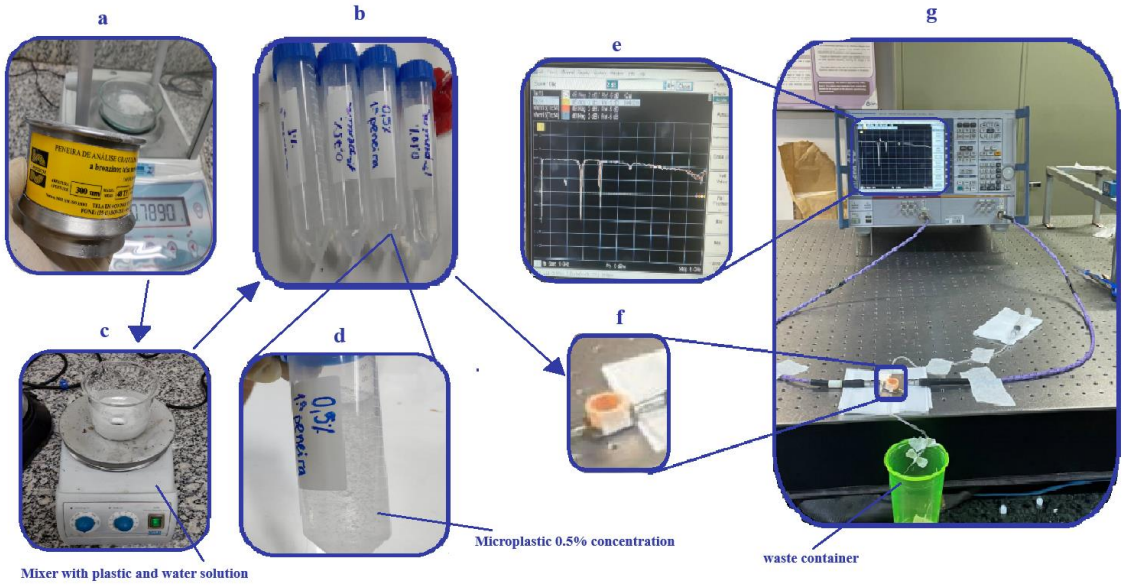

4.3.1. SENSOR 1

The next set of tests focused on sensor model 1, where microplastics with a mesh size of less than 300 microns were tested. The setup for this procedure followed the same protocol as previously described. Initially, the sensor was tested with just water to establish the baseline response, after which the microplastic particles were introduced into the system. These microplastics had been mixed using an electric mixer to ensure an even distribution. However, even with mixing, achieving the exact expected concentration was challenging. This was primarily due to the possibility of plastic particles accumulating at the tip of the syringe or within the hoses, which could result in a slight variation in the actual concentration in the solution.

Figure 4.11 presents the results for the water-only test in blue, with resonance frequencies of 4.275 GHz and 5.035 GHz. When microplastics were introduced, the resonance frequencies for the 0.1%, 0.5%, and 1% concentrations converged to approximately 4.205 GHz and 4.895 GHz values. Similarly, the 0.5% concentration also showed resonance frequencies of 4.23 GHz and 4.95 GHz.

Several factors can explain the convergence of the resonance frequencies across these different concentrations. First, the combination of particle size, mixing, and concentration may

not have been optimal, resulting in a less significant difference between the samples. Additionally, the position of the plastic particles within the sensor during testing could have contributed to the uniformity in the response. These factors likely played a role in minimizing the expected differences in resonance frequency, suggesting that further optimization of the experimental setup is needed to achieve more precise concentration-dependent results.

Figure 4.11 - Frequency Response of Sensor Model 1 for Varying Microplastic Concentrations (0.1%, 0.5%, 1%) with plastics larger than 300 um.

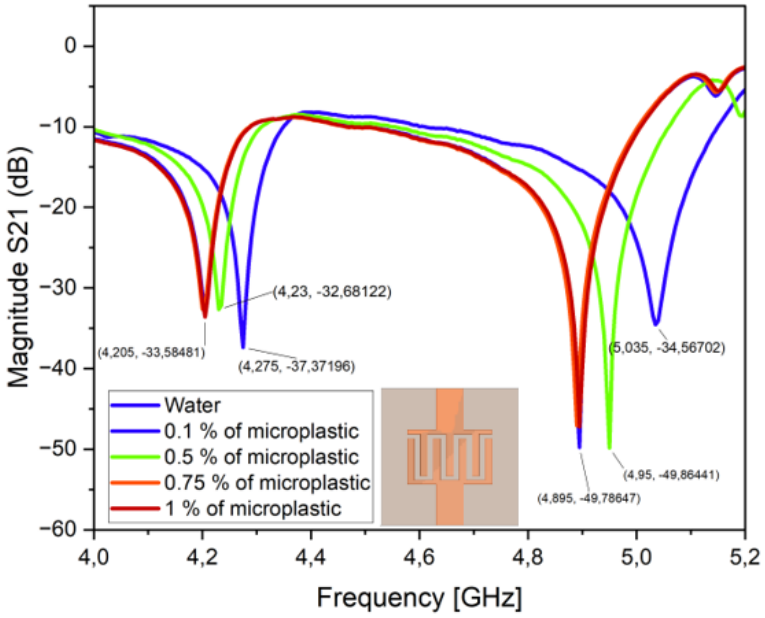

One significant observation from the tests is that, regardless of the specific concentration or particle distribution, the sensor consistently detected a variation in frequency whenever a quantity of plastic was present in the solution. This indicates that the sensor is sensitive to the presence of microplastics, even at varying concentrations. Although the frequency shifts were not always as large or distinct as expected, the fact that any plastic addition resulted in a detectable change in resonance frequency highlights the sensor's capability to respond to the presence of contaminants in the water.

The frequency shift, though subtle in some cases, is an important feature because it demonstrates that the sensor can identify microplastic particles in the water, which is the primary objective. This sensitivity suggests that the resonator can effectively act as an early-stage detection tool, even when the concentration or size of the particles is relatively low. Further refinement of the experimental conditions and sensor configuration could help improve the sensitivity and precision of the response, allowing for more accurate quantification and detection of microplastic contamination at various levels.

For the concentration test with microplastics of sizes less than 300 micrometers, Figure 4.12 illustrates the resonance frequency responses observed at various concentration levels. The results reveal a relatively minor difference of only 6 MHz between the different concentrations. However, a notable frequency shift is apparent when comparing the baseline (water-only) response to the plastic-laden solutions. Specifically, resonance shifts from 4.275 GHz to 4.175 GHz and from 5.035 GHz to 4.865 GHz, highlighting the sensor's sensitivity to even small microplastic particles. This shift underscores the sensor's ability to detect subtle changes in the medium, validating its potential in detecting microplastic presence and variations in concentration across particle sizes.

Figure 4.12 - Resonance Frequency Shift in Response to Microplastic Concentrations under 300 Micrometers

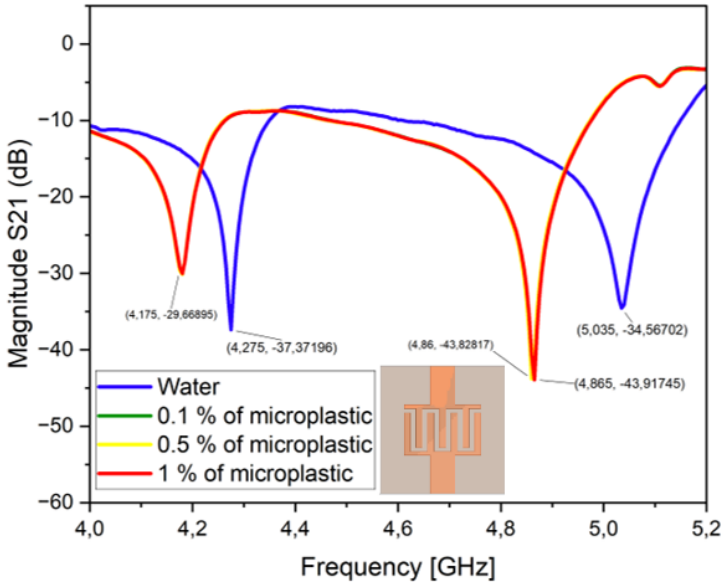

Figure 4.13 presents the frequency responses for varying concentrations for the smallest dimension of microplastic particles tested. The response at a concentration of 0.1% is shown in green, with resonance frequencies of 4.19 GHz and 4.87 GHz. At a concentration of 0.5%, the response appears in orange, with resonance frequencies of 4.21 GHz and 4.92 GHz. Finally, the response for the 1% concentration is represented in red, showing frequencies of 4.21 GHz and 4.9 GHz.

The data suggests that while there is a minimal increase in resonance frequency with higher concentrations, the sensor still consistently registers a shift in resonance frequency upon detecting the presence of microplastic particles, even at smaller particle sizes. The results indicate that the sensor is sensitive enough to detect microplastics across a range of small

concentrations. However, the relatively minor frequency shifts across different concentrations may suggest a limit to the sensor's sensitivity at such small particle sizes.

Figure 4.13 - Frequency Response of Sensor for Varying Concentrations of Microplastic Particles Under 150 Micrometers.

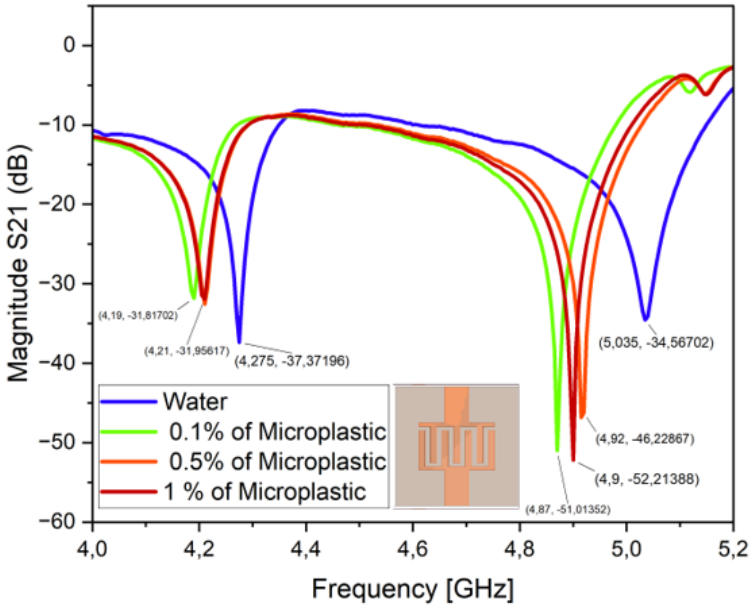

4.3.2. SENSOR 2

The results obtained from this setup highlight the sensor's sensitivity to different microplastic concentrations, starting with microplastic particles larger than 300 microns. Note that sensor 2 was modified for this measurement, adding a cylindrical container on the top of the interdigital resonance. Figure 4.14 presents the resonance frequency responses for each tested concentration level. The unloaded system, containing only water, shows resonance frequencies at 2.24 GHz and 3.37 GHz. Upon introducing a 0.1% microplastic concentration, the response shifts slightly to 2.275 GHz and 3.265 GHz, shown in light blue. At a 0.5% concentration (yellow), the resonance frequencies shift to 2.36 GHz and 3.265 GHz, while at a 1% concentration (red), they adjust to 2.26 GHz and 3.325 GHz. These results confirm that sensor model 2 detects shifts in resonance frequencies in response to the presence of microplastics, even at low concentration levels. The progressive frequency shifts correspond to increasing concentration, demonstrating the sensor's ability to quantify microplastic density changes. This behavior aligns with the sensor's design objective, confirming its capacity to detect microplastic pollutants accurately across various concentrations.

Figure 4.14 - Resonance Frequency Responses of Sensor Model 2 for Various Microplastic Concentrations (larger than 300 Microns).

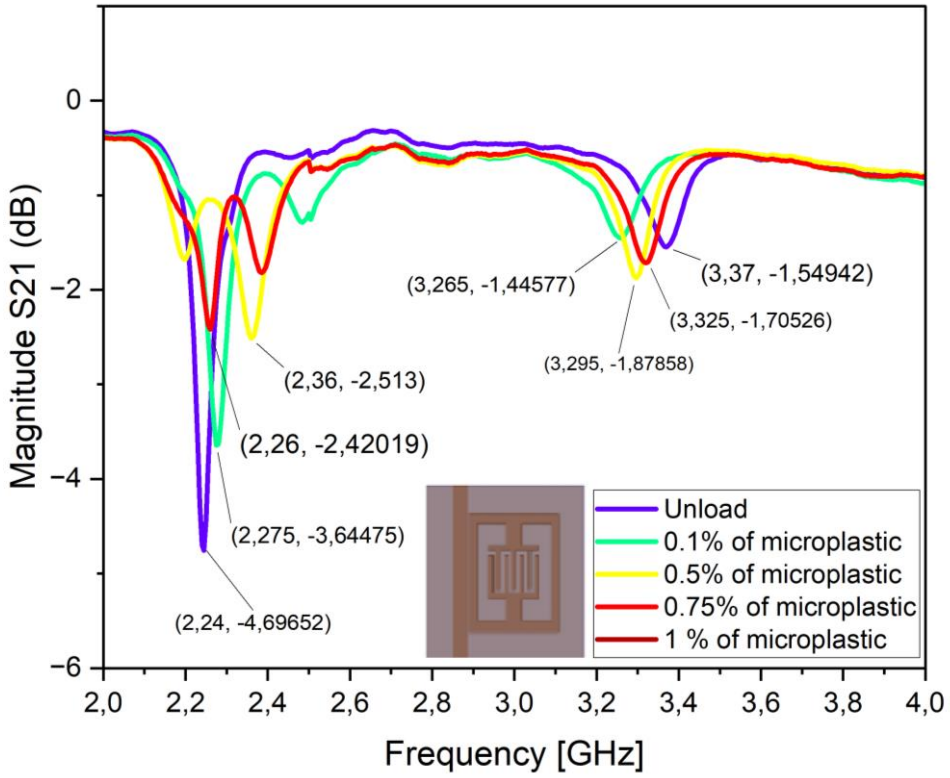

For the concentration range between 300 and 150 microns, the initial observation highlights that the sensor's sensitivity predominantly operates in the 2- to 2.5 GHz range. The sensor maintains a baseline response in this frequency range in the unloaded state, serving as a reliable reference. When introducing a 0.1% microplastic concentration, the resonance frequency shifts slightly to 2.295 GHz, shown in light blue. For higher concentrations of 0.5% and 1%, indicated in red and yellow, respectively, the resonance frequencies converge to approximately 2.42 GHz, demonstrating a measurable shift from the baseline. This shows that the sensor did not perform linearly as we increased the concentrations, indicating that a more precise measurements should be performed.

For pollutant plastic particles smaller than 150um, the analysis region was further narrowed to the range of 2.2 GHz to 2.4 GHz to enhance sensitivity and focus on the observable frequency shifts within this specific range. In the unloaded state, the sensor maintained a stable baseline response. When introducing a 0.1% plastic concentration, represented by the light blue curve, the resonance frequency shifted from 2.335 GHz to 2.315 GHz, indicating the low concentration's subtle yet measurable effect. For the higher concentrations of 0.5% and 1%, represented in yellow and red, respectively, the sensor exhibited a shared resonance frequency at 2.2975 GHz. This trend emphasizes that, for this sensor model, intermediate frequency shifts

occur with smaller concentrations. In contrast, shifts may stabilize at higher concentrations, reflecting a reduced sensitivity gradient in this specific range. It is important to notice that the resonant frequency varies linearly in these measurements.

Figure 4.15 - Frequency Response Shifts of Sensor Model 2 for Microplastic Concentrations Between 300 and 150 Microns.

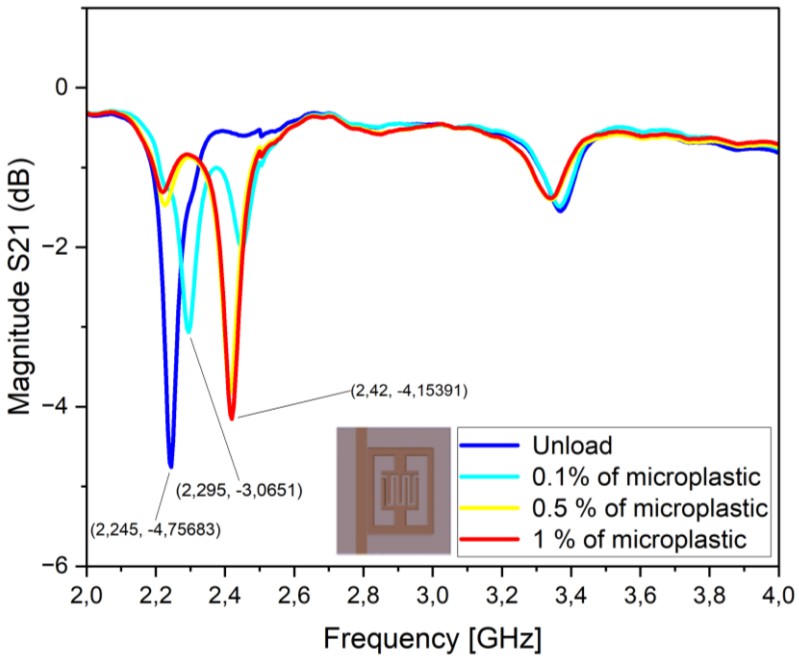

Figure 4.16 - Frequency Response Shifts for Plastic Pollutant Concentrations Between 150 and 75 Microns.

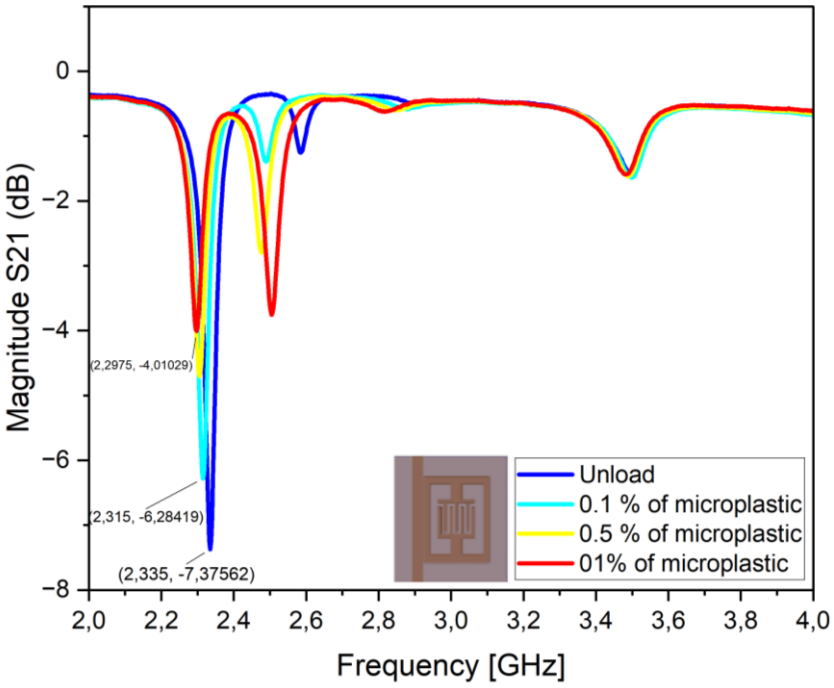
Magnitude S21 (dB)
Frequency [GHz]
0
−2
−4
−6
−8
2,0
2,2
2,4
2,6
2,8
3,0
3,2
3,4
3,6
3,8
4,0
(2,2975, -4,01029)
(2,315, -6,28419)
(2,335, -7,37562)
Unload
0.1 % of microplastic
0.5 % of microplastic
01% of microplastic

4.4. SUMMARY OF THE MEASUREMENTS

The bench tests conducted for sensor models 1 and 2 demonstrate each sensor's response to microplastic pollutants in water, assessed across both detection phases—first generation (presence detection) and second generation (concentration measurement). Here is an in-depth summary of the results and observations across both sensor models and testing phases:

4.4.1. SENSOR MODEL 1

4.4.1.1. FIRST GENERATION (PRESENCE DETECTION)

Resonance Frequency Shift: Sensor Model 1 successfully detects the presence of microplastics, demonstrated by measurable resonance frequency shifts between the unloaded and loaded states.

Sensitivity to Particle Position: During tests, the sensor displayed higher sensitivity to plastic particles at specific resonator points, correlating with the electric field distribution patterns identified in simulations. The largest frequency shifts were noted when particles were positioned in areas of the highest electric field concentration. The sensor provides a consistent shift in resonance frequency, verifying its suitability for detecting the microplastic presence in the water.

4.4.1.2. SECOND GENERATION

Resonance Response to Concentration Variations: For microplastic sizes up to 300 microns, shifts in resonance frequencies were observed across the different concentrations tested (0.1%, 0.5%, and 1%).

Challenges with Smaller Particles: When particle sizes decreased to 150 microns and below, the sensor's responses began to converge for higher concentrations, indicating a potential saturation or limitation in sensitivity when exposed to densely concentrated microplastic suspensions or smaller particles. While the sensor provides reliable shifts in resonance frequencies at lower concentrations, further refinement may be required to accurately distinguish higher concentrations or detect smaller particle sizes with greater precision.

4.4.2. SENSOR MODEL 2

4.4.2.1. FIRST GENERATION:

System Modifications for Improved Detection: Unlike Model 1, Sensor Model 2 showed minimal response when using the microchannel setup for the presence detection tests. To address this, the experimental setup was modified to use an open container, enabling more effective interaction between the sensor and the microplastic-laden water. *Frequency Response Shift:* Once the new setup was applied, significant frequency shifts were observed, confirming Model 2's ability to detect the presence of microplastic particles down to 150 microns.

4.4.2.2. SECOND GENERATION

Resonance Sensitivity at Lower Frequencies: Sensor Model 2's sensitivity range was more responsive at lower frequency bands (between 2 GHz and 2.5 GHz), displaying resonance shifts in response to increased concentrations. For instance, 0.1%, 0.5%, and 1% concentrations presented distinctive frequency shifts when the particles were between 150 and 75 microns.

Observations and Limitations: At higher concentrations and smaller particle sizes, the resonant shifts became subtler, with some overlaps in frequency response, indicating a possible threshold for the sensor's concentration sensitivity. Sensor Model 2 exhibited reliable detection capabilities at lower frequencies, with distinguishable shifts for concentration levels up to a certain threshold but may require further tuning or design adjustments for more refined differentiation at higher concentrations.

Both sensor models demonstrated competency in detecting microplastic presence, with distinguishable shifts in resonance frequencies confirming their effectiveness. Model 1 excelled in presence detection and initial concentration measurements but showed limits in distinguishing higher concentrations or smaller particle sizes. Model 2, while requiring an alternative setup for optimal performance, offered a broader detection capability within a lower frequency range, especially effective at detecting concentrations at the 150–75-micron particle scale. These results suggest that both models hold promises for detecting microplastic pollutants in water, with areas for improvement in handling high-density and smaller-sized microplastics.

Table 4.1 presents the results of the most significant frequency shifts observed for each sensor model and the associated differences in magnitude. This table shows that Sensor Model 1 demonstrates a quality factor (Q-factor) of 74.11 in the unloaded condition and 99.14 when loaded. Similarly, Sensor Model 2 shows a Q-factor of 69.20 when unloaded and 73.75 when loaded.

The difference in Q-factor between the loaded and unloaded states for both sensor models suggest interesting insights into the sensors' performance and interaction with the test medium. For Sensor Model 1, the Q-factor increases in the loaded condition, indicating that this model experiences a relatively greater concentration of energy near the resonant frequency when introducing microplastics. This increase in Q-factor may be attributed to a better energy confinement due to the physical or electromagnetic interaction between the resonator and the microplastic particles. In practical terms, a higher Q-factor under load often means the sensor is more sensitive to environmental changes, thereby enhancing its ability to detect microplastics or similar contaminants.

First generation of microplastic				
	Unload		Loaded	
	Sensor 1	Sensor 2	Sensor 1	Sensor 2
R.Freq 1 GHz	3.512	2.337	3.568	2.367
R. Freq 2 GHz	4.168	2.84	4.331	2.92
Δfreq1 GHz	-----	-----	0.056	0,030
Δfreq2 GHz	-----	-----	0.163	0.806
Mag 1 dB	-22.563	-6.969	-20.325	-7.135
Mag 2 dB	-23.876	-5.987	-27.477	-2.542
ΔMag 1 dB	-----	-----	-2.388	-0.166
ΔMag 2 dB	-----	-----	7.152	-3.445
Q-factor 1	74.11	69,20	99.14	73.75

Table 4.1 - Frequency Shifts and Quality Factors for Sensor Models in Loaded and Unloaded Conditions.

In contrast, Sensor Model 2 also shows an increase in Q-factor when loaded, but the change is less pronounced than Model 1. This could be due to differences in the design, such as variations in the resonator's geometry, material composition, or the distribution of the electric field around the sensor. These factors might influence how well the resonator interacts with the microplastics in the channel. The relatively smaller increase in Q-factor for Model 2 could imply that its sensitivity is somewhat lower than that of Model 1, potentially making it less effective for detecting very fine shifts or minute contaminant concentrations.

CHAPTER 5

5. CONCLUSIONS

This research successfully developed and validated an approach for detecting microplastic particles in water using resonant sensor technology. The study followed a comprehensive process, beginning with theoretical modeling and simulations, progressing to sensor fabrication, and culminating in systematic bench testing to evaluate performance under real-world and near-real-world conditions. However, due to laboratory limitations, it was not possible to isolate various factors present in tap water, such as salt, iron, or other particles, which could influence the results. The following conclusions detail the effectiveness of each stage in the methodology and summarize the main findings. The methodology was designed to comprehensively explore resonant sensors' microplastic detection capabilities. The approach involved:

- Theoretical Modeling: Building foundational knowledge on resonance principles to optimize sensor design for detecting microplastic-induced shifts.
- Simulation: Simulations were essential for testing initial hypotheses about resonance shifts in response to microplastics. Various sensor configurations were modeled to study the electric field distributions and resonance frequency shifts, particularly emphasizing regions within the resonator exhibiting high field intensities. Later, this proved crucial during experimental testing. Simulations provided critical insights into the behavior of the resonator when exposed to microplastic particles:

The simulations showed regions within the resonator that generated the strongest electric fields, which would likely experience the most significant shifts upon introducing microplastics. This insight guided the positioning of microplastic particles during testing and helped optimize sensor design for maximum sensitivity. Simulations indicated that detectable shifts in resonance frequency would be achievable for microplastic sizes from 300 microns down to 75 microns, depending on concentration and placement within the field. The results highlighted the expected sensitivity range for each sensor model.

Based on the simulation results, two sensor models (Model 1 and Model 2) were designed and fabricated on printed circuit boards (PCBs). The design of these sensors aimed to create high sensitivity to material changes within the resonator's detection field, as predicted in simulations. The fabrication phase focused on translating the simulated designs into physical sensor prototypes:

- *PCB-Based Fabrication:* Both sensors were fabricated on PCBs, incorporating microchannel designs to allow controlled water flow with suspended microplastic particles. The PCB fabrication process ensured consistency and precise geometries that aligned with simulation parameters.
- *Bench Testing Setup:* A custom test bench was constructed, including a vector network analyzer (VNA) for precise resonance frequency measurements, a pump to control flow rates, and microchannels for introducing microplastic samples. This setup provided a controlled environment to replicate real-world testing conditions. The bench tests focused on evaluating the sensors in two main configurations—unloaded (with water only) and loaded (with water and microplastics)—to determine resonance shifts and sensitivity:
- *Presence Detection (First Generation Tests):* Both sensor models effectively detected microplastic presence through noticeable frequency shifts. The tests confirmed that particles positioned at high-field regions within the resonator generated the largest resonance shifts, in line with simulation predictions.
- *Concentration Detection (Second Generation Tests*): The sensors were also evaluated for their ability to differentiate microplastic concentrations in water. Resonance shifts were detected across various concentration levels (0.1%, 0.5%, and 1%) and particle sizes (300 microns, 150 microns, and 75 microns). However, limitations emerged at smaller particle sizes and higher concentrations, indicating a potential threshold for each sensor model's sensitivity.

The study's results demonstrated that resonant sensors can effectively detect microplastic particles in water. In conclusion, this research demonstrates that PCB-based resonant sensors offer a viable solution for microplastic detection in water, with clear potential for further development. The process of combining simulation, careful fabrication, and bench testing proved to be a robust methodology for developing highly sensitive resonant sensors.

5.1. FUTURE PERSPECTIVES

Future work could focus on:

- Enhancing Sensor Sensitivity: Increasing sensitivity to detect smaller particle sizes and higher concentrations, possibly by optimizing resonator geometry or exploring alternative materials.
- Field Testing: Extending testing to real-world water samples containing environmental microplastics to evaluate sensor performance in varied conditions.
- Integration with Real-Time Monitoring Systems: Integrating these sensors into portable or in-line monitoring systems for continuous water quality assessment.

This research opens up exciting prospects for enhancing sensor sensitivity, detection range, and versatility in microplastic and contaminant detection. Refinements in circuit design, material selection, and calibration techniques could lead to detecting even smaller microplastic particles and trace levels of other pollutants. Advancing these parameters would increase the sensor's robustness and adaptability across diverse environments, from aquatic ecosystems to food and beverage safety applications.

This research presents an academically significant microplastic detection methodology with clear commercial potential. With its adaptable design and proven efficacy, the proposed RF resonator technology stands as a promising solution for pressing challenges in pollution monitoring, food safety, and, potentially, healthcare diagnostics. Through continued advancements, this work addresses current environmental concerns and paves the way for future innovations in high-sensitivity, RF-based detection technologies.

REFERENCES

[1] K. Ziani *et al.*, "Microplastics: A Real Global Threat for Environment and Food Safety: A State of the Art Review," Feb. 01, 2023, *MDPI*. doi: 10.3390/nu15030617.

[2] S. Ghosh, J. K. Sinha, S. Ghosh, K. Vashisth, S. Han, and R. Bhaskar, "Microplastics as an Emerging Threat to the Global Environment and Human Health," Jul. 01, 2023, *Multidisciplinary Digital Publishing Institute (MDPI)*. doi: 10.3390/su151410821.

[3] Y. Li, L. Tao, Q. Wang, F. Wang, G. Li, and M. Song, "Potential Health Impact of Microplastics: A Review of Environmental Distribution, Human Exposure, and Toxic Effects," *Environment & Health*, vol. 1, no. 4, pp. 249–257, Oct. 2023, doi: 10.1021/envhealth.3c00052.

[4] P. Roy, A. K. Mohanty, and M. Misra, "Microplastics in ecosystems: their implications and mitigation pathways," *Environmental Science: Advances*, vol. 1, no. 1, pp. 9–29, Apr. 2022, doi: 10.1039/d1va00012h.

[5] M. Wagner *et al.*, "Microplastics in freshwater ecosystems: what we know and what we need to know," *Environ Sci Eur*, vol. 26, no. 1, pp. 1–9, Dec. 2014, doi: 10.1186/s12302-014-0012-7.

[6] "r6Plastic planet_ How tiny plastic particles are polluting our soil".

[7] B. Pandey *et al.*, "Microplastics in the Ecosystem: An Overview on Detection, Removal, Toxicity Assessment, and Control Release," Jan. 01, 2023, *MDPI*. doi: 10.3390/w15010051.

[8] G. Lamichhane *et al.*, "Microplastics in environment: global concern, challenges, and controlling measures," Apr. 01, 2023, *Institute for Ionics*. doi: 10.1007/s13762-022-04261-1.

[9] M. G. Kibria, N. I. Masuk, R. Safayet, H. Q. Nguyen, and M. Mourshed, "Plastic Waste: Challenges and Opportunities to Mitigate Pollution and Effective Management," Feb. 01, 2023, *Springer Science and Business Media Deutschland GmbH*. doi: 10.1007/s41742-023-00507-z.

[10] Y. Lee, J. Cho, J. Sohn, and C. Kim, "Health Effects of Microplastic Exposures: Current Issues and Perspectives in South Korea," May 01, 2023, *Yonsei University College of Medicine*. doi: 10.3349/ymj.2023.0048.

[11] S. S. Shetty *et al.*, "Environmental pollutants and their effects on human health," Sep. 01, 2023, *Elsevier Ltd*. doi: 10.1016/j.heliyon.2023.e19496.

[12] L. K. Bhardwaj, P. Rath, P. Yadav, and U. Gupta, "Microplastic contamination, an emerging threat to the freshwater environment: a systematic review," *Environmental Systems Research*, vol. 13, no. 1, Feb. 2024, doi: 10.1186/s40068-024-00338-7.

[13] A. A. Koelmans, N. H. Mohamed Nor, E. Hermsen, M. Kooi, S. M. Mintenig, and J. De France, "Microplastics in freshwaters and drinking water: Critical review and assessment of data quality," May 15, 2019, *Elsevier Ltd*. doi: 10.1016/j.watres.2019.02.054.

[14] T. S. M. Amelia, W. M. A. W. M. Khalik, M. C. Ong, Y. T. Shao, H. J. Pan, and K. Bhubalan, "Marine microplastics as vectors of major ocean pollutants and its hazards to the marine ecosystem and humans," Dec. 01, 2021, *Springer Science and Business Media Deutschland GmbH*. doi: 10.1186/s40645-020-00405-4.

[15] K. Ziani *et al.*, "Microplastics: A Real Global Threat for Environment and Food Safety: A State of the Art Review," *Nutrients*, vol. 15, no. 3, 2023, doi: 10.3390/nu15030617.

[16] C. Wang, J. Zhao, and B. Xing, "Environmental source, fate, and toxicity of microplastics," Apr. 05, 2021, *Elsevier B.V.* doi: 10.1016/j.jhazmat.2020.124357.

[17] Z. Huang, B. Hu, and H. Wang, "Analytical methods for microplastics in the environment: a review," *Environ Chem Lett*, vol. 21, no. 1, pp. 383–401, Feb. 2023, doi: 10.1007/s10311-022-01525-7.

[18] V. Kaing, Z. Guo, T. Sok, D. Kodikara, F. Breider, and C. Yoshimura, "Photodegradation of biodegradable plastics in aquatic environments: Current understanding and challenges," Feb. 10, 2024, *Elsevier B.V.* doi: 10.1016/j.scitotenv.2023.168539.

[19] J. C. Prata, J. P. da Costa, I. Lopes, A. C. Duarte, and T. Rocha-Santos, "Environmental exposure to microplastics: An overview on possible human health effects," Feb. 01, 2020, *Elsevier B.V.* doi: 10.1016/j.scitotenv.2019.134455.

[20] M. J. Stapleton and F. I. Hai, "Microplastics as an emerging contaminant of concern to our environment: a brief overview of the sources and implications," Dec. 01, 2023, *NLM (Medline)*. doi: 10.1080/21655979.2023.2244754.

[21] N. Kalogerakis *et al.*, "Microplastics generation: Onset of fragmentation of polyethylene films in marine environment mesocosms," *Front Mar Sci*, vol. 4, no. MAR, Mar. 2017, doi: 10.3389/fmars.2017.00084.

[22] S. Siddiqui, S. J. Hutton, J. M. Dickens, E. I. Pedersen, S. L. Harper, and S. M. Brander, "Natural and synthetic microfibers alter growth and behavior in early life stages of estuarine organisms," *Front Mar Sci*, vol. 9, Jan. 2023, doi: 10.3389/fmars.2022.991650.

[23] S. Acharya, S. S. Rumi, Y. Hu, and N. Abidi, "Microfibers from synthetic textiles as a major source of microplastics in the environment: A review," Sep. 01, 2021, *SAGE Publications Ltd*. doi: 10.1177/0040517521991244.

[24] S. Santonicola, M. Volgare, M. Cocca, G. Dorigato, V. Giaccone, and G. Colavita, "Impact of Fibrous Microplastic Pollution on Commercial Seafood and Consumer Health: A Review," Jun. 01, 2023, *MDPI*. doi: 10.3390/ani13111736.

[25] Q. Lin *et al.*, "Occurrence of microplastics in three types of household cleaning products and their estimated emissions into the aquatic environment," *Science of the Total Environment*, vol. 902, Dec. 2023, doi: 10.1016/j.scitotenv.2023.165903.

[26] R. Z. Habib *et al.*, "Trends of microplastic abundance in personal care products in the United Arab Emirates over the period of 3 years (2018–2020)," *Environmental Science and Pollution Research*, vol. 29, no. 59, pp. 89614–89624, Dec. 2022, doi: 10.1007/s11356-022-21773-y.

[27] "Proceedings of the Second Research Workshop on Microplastic Marine Debris," 2012.

[28] W. Huang *et al.*, "Microplastics and associated contaminants in the aquatic environment: A review on their ecotoxicological effects, trophic transfer, and potential impacts to human health," *J Hazard Mater*, vol. 405, Mar. 2021, doi: 10.1016/j.jhazmat.2020.124187.

[29] "Microplastic pollution: the causes, consequences and issues for investors First Sentier MUFG Sustainable Investment Institute."

[30] "European Commission-Press release The Commission proposes measures to reduce microplastic pollution from plastic pellets."

[31] F. Mendrik, R. Fernández, C. R. Hackney, C. Waller, and D. R. Parsons, "Non-buoyant microplastic settling velocity varies with biofilm growth and ambient water salinity," *Commun Earth Environ*, vol. 4, no. 1, Dec. 2023, doi: 10.1038/s43247-023-00690-z.

[32] S. Gupta *et al.*, "Atmospheric Microplastics: Perspectives on Origin, Abundances, Ecological and Health Risks," Oct. 01, 2023, *Springer Science and Business Media Deutschland GmbH*. doi: 10.1007/s11356-023-28422-y.

[33] A. A. de Souza Machado, W. Kloas, C. Zarfl, S. Hempel, and M. C. Rillig, "Microplastics as an emerging threat to terrestrial ecosystems," Apr. 01, 2018, *Blackwell Publishing Ltd*. doi: 10.1111/gcb.14020.

[34] M. Rai *et al.*, "Microplastic Pollution in Terrestrial Ecosystems and Its Interaction with Other Soil Pollutants: A Potential Threat to Soil Ecosystem Sustainability," Jun. 01, 2023, *Multidisciplinary Digital Publishing Institute (MDPI)*. doi: 10.3390/resources12060067.

[35] C. O. Egbeocha, S. Malek, C. U. Emenike, and P. Milow, "Feasting on microplastics: Ingestion by and effects on marine organisms," 2018, *Inter-Research*. doi: 10.3354/ab00701.

[36] M. S. Savoca, A. G. McInturf, and E. L. Hazen, "Plastic ingestion by marine fish is widespread and increasing," *Glob Chang Biol*, vol. 27, no. 10, pp. 2188–2199, May 2021, doi: 10.1111/gcb.15533.

[37] A. A. De Souza Machado *et al.*, "Microplastics Can Change Soil Properties and Affect Plant Performance," *Environ Sci Technol*, vol. 53, no. 10, pp. 6044–6052, May 2019, doi: 10.1021/acs.est.9b01339.

[38] M. E. McHale and K. L. Sheehan, "Bioaccumulation, transfer, and impacts of microplastics in aquatic food chains," *Journal of Environmental Exposure Assessment*, vol. 3, no. 3, Jul. 2024, doi: 10.20517/jeea.2023.49.

[39] N. Rafa *et al.*, "Microplastics as carriers of toxic pollutants: Source, transport, and toxicological effects," Feb. 15, 2024, *Elsevier Ltd*. doi: 10.1016/j.envpol.2023.123190.

[40] M. Bergmann, L. Gutow, and M. Klages, "Marine Anthropogenic Litter."

[41] S. Zaheer Ud Din, K. Shah, N. Bibi, H. H. Mahboub, and M. A. Kakakhel, "Recent Insights into the Silver Nanomaterials: an Overview of Their Transformation in the Food Webs and Toxicity in the Aquatic Ecosystem," Feb. 01, 2023, *Institute for Ionics*. doi: 10.1007/s11270-023-06134-w.

[42] G. Murtaza, M. T. Shehzad, S. Kanwal, Z. U. R. Farooqi, and G. Owens, "Biomagnification of potentially toxic elements in animals consuming fodder irrigated with sewage water," *Environ Geochem Health*, vol. 44, no. 12, pp. 4523–4538, Dec. 2022, doi: 10.1007/s10653-022-01211-1.

[43] C. Corinaldesi *et al.*, "Multiple impacts of microplastics can threaten marine habitat-forming species," *Commun Biol*, vol. 4, no. 1, Dec. 2021, doi: 10.1038/s42003-021-01961-1.

[44] M. Bergmann, L. Gutow, and M. Klages, "Marine Anthropogenic Litter."

[45] X. Ouyang, C. Panti, S. Canicci, R. Li, and N. F. Y. Tam, "Editorial: Impact of marine debris on marine ecosystems and organisms," Jan. 27, 2023, *Frontiers Media S.A.* doi: 10.3389/fmars.2023.1136431.

[46] W. K. Ho, J. C. F. Law, J. C. W. Lo, I. K. X. Chng, C. H. H. Hor, and K. S. Y. Leung, "Sorption Behavior, Speciation, and Toxicity of Microplastic-Bound Chromium in Multisolute Systems," *Environ Sci Technol Lett*, vol. 10, no. 1, pp. 27–32, Jan. 2023, doi: 10.1021/acs.estlett.2c00689.

[47] S. L. Wright and F. J. Kelly, "Plastic and Human Health: A Micro Issue?," *Environ Sci Technol*, vol. 51, no. 12, pp. 6634–6647, Jun. 2017, doi: 10.1021/acs.est.7b00423.

[48] C. Campanale, C. Massarelli, I. Savino, V. Locaputo, and V. F. Uricchio, "A detailed review study on potential effects of microplastics and additives of concern on human health," Feb. 02, 2020, *MDPI AG*. doi: 10.3390/ijerph17041212.

[49] C. Q. Y. Yong, S. Valiyaveettil, and B. L. Tang, "Toxicity of microplastics and nanoplastics in Mammalian systems," Mar. 01, 2020, *MDPI*. doi: 10.3390/ijerph17051509.

[50] M. E. Seeley, B. Song, R. Passie, and R. C. Hale, "Microplastics affect sedimentary microbial communities and nitrogen cycling," *Nat Commun*, vol. 11, no. 1, Dec. 2020, doi: 10.1038/s41467-020-16235-3.

[51] M. P. de Almeida *et al.*, "The prevalence of microplastics on the earth and resulting increased imbalances in biogeochemical cycling," *Water Emerging Contaminants & Nanoplastics*, vol. 2, no. 2, p. 7, 2023, doi: 10.20517/wecn.2022.20.

[52] A. Kumar and G. Krishan, "Microplastic Pollutants in Aquatic Ecosystems: Present and Future Challenges," Jan. 01, 2024, *Multidisciplinary Digital Publishing Institute (MDPI)*. doi: 10.3390/w16010102.

[53] J. DA Pinto Costa, T. Rocha-santos, A. C. Duarte, D. of Chemistry, and U. of Aveiro, "The environmental impacts of plastics and micro-plastics use, waste and pollution: EU and national measures Policy Department for Citizens' Rights and Constitutional Affairs Directorate-General for Internal Policies PE."

[54] S. Coffin, H. Wyer, and J. C. Leapman, "Addressing the environmental and health impacts of microplastics requires open collaboration between diverse sectors," Mar. 30, 2021, *Public Library of Science*. doi: 10.1371/JOURNAL.PBIO.3000932.

[55] V. Jani, S. Wu, and K. Venkiteshwaran, "Advancements and Regulatory Situation in Microplastics Removal from Wastewater and Drinking Water: A Comprehensive Review," *Microplastics*, vol. 3, no. 1, pp. 98–123, Feb. 2024, doi: 10.3390/microplastics3010007.

[56] S. Damaj, F. Trad, D. Goevert, and J. Wilkesmann, "Bridging the Gaps between Microplastics and Human Health," *Microplastics*, vol. 3, no. 1, pp. 46–66, Jan. 2024, doi: 10.3390/microplastics3010004.

[57] Y. Li, L. Tao, Q. Wang, F. Wang, G. Li, and M. Song, "Potential Health Impact of Microplastics: A Review of Environmental Distribution, Human Exposure, and Toxic Effects," Oct. 20, 2023, *American Chemical Society*. doi: 10.1021/envhealth.3c00052.

[58] K. D. Cox, G. A. Covernton, H. L. Davies, J. F. Dower, F. Juanes, and S. E. Dudas, "Human Consumption of Microplastics," *Environ Sci Technol*, vol. 53, no. 12, pp. 7068–7074, Jun. 2019, doi: 10.1021/acs.est.9b01517.

[59] E. Curren, C. P. Leaw, P. T. Lim, and S. C. Y. Leong, "Evidence of Marine Microplastics in Commercially Harvested Seafood," *Front Bioeng Biotechnol*, vol. 8, Dec. 2020, doi: 10.3389/fbioe.2020.562760.

[60] M. Smith, D. C. Love, C. M. Rochman, and R. A. Neff, "Microplastics in Seafood and the Implications for Human Health," Sep. 01, 2018, *Springer*. doi: 10.1007/s40572-018-0206-z.

[61] M. Myszograj, "Microplastic in Food and Drinking Water - Environmental Monitoring Data," *Civil and Environmental Engineering Reports*, vol. 30, no. 4, pp. 201–209, Dec. 2020, doi: 10.2478/ceer-2020-0060.

[62] A. Tamargo *et al.*, "PET microplastics affect human gut microbiota communities during simulated gastrointestinal digestion, first evidence of plausible polymer biodegradation during human digestion," *Sci Rep*, vol. 12, no. 1, Dec. 2022, doi: 10.1038/s41598-021-04489-w.

[63] A. W. Verla, C. E. Enyoh, E. N. Verla, and K. O. Nwarnorh, "Microplastic–toxic chemical interaction: a review study on quantified levels, mechanism and implication," Nov. 01, 2019, *Springer Nature*. doi: 10.1007/s42452-019-1352-0.

[64] M. Borgatta and F. Breider, "Inhalation of Microplastics—A Toxicological Complexity," *Toxics*, vol. 12, no. 5, May 2024, doi: 10.3390/toxics12050358.

[65] T. Eberhard, G. Casillas, G. M. Zarus, and D. B. Barr, "Systematic review of microplastics and nanoplastics in indoor and outdoor air: identifying a framework and data needs for quantifying human inhalation exposures," Mar. 01, 2024, *Springer Nature*. doi: 10.1038/s41370-023-00634-x.

[66] K. Lu *et al.*, "Microplastics, potential threat to patients with lung diseases," 2022, *Frontiers Media S.A.* doi: 10.3389/ftox.2022.958414.

[67] C. Baeza-Martínez, E. Garcia-Pachon, and J. Bayo, "Environmental Microplastics and the Lung," Jun. 01, 2023, *Sociedad Espanola de Neumologia y Cirugia Toracica (SEPAR)*. doi: 10.1016/j.arbres.2022.09.019.

[68] G. F. Vasse and B. N. Melgert, "Microplastic and plastic pollution: impact on respiratory disease and health," *European Respiratory Review*, vol. 33, no. 172, Apr. 2024, doi: 10.1183/16000617.0226-2023.

[69] S. M. Bashir, S. Kimiko, C. W. Mak, J. K. H. Fang, and D. Gonçalves, "Personal Care and Cosmetic Products as a Potential Source of Environmental Contamination by Microplastics in a Densely Populated Asian City," *Front Mar Sci*, vol. 8, Jun. 2021, doi: 10.3389/fmars.2021.683482.

[70] L. Deng, G. Li, S. Peng, J. Wu, and Y. Che, "Microplastics in personal care products: Exploring public intention of usage by extending the theory of planned behaviour," *Science of the Total Environment*, vol. 848, Nov. 2022, doi: 10.1016/j.scitotenv.2022.157782.

[71] E. Vassilenko *et al.*, "Domestic laundry and microfiber pollution: Exploring fiber shedding from consumer apparel textiles," *PLoS One*, vol. 16, no. 7 July, Jul. 2021, doi: 10.1371/journal.pone.0250346.

[72] B. M. Carney Almroth, L. Åström, S. Roslund, H. Petersson, M. Johansson, and N. K. Persson, "Quantifying shedding of synthetic fibers from textiles; a source of microplastics released into the environment," *Environmental Science and Pollution Research*, vol. 25, no. 2, pp. 1191–1199, Jan. 2018, doi: 10.1007/s11356-017-0528-7.

[73] H. Samuel, F.-D. Makong, and M. Ori, "Green Chemistry Strategies for Mitigating Microplastic Pollution in Aquatic Environments," *Asian Journal of Environmental Research*, vol. 1, no. 2, pp. 73–82, Jul. 2024, doi: 10.69930/ajer.v1i2.67.

[74] S. Mariano, S. Tacconi, M. Fidaleo, M. Rossi, and L. Dini, "Micro and Nanoplastics Identification: Classic Methods and Innovative Detection Techniques," 2021, *Frontiers Media S.A.* doi: 10.3389/ftox.2021.636640.

[75] K. Duis and A. Coors, "Microplastics in the aquatic and terrestrial environment: sources (with a specific focus on personal care products), fate and effects," Dec. 01, 2016, *Springer Verlag*. doi: 10.1186/s12302-015-0069-y.

[76] S. Adhikari, V. Kelkar, R. Kumar, and R. U. Halden, "Methods and challenges in the detection of microplastics and nanoplastics: a mini-review," May 01, 2022, *John Wiley and Sons Ltd*. doi: 10.1002/pi.6348.

[77] R. K. Gangwar *et al.*, "Optical fiber SERS sensors: Unveiling advances, challenges, and applications in a miniaturized technology," Jul. 01, 2024, *Elsevier B.V.* doi: 10.1016/j.ccr.2024.215861.

[78] M. Willans *et al.*, "Development of a rapid detection protocol for microplastics using reflectance-FTIR spectroscopic imaging and multivariate classification," *Environmental Science: Advances*, vol. 2, no. 4, pp. 663–674, Mar. 2023, doi: 10.1039/d2va00313a.

[79] A. S. Tagg, M. Sapp, J. P. Harrison, and J. J. Ojeda, "Identification and Quantification of Microplastics in Wastewater Using Focal Plane Array-Based Reflectance Micro-FT-IR Imaging," *Anal Chem*, vol. 87, no. 12, pp. 6032–6040, Jun. 2015, doi: 10.1021/acs.analchem.5b00495.

[80] J. Zhou, H. Xu, Y. Xiang, and J. Wu, "Effects of microplastics pollution on plant and soil phosphorus: A meta-analysis," *J Hazard Mater*, vol. 461, Jan. 2024, doi: 10.1016/j.jhazmat.2023.132705.

[81] T. Fisher Scientific, "Guide to the identification of microplastics by FTIR and Raman spectroscopy."

[82] V. Nava, M. L. Frezzotti, and B. Leoni, "Raman Spectroscopy for the Analysis of Microplastics in Aquatic Systems," Nov. 01, 2021, *SAGE Publications Inc.* doi: 10.1177/00037028211043119.

[83] A. M. Othman, A. A. Elsayed, Y. M. Sabry, D. Khalil, and T. Bourouina, "Detection of Sub-20 μm Microplastic Particles by Attenuated Total Reflection Fourier Transform Infrared Spectroscopy and Comparison with Raman Spectroscopy," *ACS Omega*, vol. 8, no. 11, pp. 10335–10341, Mar. 2023, doi: 10.1021/acsomega.2c07998.

[84] D. Dong and C. Zhao, "Limitations and challenges of using raman spectroscopy to detect the abiotic plant stress response," Jul. 11, 2017, *National Academy of Sciences*. doi: 10.1073/pnas.1707408114.

[85] T. Fisher Scientific, "Guide to the identification of microplastics by FTIR and Raman spectroscopy."

[86] S. T. Anuar *et al.*, "Utilizing Pyrolysis–Gas Chromatography/Mass Spectrometry for Monitoring and Analytical Characterization of Microplastics in Polychaete Worms," *Polymers (Basel)*, vol. 14, no. 15, Aug. 2022, doi: 10.3390/polym14153054.

[87] M. E. Seeley and J. M. Lynch, "Previous successes and untapped potential of pyrolysis–GC/MS for the analysis of plastic pollution," Jun. 01, 2023, *Springer Science and Business Media Deutschland GmbH*. doi: 10.1007/s00216-023-04671-1.

[88] S. Primpke, C. Lorenz, R. Rascher-Friesenhausen, and G. Gerdts, "An automated approach for microplastics analysis using focal plane array (FPA) FTIR microscopy and image analysis," *Analytical Methods*, vol. 9, no. 9, pp. 1499–1511, Mar. 2017, doi: 10.1039/c6ay02476a.

[89] Z. Yang, H. Nagashima, and H. Arakawa, "Development of automated microplastic identification workflow for Raman micro-imaging and evaluation of the uncertainties during micro-imaging," *Mar Pollut Bull*, vol. 193, Aug. 2023, doi: 10.1016/j.marpolbul.2023.115200.

[90] K. M. DeAngelis *et al.*, "PCR amplification-independent methods for detection of microbial communities by the high-density microarray PhyloChip," *Appl Environ Microbiol*, vol. 77, no. 18, pp. 6313–6322, Sep. 2011, doi: 10.1128/AEM.05262-11.

[91] J. J. Ojeda, "Advantages and limitations of spectroscopic and microscopic approaches for the characterisation of microplastics."

[92] A. A. Elsayed *et al.*, "A microfluidic chip enables fast analysis of water microplastics by optical spectroscopy," *Sci Rep*, vol. 11, no. 1, Dec. 2021, doi: 10.1038/s41598-021-89960-4.

[93] Jia-Sheng Hong; M. J. Lancaster, *Microstrip Filters for RF/Microwave Applications*, vol. 1. John Wiley & Sons, Inc, 2001.

[94] "Lecture 11 Transmission Lines."

[95] A. Rashid, O. Hasan, E. Deniz, S. Tahar, and T. Deniz, "Formalization of the Telegrapher's Equations using Higher-Order-Logic Theorem Proving," 2024. [Online]. Available: https://www.researchgate.net/publication/379913006

[96] "Lecture_12_Transmission line theory".

[97] J. D. ' Ambrosia, T. Electronics, and A. Healey, "EuroDesignCon 2005 Backplane Channels and Correlation Between Their Frequency and Time Domain Performance."

[98] S. Arslanagić *et al.*, "A review of the scattering parameter extraction method with clarification of ambiguity issues in relation to metamaterial homogenization."

[99] L. Zhong, R. Yu, and X. Hong, "Review of carbon-based electromagnetic shielding materials: film, composite, foam, textile," May 01, 2021, *SAGE Publications Ltd*. doi: 10.1177/0040517520968282.

[100] J. D. Jackson, *Classical Electrodynamics*. USA: Wiley, 1989.

[101] "Paper II Electromagnetic".

[102] Z. Sun, C. Ma, C. Yu, and Z. Li, "Microplastic separation and enrichment in microchannels under derivative electric field gradient by bipolar electrode reactions," *Sci Rep*, vol. 14, no. 1, Dec. 2024, doi: 10.1038/s41598-024-54921-0.

[103] Y. Li, Y. Zhu, J. Huang, Y. W. Ho, J. K. H. Fang, and E. Y. Lam, "High-throughput microplastic assessment using polarization holographic imaging," *Sci Rep*, vol. 14, no. 1, Dec. 2024, doi: 10.1038/s41598-024-52762-5.

[104] B. C. Colson and A. P. M. Michel, "Flow-Through Quantification of Microplastics Using Impedance Spectroscopy," *ACS Sens*, vol. 6, no. 1, pp. 238–244, Jan. 2021, doi: 10.1021/acssensors.0c02223.

[105] Martin Chaplin, "Water Dielectric and Microwave Radiation," https://sites.science.oregonstate.edu/~hetheriw/astro/rt/info/water/water_dielectric_function_and_microwave_radiation.html.
[106] S. Kumar, D. Shri, S. Baba, and A. M. Ambikapur, "The effect of dielectric constant's on water properties and applications : A comprehensive review 1 2* 3." [Online]. Available: https://www.researchgate.net/publication/379019400
[107] D. M. Pozar, *Microwave engineering*. John Wiley & Sons, 2009.
[108] "PHOTOLITHOGRAPHY OVERVIEW FOR MICROSYSTEMS Photolithography Overview Learning Module Patterned Mask for Photolithography Expose."
[109] J. Im, T. Goo, J. Kim, S. Choi, S. J. Hong, and Y. M. Bahk, "Detection of microplastic in salts using terahertz time-domain spectroscopy," *Sensors*, vol. 21, no. 9, May 2021, doi: 10.3390/s21093161.
[110] G. Gugliandolo, A. Quattrocchi, M. Latino, D. Aloisio, G. Crupi, and N. Donato, "Microplastic identification in marine environments: A low-cost and effective approach based on transmitted light measurements," *Acta IMEKO*, vol. 13, no. 2, 2024, doi: 10.21014/actaimeko.v13i2.1745.
[111] Z. Chen, X. Kan, Q. Yuan, T. Wang, J. Yang, and F. Yang, "A Switchable High-Performance RF-MEMS Resonator with Flexible Frequency Generations," *Sci Rep*, vol. 10, no. 1, Dec. 2020, doi: 10.1038/s41598-020-61744-2.
[112] A. R. H. Goodwin, J. B. Mehl, and M. R. Moldover, "Reentrant radio-frequency resonator for automated phase-equilibria and dielectric measurements in fluids." [Online]. Available: http://ojps.aip.org/rsio/rsicr.jsp
[113] EverythingRF, "Microstrip Impedance Calculator," https://www.everythingrf.com/rf-calculators/microstrip-impedance-calculator.
[114] R. E. Rachmanita *et al.*, "The high capacitance for electrode structure of interdigital capacitor thin film models."
[115] B. R. S, A. M. Khan, and M. H. Reddy V, "DESIGN AND OPTIMIZATION OF INTERDIGITAL CAPACITOR." [Online]. Available: https://www.esatjournals.org/ijret
[116] A. Awada *et al.*, "Facile detection of microplastics from a variety of environmental samples with conjugated polymer nanoparticles," *Environmental Science: Advances*, 2024, doi: 10.1039/d4va00239c.
[117] C. Yang, J. Xie, A. Gowen, and J. L. Xu, "Machine learning driven methodology for enhanced nylon microplastic detection and characterization," *Sci Rep*, vol. 14, no. 1, Dec. 2024, doi: 10.1038/s41598-024-54003-1.
[118] B. C. Colson and A. P. M. Michel, "Flow-Through Quantification of Microplastics Using Impedance Spectroscopy," *ACS Sens*, vol. 6, no. 1, pp. 238–244, Jan. 2021, doi: 10.1021/acssensors.0c02223.
[119] Y. Li *et al.*, "Microplastics in Water: A Review of Characterization and Removal Methods," May 01, 2024, *Multidisciplinary Digital Publishing Institute (MDPI)*. doi: 10.3390/su16104033.
[120] A. A. de Souza Machado, W. Kloas, C. Zarfl, S. Hempel, and M. C. Rillig, "Microplastics as an emerging threat to terrestrial ecosystems," Apr. 01, 2018, *Blackwell Publishing Ltd*. doi: 10.1111/gcb.14020.
[121] R. Corporation, "RT/duroid ® 5870 /5880 High Frequency Laminates Some Typical Applications: • Commercial Airline Broadband Antennas • Microstrip and Stripline Circuits • Millimeter Wave Applications • Military Radar Systems • Missile Guidance Systems • Point to Point Digital Radio Antennas," 2022.
[122] P. Kakria, A. Marwaha, M. S. Manna, M. Tech, and R. Scholar, "Optimized Design of Shielded Microstrip Lines Using Adaptive Finite Element Method."
[123] "Microstrip, Stripline, and CPW Design." [Online]. Available: http://www.qsl.net/va3iul
[124] "Microwave_Engineering_David_M_Pozar_4ed_Wiley_2012".

APENDIX

The identification of microplastics in environmental samples demands sophisticated and precise analytical techniques. As a result, the detection and characterization of microplastics have become crucial research areas in understanding their distribution, impact, and potential mitigation strategies[116][117]. Researchers and scientists have turned to innovative material characterization technologies, such as stripline, microstrip, coplanar waveguide, and slot line transmission methods, to study microplastics' electrical properties and interactions[118], [119]. By exploring the electrical characteristics, permittivity, and empirical formulas associated with these technologies, it is possible to make informed decisions about selecting the most suitable method for detecting and quantifying microplastics in various environmental matrices [118]. This research delves into the comparative analysis of these transmission line technologies for material characterization, emphasizing their critical electrical characteristics, permittivity behavior, and empirical formulas. By examining their applicability and sensitivity to microplastics' presence, this study aims to provide valuable insights into choosing the optimal technology for ongoing research in microplastic detection and its implications for environmental conservation efforts. Understanding and tackling the microplastic issue are critical steps towards preserving ecosystems and safeguarding the health of both the environment and human populations[120]

Microwave circuit technologies are integral to diverse applications like telecommunications, radar systems, wireless communication, and satellite communication. Efficient and high-performance circuit design relies on understanding the electrical characteristics unique to each technology[121]. Key electrical characteristics, such as characteristic impedance (Z_0), attenuation factor, and signal propagation speed (v), are crucial in high-frequency circuit designs. The values of (Z_0) and (v) are affected by the effective relative permittivity (ϵ_r), while signal losses are influenced by α_c. This study aims to analyze and compare the electrical characteristics of four prominent microwave circuit technologies: stripline, microstrip, coplanar waveguide (CPW), and slot line. Each of these technologies has

its own advantages and limitations in terms of performance, ease of manufacturing, and application suitability.

By comparing these technologies, the study will provide insights into the most appropriate choice for specific microwave circuit applications based on their electrical characteristics, including (Z_0), (v), (ε_r), and (α_c). This analysis will help optimize microwave circuit designs for various applications, balancing performance, cost, and manufacturability.

The following parameters will be employed in this section to calculate the characteristic impedance (Z_0), the conductor loss factor (α_c), and the effective relative permittivity ($\varepsilon_{r,\text{eff}}$) of the transmission lines. These key parameters are applicable to the various transmission line structures discussed, by definition, they are:

- (Z_0): The characteristic impedance of the transmission line, which determines the relationship between voltage and current in the line. It is crucial for matching the impedance of the source and load to minimize reflections and maximize power transfer.

- (α_c): The conductor loss factor, which quantifies the energy loss due to the resistance of the conductors in the transmission line. This factor influences the attenuation of the signal as it propagates through the line, and higher conductor losses can degrade signal quality.

- ($\varepsilon_{r,\text{eff}}$): The effective relative permittivity of the transmission line, which affects the speed of signal propagation (v) and the characteristic impedance (Z_0). The effective permittivity takes into account both the dielectric material and the structure of the transmission line, providing a more accurate representation of how electromagnetic waves travel through the medium.

STRIPLINE

Stripline circuits are designed with a conducting strip placed between two parallel ground planes, typically on a dielectric substrate The electrical properties of stripline circuits encompass several key aspects. Firstly, they exhibit lower propagation delay compared to microstrip circuits, primarily due to the signal line's closer proximity to the ground planes. This closeness helps in reducing signal travel time. Another significant advantage of stripline circuits is their excellent control over characteristic impedance[122], [123]. This precise control enables accurate impedance matching and minimizes signal reflection, leading 7 to

improved signal integrity and performance. When analysing Stripline transmission lines, researchers commonly use two sets of equations to calculate the characteristic impedance (Z0) and the attenuation (αc).

Figure A 1 - Ilustrated Microstrip Line and its Cross-Sectional view without metal cover

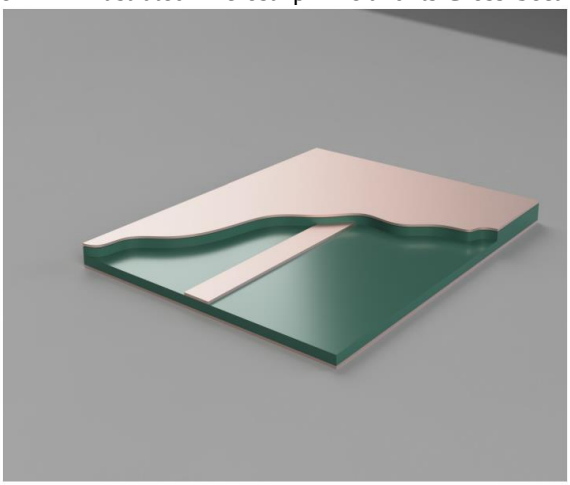

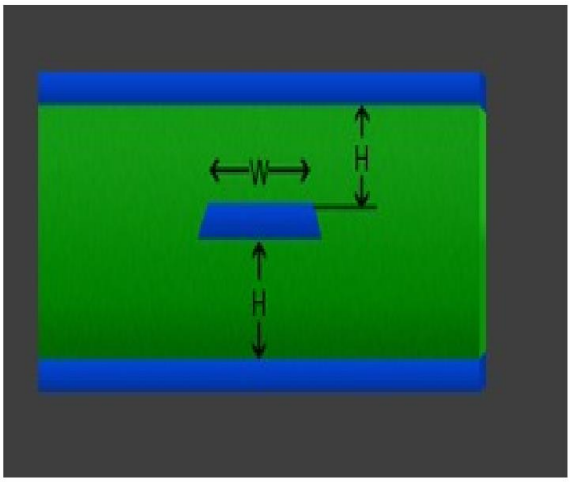

The choice of equations depends on whether the transmission line is considered narrow or wide. Specifically, the equation relies on the ratio between the width of the signal line (w) and the difference between the dielectric and conductor thickness (b-t), where the spacing between the ground planes (b) plays a crucial role Figure. 01 a. In summary, Stripline circuits offer advantages such as lower propagation delay and excellent impedance control (b11). The design and analysis of Stripline transmission lines involve specific equations dependent on the line's width and ground plane spacing, allowing for precise characterization and utilization in various applications as in[115], [123][124].

$$\epsilon_{\mathrm{r,eff}} = \frac{\mathrm{C}}{\mathrm{C}_0} \quad \text{A. 1}$$

$$\mathrm{Z}_0 = \frac{1}{\mathrm{cv}_{\mathrm{ph}}} \quad \text{A. 2}$$

$$\mathrm{cv}_{\mathrm{ph}} = \frac{V_0}{\sqrt{\epsilon_{\mathrm{r,eff}}}} \quad \text{A. 3}$$

$$C = C_0 + C_1 + C_2 + C_3 \quad \text{A. 4}$$

$$C_0 = C_{01} + C_{02} \quad \text{A. 5}$$

$$C_{01} = \frac{\epsilon_0 K(k_2')}{2\mathrm{K}(k_2)} \quad \text{A. 6}$$

$$C_{02} = \frac{\epsilon_0 K(k_3')}{2\mathrm{K}(k_3)} \quad \text{A. 7}$$

$$C_1 = \frac{\epsilon_0(\epsilon_r - 1)K(k_2')}{2\mathrm{K}(k_2)} \quad \text{A. 8}$$

$$C_2 = \frac{\epsilon_0(\epsilon_{r3}-1)K(k_3')}{2\mathrm{K}(k_3)} \quad \text{A. 9}$$

$$C_3 = \frac{\epsilon_0(\epsilon_{r2}-\epsilon_{r3})K(k_{34}')}{2\mathrm{K}(k_4)} \quad \text{A. 10}$$

$$k_2 = \frac{S_t W_t}{2W_{1t}W_{2t}+S_t W_t+2\sqrt{W_{1t}^2 W_{2t}^2 S_t W_{1t} W_{1t} W_t}} \quad \text{A. 11}$$

$$k_2' = \sqrt{1-\ k_2^2} \quad \text{A. 12}$$

$$S_t = B_3\ -\ B_2 \quad \text{A. 13}$$

$$W_{1t} =\ B_2 -\ B_1 \quad \text{A. 14}$$

$$W_{2t} = B_4 - B_3 \quad \text{A. 15}$$

$$W_t = W_{1t} + W_{2t} + S_t \quad \text{A. 16}$$

This case was tasted for: $W_{1t} =\ 0.6,\ W_{2t} =\ 0.3,\ S_t =\ 0.1$

$$C_1 = \frac{\epsilon_0(\epsilon_{r1}-1)K(k_2')}{K(k_2')^2 K(k_2)} = \frac{\epsilon_0(\epsilon_{r1}-\epsilon_2)K(k_2')}{K(k_2')^2 K(k_2)} = \frac{\epsilon_0\left(\epsilon_{r1}-\frac{v_p}{v_T}\right)\epsilon_{\mathrm{p}}^{\gamma}+\left(1-\frac{v_p}{v_T}\right)\epsilon_{\mathrm{w}}^{\gamma}K(k_2')}{K(k_2')^2 K(k_2)} \quad \text{A. 17}$$

$$\epsilon_2 = \frac{v_p}{v_T}\epsilon_{\mathrm{p}}^{\gamma} + \left(1-\frac{v_p}{v_T}\right)\epsilon_{\mathrm{w}}^{\gamma} \quad \text{A. 18}$$

$$\frac{\mathrm{K}(k_2)}{K(k_2')} = \frac{W}{2\mathrm{h}} \quad \text{A. 19}$$

Again, by substituting the equations recursively, the final value of the permittivity is obtained:

$$\epsilon_{\mathrm{r,eff}} = \frac{C_0+C_1+C_2+C_3}{\mathrm{C}_0} \quad \text{A. 20}$$

and its derivative is given by:

$$\left|\frac{\partial(\epsilon_{r,eff})}{\partial v}\right| = \frac{4\pi r^2}{\gamma\epsilon_{\mathrm{r1}}^{\gamma-1}v_t}\left(\epsilon_{\mathrm{p}}^{\gamma}-\epsilon_{\mathrm{w}}^{\gamma}\right)dr \quad \text{A. 21}$$

Figure A 2 - Effective permittivity in (a) and its derivative in (b) vs variation of the raduis of the plastic volume. Note that the values are really outlined but the expected tandance holds

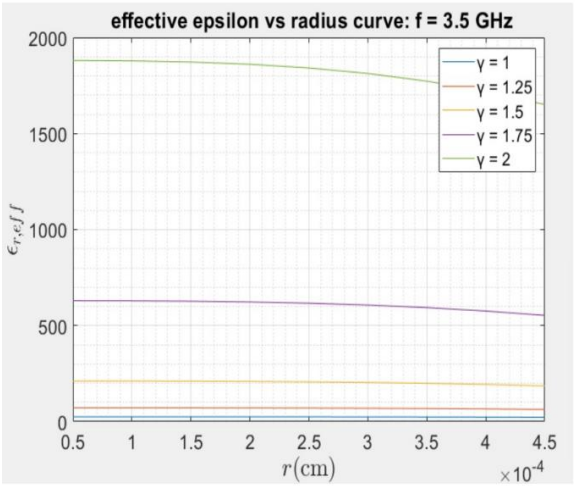

(a)

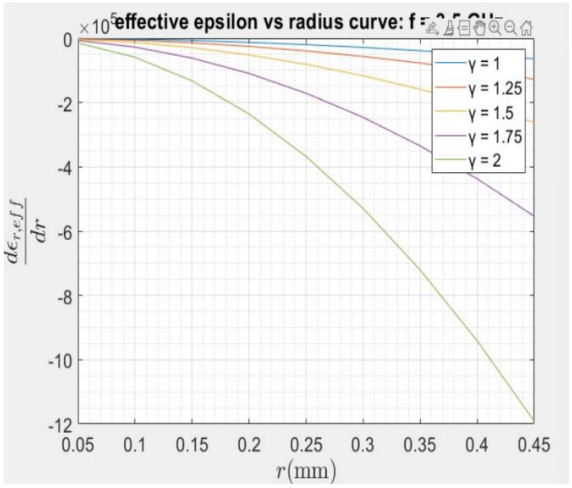

(b)

COPLANAR WAVEGUIDE (CPW)

Is widely used microwave circuit technology, featuring a conducting strip positioned between two ground planes with gaps on each side. This design offers excellent isolation, low signal losses, and compatibility with integrated circuits. Compared to microstrip CPW provides a broader bandwidth but entails higher fabrication complexity and costs[123], [124]. The characteristic impedance of CPW is determined by the conductor width, the gap between the conductor and ground planes, and the dielectric constant of the substrat.

Figure A 3 - Effective permittivity in (a) and its derivative in (b) vs variation of the raduis of the plastic volume. Note that the values are really outline but the expected tandance holds

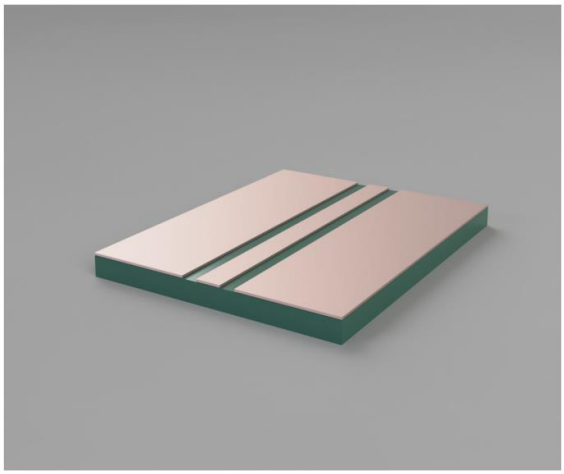

(a)

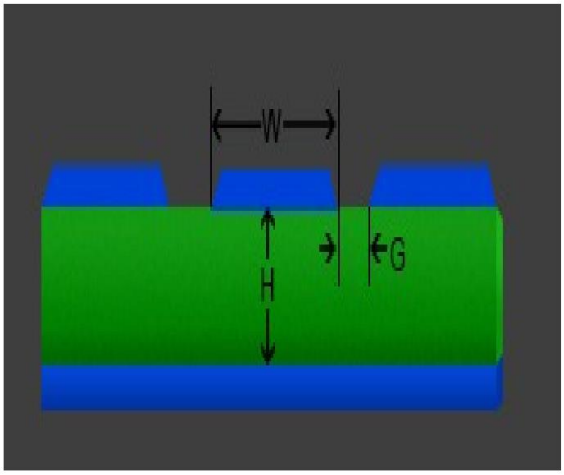

(b)

Regarding the electrical characteristics of CPW, let's consider two scenarios for the capacitance C per unit length. Firstly, when the dielectric substrate is replaced with air (i.e., εr = 1), the capacitance per unit length can be expressed as one-fourth of the conductor width. Secondly, when the electromagnetic field is confined within a dielectric substrate with a relative permittivity of εr (εr - 1 scenario) the capacitance per unit length is approximately given by r divided by four times the conductor width [122], [123], [124].

$$\epsilon_{r,eff} = 1 + \frac{C}{C_0}, \qquad \text{A. 22}$$

with, $C = C_0 + C_1$. As previously

$$C_0 = C_{01} + C_{02} \qquad \text{A. 23}$$

The configuration of C_{01} is the CPW with a finite ground conductor and upper half-plane air region. Thus, using the conformal mapping method, it´s can be found that:

Figure A 4 - Configurations of capacitances (a) C_01 and (b) C_02.

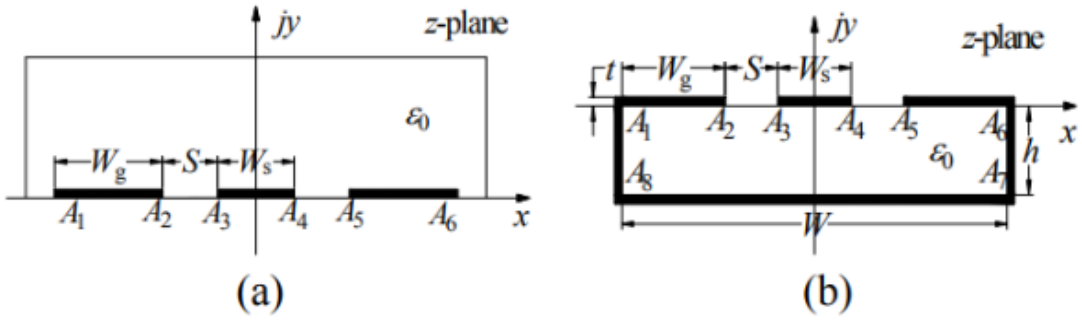

Figure A 5 - Configurations of capacitances C_{02} in t-plane.

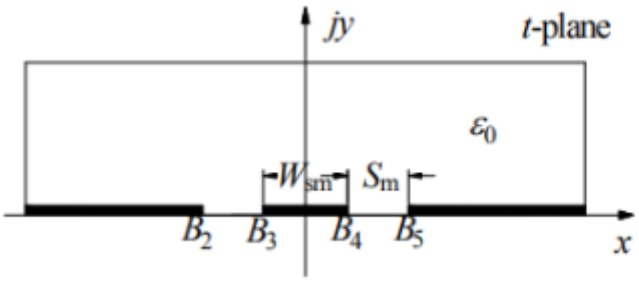

$$C_{01} = \frac{\epsilon_0 K(k_1')}{K(k_1)} \qquad \text{A. 24}$$

$$C_{02} = \frac{2\epsilon_0 K(k_3')}{K(k_3)} \qquad \text{A. 25}$$

Note that: The difference between configurations of C_{02} and C_1 is only the permittivity. In the configuration of C_1, the relative permittivity is ε_r - 1. Thus, the capacitance C_1 can be derived as in [123]:

$$C_1 = \frac{2(\epsilon_r - 1)\mathrm{K}(k_3)}{K(k_3')} \quad \text{A. 26}$$

K is the complete elliptical integral of the first kind. The modulus can be expressed as:

$$k_1 = \frac{S_t W_t}{2W_{gt}W_{st} + S_t W_t + 2\sqrt{W_{gt}^2 W_{2t}^2 S_t W_{gt} W_{st} W_t}} \quad \text{A. 27}$$

$$k_3 = \frac{W_{sm}}{W_{sm} + 2S_m} \quad \text{A. 28}$$

Where $S_t = S^2 + SW_s$

$$W_{gt} = W_g^2 + W_S W_g + 2SW_g \quad \text{A. 29}$$

$$W_{st} = \frac{W_s^2}{4} \quad \text{A. 30}$$

$$W_t = W_{st} + W_{gt} + S_t \quad \text{A. 31}$$

$$k_1' = \sqrt{1 - k_1^2} \quad \text{A. 32}$$

$$W_{sm} = 2S_m \left(\frac{K(k_2)W_s}{W}, k_2\right) \quad \text{A. 33}$$

$$S_m = \left(\frac{K(k_2)(W_s + 2S)}{W}, k_2\right) - \left(\frac{K(k_2)W_s}{W}, k_2\right) \quad \text{A. 34}$$

The approximate expressions of modulus k_2 can be expressed as in [15]

$$1 \le \frac{W}{2h} \le \infty \rightarrow k_2 = \left(\frac{\pi e^{\frac{W}{2h}} - 2}{\pi e^{\frac{W}{2h}} + 2}\right)^2 \quad \text{A. 35}$$

$$0 \le \frac{W}{2h} \le 1 \rightarrow k_2 = \sqrt{1 - \left(\frac{\pi e^{\frac{W}{2h}} - 2}{\pi e^{\frac{W}{2h}} + 2}\right)^4} \quad \text{A. 36}$$

Now with the value of C0 and C1 It's easy to calculate the relative effective permittivity $\varepsilon_{r,eff}$ and characteristic impedance Z_0 equation[x] of the system as in [13-16] respectively.

$$\epsilon_{r,eff} = \frac{\mathrm{C}}{\mathrm{C}_0} = 1 + \frac{\mathrm{C}_1}{\mathrm{C}_0} \quad \text{A. 37}$$

For multilayers, as in microstrip $\epsilon_r - 1$ turns into $\epsilon_{r1} - \epsilon_{r2}$. By substituting the equations recursively, the final value of the permittivity is obtained as:

$$\epsilon_{r,eff} = 1 + \frac{(\epsilon_{r1} - \epsilon_{r2})}{\epsilon_0} \quad \text{A. 38}$$

Using the equation $\epsilon_2 = \epsilon_{r2}^{\gamma}$, the effective permittivity becomes as folliwing.

$$\epsilon_{r,eff} = 1 + \frac{\left(\epsilon_{r1} - \left(\frac{v_p}{v_T}\epsilon_p^{\gamma} + \left(1 - \frac{v_p}{v_T}\right)\epsilon_w^{\gamma}\right)\right)}{\epsilon_0} \quad \text{A. 39}$$

To analyze the impact of changes in the radius of the spherical plastic on the effective permittivity, we assume that both (ϵ_1) and r_1 are constants. Therefore, their derivatives with respect to the radius are zero. The effective permittivity ϵ_{eff} is a function of the radius of the spherical microplastic particles. By computing the derivative of ϵ_{eff} with respect to the radius r we can determine how the effective permittivity changes as the size of the plastic particles varies.

This derivative will provide insights into how sensitive the permittivity is to particle size, which is essential for optimizing detection techniques. The relationship can be expressed from [124] as:

$$\frac{\partial \epsilon_{\mathrm{r,eff}}}{\partial r} = \frac{d}{dr}\left(1 + \frac{\left(\epsilon_{\mathrm{r1}} - \left(\frac{v_p}{v_T}\epsilon_{\mathrm{p}}^{\gamma} + \left(1 - \frac{v_p}{v_T}\right)\epsilon_{\mathrm{w}}^{\gamma}\right)\right)}{\epsilon_0}\right) \qquad \text{A. 40}$$

This approach allows us to evaluate the impact of particle size on the overall. electromagnetic properties of the system, which is critical in refining the detection accuracy of microplastics in the medium. Using the same value for C_0 as [124] them the derivative of the Effective Permittivity is given as:

$$\left|\frac{\partial(\epsilon_{r,eff})}{\partial v}\right| = -\frac{1}{\epsilon_0}\left(\frac{4\pi r^2}{\gamma \epsilon_{\mathrm{r1}}^{\gamma-1} v_t}\left(\epsilon_{\mathrm{p}}^{\gamma} - \epsilon_{\mathrm{w}}^{\gamma}\right)dr\right) \qquad \text{A. 41}$$

Figure A 6 - (a) illustrates the effective permittivity as a function of frequency, showing that it remains constant. Figure (b) depicts the relationship between the derivative of the effective permittivity and the radius of the plastic sphere.

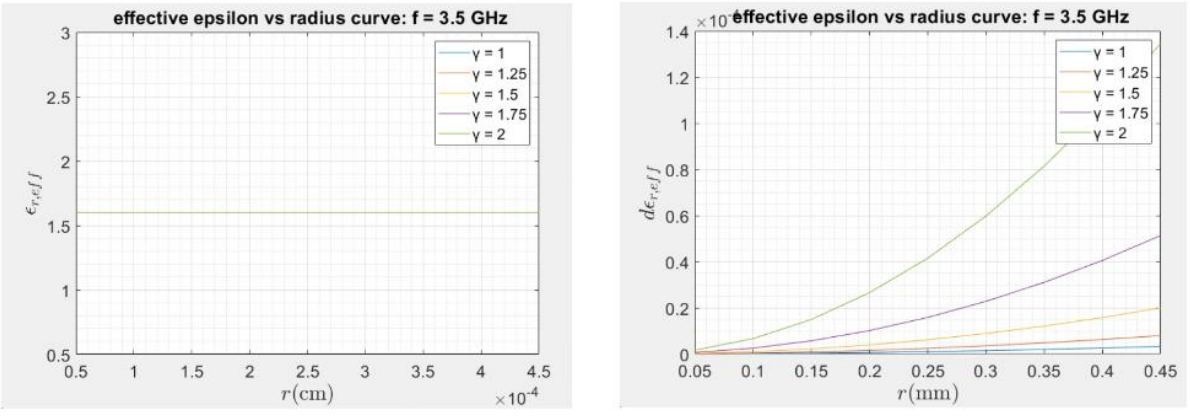

Figura 2.4 – Effective permittivity in (a) and its derivative in (b) vs variation of the radius of the plastic volume. Note that the values are really outlined but the expected tendence holds

- ***Impedance Control:*** In impedance control, coplanar waveguide (CPW) circuits offer precise control over the characteristic impedance (Z_0), which is crucial for achieving impedance matching and efficient signal transmission. The characteristic impedance for a CPW is typically given by the equation:

$$Z_0 = \frac{\sqrt{\epsilon_{r,eff}}}{C v_0} \quad \text{A. 42}$$

Where (Z_0) is the characteristic impedance, ($\epsilon_{r,eff}$) is the effective relative permittivity of the transmission line, (C) represents the capacitance per unit length of the transmission line and (v_0) is the speed of light in a vacuum.

This equation highlights the relationship between the effective permittivity and the characteristic impedance, with (Z_0) being inversely proportional to ($\epsilon_{r,eff}$). Efficient control of ($\epsilon_{r,eff}$) through proper circuit design leads to better impedance matching, minimizing signal reflections and ensuring optimal signal transmission across the circuit.

SLOT LINE

Slot line is a type of transmission line technology widely used in microwave and RF circuits. It consists of a narrow slot or gap in a conductive ground plane, with a strip line positioned above the slot on a dielectric substrate. This structure allows precise control over the electric field concentrated within the slot, making the design highly sensitive to variations in material properties or the presence of contaminants, as shown in Figure 2.7 Slot line transmission lines are known for their low-loss characteristics and the ability to handle high power, making them suitable for applications in microwave filters, couplers, and other high-frequency components[123].

However, compared to other technologies like microstrip or stripline, slot lines can be more complex to fabricate. The electrical properties of a slot line, including its characteristic impedance (Z_0), propagation constant (β), and signal propagation speed (v), are key parameters for designing and optimizing circuits for specific microwave applications. A clear understanding of these characteristics is essential for achieving efficient, high-performance microwave circuit designs[122].

ASYMMETRIC STRIPLINE:

Asymmetric stripline is another type of transmission line used in high-frequency and microwave circuit designs. It consists of a dielectric layer sandwiched between two conductive planes, but unlike conventional stripline, the conductive planes are of unequal width, giving rise to its "asymmetric" designation.

In this configuration, the wider conductive plane serves as the signal trace, while the narrower one acts as the ground plane. The dielectric layer between them provides insulation and mechanical support. The unequal width of the planes results in different characteristic impedance for the signal trace compared to symmetrical striplines. Key factors influencing the characteristic impedance include the dimensions of the conductive planes, the thickness of the dielectric layer, and the dielectric constant of the material.

Asymmetric striplines offer certain advantages in RF and microwave circuits, such as improved electromagnetic interference (EMI) reduction due to the presence of a well-shielded ground plane. Additionally, the asymmetry enables finer control over the impedance, which is crucial for impedance matching and transformation in high-frequency circuits.

However, the design and analysis of asymmetric striplines require careful consideration of the material properties, geometry, and dimensions of the structure to ensure proper impedance matching and signal integrity. Achieving optimal performance in these circuits depends heavily on precise impedance control.

Figure A 7 - dsadsadsa

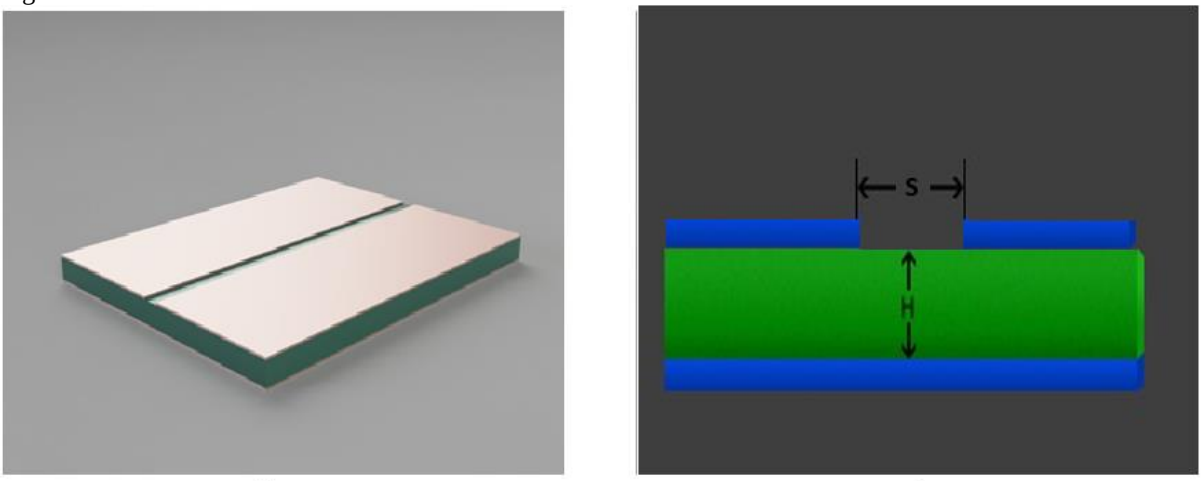

a b

For slot line transmission lines, the effective relative permittivity and characteristic impedance can be calculated using the expression derived by Garg and Gupta in their study on slot line wavelength and impedance. These calculations are fundamental for optimizing slot line designs and achieving the desired performance in microwave applications[124].

$$\epsilon_{r,eff}(\mathrm{f},\mathrm{t}) = \epsilon_{r,eff}(\mathrm{f},\mathrm{t}=0) - \left(\frac{\epsilon_{\mathrm{r}}-1}{4.6}\frac{\frac{\mathrm{t}}{\mathrm{h}}}{\sqrt{\frac{\mathrm{W}}{\mathrm{h}}}}\right) \quad \text{A. 43}$$

$$\epsilon_{r,eff}(\mathrm{f},\mathrm{t}=0) = \left(\frac{\lambda_0}{\lambda_{\mathrm{g}}}\right)^2 \quad \text{A. 44}$$

$$\lambda_{\mathrm{g}} = \lambda_0(A_1 + B_1 * g_1 + C_2 * g_1 + D_2 * g_3 + E_2 + F_2 + G_1) \quad \text{A. 45}$$

$$Z_0 = A_2 + B_2 * g_1 + C_2 * g_1 + D_2 * g_3 + E_2 + F_2 \quad \text{A. 46}$$

From Appendix–A. [18]

For $\left(0.0015 \le \frac{w}{\lambda_0} \le 00.075\right)$

$$f_1 = ln\,\epsilon_r,\ f_2 = \frac{w}{h},\quad f_3 = ln\left(\frac{h}{\lambda_0}\right),\ A_1 = 1.045,\ B_1 = -0.365 \quad \text{A. 47}$$

$$C_1 = \left[\frac{6.3\epsilon_r^{0.945}}{238.64+\frac{100w}{h}}\right] \quad \text{A. 48}$$

$$D_1 = \left[0.0599 - \frac{8.3695}{100\epsilon_{\mathrm{r}}}\right] \quad \text{A. 49}$$

$$E_1 = 0 \quad \text{A. 50}$$

$$F_1 = 0 \quad \text{A. 51}$$

$$G_1 = 0 \quad \text{A. 52}$$

For multilayers: $(\epsilon_r - 1)$turns into $(\epsilon_{r1} - \epsilon_{r2})$ from equation 0.43. Again, by substituting the equations recursively, the final value of the permittivity is obtained:

$$\epsilon_{r,eff}(\mathrm{f},\mathrm{t}) = \left(\frac{\lambda_0}{\lambda_0(A_1+B_1*g_1+C_2*g_1+D_2*g_3+E_2+F_2+G_1)}\right)^2 - \left(\frac{\epsilon_{\mathrm{r}}-1}{4.6}\frac{\frac{\mathrm{t}}{\mathrm{h}}}{\sqrt{\frac{\mathrm{W}}{\mathrm{h}}}}\right) \quad \text{A. 53}$$

Where 1, will be replaced by ϵ_{r2} from equation [0.53]. The first part of the equation does not depend on the radius, then, the derivative concerns only the second part,

$$\left|\frac{\partial}{\partial v}(\epsilon_{r,eff})\right| = -\frac{\frac{\mathrm{t}}{\mathrm{h}}}{4.6\sqrt{\frac{\mathrm{W}}{\mathrm{h}}}}\left(\frac{4\pi r^2}{\gamma\epsilon_{\mathrm{r1}}^{\gamma-1}v_t}(\epsilon_{\mathrm{p}}^{\gamma} - \epsilon_{\mathrm{w}}^{\gamma})dr\right) \quad \text{A. 54}$$

Figure A 8 - (a) illustrates the effective permittivity as a function of frequency, showing that it remains constant. Figure (b) depicts the relationship between the derivative of the effective permittivity and the radius of the plastic sphere.

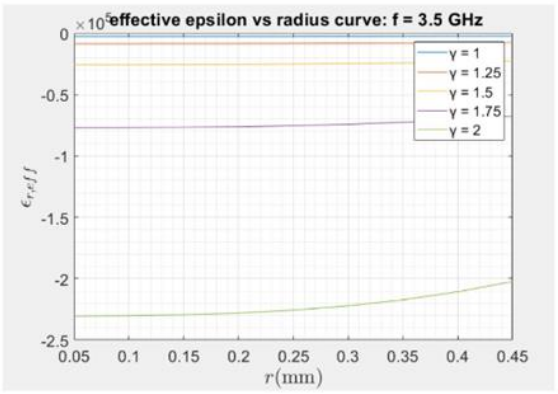

a

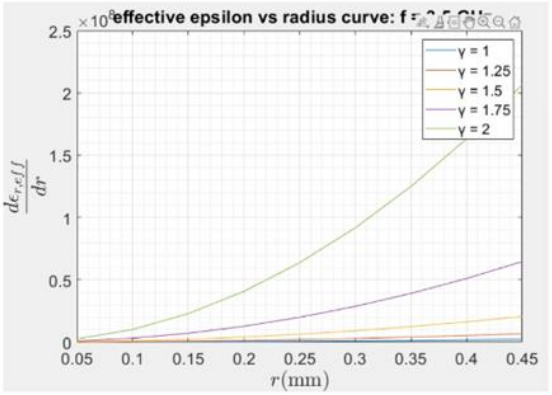

b

In conclusion, after thorough analysis and comparison of different transmission line technologies for material characterization with respect to pollutant detection, the microstrip technology stood out as the most suitable choice. The graphs clearly demonstrated that the microstrip configuration exhibited a steeper curve in absolute value concerning the permittivity derivative, showcasing its heightened sensitivity to changes in pollutant concentration or volume. Additionally, all the technologies, including microstrip, showed optimal performance at a propagation factor of 2. This observation indicates the optimal conditions for accurate material characterization and highlights the importance of selecting the appropriate propagation factor for reliable measurements.